NON-COVALENT INTERACTIONS AND THEIR

EFFECTS ON CHEMICAL REACTIVITY

by

Muhammad Kazim

A dissertation submitted to Johns Hopkins University in conformity with the requirements for
the degree of Doctor of Philosophy

Baltimore, Maryland

April 2022

Abstract

Non-covalent interactions play significant role across a variety of scientific fields including molecular self-assembly and supramolecular chemistry. Over the past few decades, different types of non-covalent interactions have been investigated through experimental and computational means. Yet, many aspects of these interactions are still rather unexplored. Additionally, studies involving application of close spatial interactions to influence chemical reactivity are rare. This research not only explores certain physical aspects of non-covalent interactions but also investigates their effects on chemical reactivity of some important organic functional groups. For instance, we expand the current understandings of conventional (amide NH···F) and non-conventional OH···π hydrogen bonding interactions. An inverse correlation was observed between the strength of amide NH···F hydrogen bond and electronic density of aromatic rings in 1,8-disubstituted naphthalenes, wherein the ^{1}H–^{19}F coupling constants are among the largest observed so far. Crystallographic analysis of a few substituted analogues based on fused 9,10-dihydroanthracene-bicycloheptane scaffold revealed a stepwise switch of a HO···π interaction to a strong non-conventional OH···π hydrogen bond by increasing the electronic density on the aromatic ring. Additionally, we were able to isolate and crystallize an indefinitely stable ring unsubstituted aliphatic para quinone methide (*p*-QM) which portrayed chemical transformations contrary to the traditional QM chemistry. For example, it resisted all attempts at aromatization by reduction (both catalytic and hydride based) whereas nucleophilic addition resulted in an unanticipated rearrangement of the molecular framework to yield an overall hydrogenation reaction placing each hydrogen *nine* heavy atoms apart. Protonation with a strong acid resulted in a crystallizable cation stabilized by a combination of partial aromatization of the QM moiety and cation–π interactions. Most importantly, the *p*-QM fragment facilitated an unprecedented photochemical oxygen insertion with the earth abundant dioxygen gas into the proximate aromatic ring while remaining intact itself. Mechanistic investigation, both experimental and computational, points to the criticality of the QM fragment to this important, yet unexplored metal free oxygen insertion into a pure organic scaffold. Finally, we present the first ever X-ray crystal structure of a symmetrical organic fluoronium cation, thereby providing an ultimate existential proof of the last missing piece of the halonium ion family.

Advisor: Professor Thomas Lectka

Reader: Professor Rebekka S. Klausen

Reader: Professor John P. Toscano

Dedicated to my family and friends,

especially to my loving parents – Jamila and Sajjad

Acknowledgments

Till the end of 10th grade, I hated chemistry with everything in me. Every time I opened my chemistry textbook, I could feel my blood pressure elevate. At the time, I had no choice but to deal with it since it was a part of our national curriculum. However, my perception changed after taking chemistry classes with Prof. Niaz Hussain in Quetta during 2011-12. His teaching style and dedication made me fall in love with the subject, especially organic chemistry. Sadly, he passed away a few days after completing our chemistry course. If it were not for my interactions with him, I would have never thought of studying chemistry, let alone doing a PhD in it. Therefore, I would like to start by expressing my eternal gratitude to him. May his soul rest in eternal peace and may Allah grant him highest ranks in Jannah.

When I first came to the United States, I was an ambitious yet inexperienced chemist looking forward to facing any challenge graduate school had to offer. Upon reflection, I have come to realize that the last 5 years have been a period of tremendous personal and scientific growth. At the heart of it is the role played by my advisor Prof. Thomas Lectka. Tom gave me the intellectual freedom in research, constantly pushed me to go beyond my comfort zone, and always inspired me to be better. I am grateful to him for creating a wonderful, collaborative group environment where everyone feels comfortable expressing themselves intellectually and personally. Tom was an amazing advisor, mentor, and ultimately an even better friend.

Beyond my advisor, I would like to thank Prof. John P. Toscano and Prof. Rebekka S. Klausen for serving on my thesis committee. They have both been wonderful mentors and provided me with helpful and valuable career advice. A big part of my graduate research involved computational chemistry which would not have been possible without the help and support from Prof. Lan Cheng. I would also like to thank Prof. Travis Dudding of Brock University, Canada who helped us with computational analysis on multiple projects. His helpful discussions and calculations made several projects come to fruition. We also collaborated with extremely talented chemists in Prof. Sebastian Riedel's group in Germany. I had the opportunity to meet with Prof. Riedel in Florida during the 25th Winter Fluorine Conference and have valuable discussions with

him. I am very thankful to him for all his help and guidance. I would also like to thank Prof. Ernesto Freire and Prof. Anthony Shoji Hall for serving on my GBO committee.

Next, I would like the extend my gratitude to all my Lectka group colleagues with whom I have worked and spent most of my time in graduate school. When I joined the group, all senior members Maxwell Holl, Liangyu Guan, Cody Pitts, and Desta Bume helped me significantly. Though I did not overlap with Cody for long, we stayed in touch after his graduation and collaborated on a few projects. Desta is one of the most honest, talented, and hardworking chemists I have encountered. His work ethic always inspires me to be a better chemist. Max and Liangyu were working on the *physical organic* side of the lab when I joined the group and thus became my mentors. Max helped me establish a good mindset and proper lab techniques while Liangyu helped me develop computational skills that helped me through the remainder of my PhD. After they left the Lectka laboratory in 2018, I became the only member of the group working in the physical organic side of the lab. Working alone for the first time, I had to figure out many things the hard way. However, I was lucky to have colleagues and friends like Stefan Harry, Fereshte Ghorabni, Joseph Capilato and Gabriel York to help and support me throughout the process. They were all extremely helpful, always available for discussions, and the most talented chemists I have worked and *"worked out"* with. I also had the opportunity to establish some exciting chemistry with Stefan over the last year and we hope to publish those results soon. Recently, Eric Holt, Muyuan Wang and Nathaniel Garrison have joined the group. Although I have spent much less time with them, I am very optimistic about their creativity, hard work and determination. I am confident that the Lectka laboratory has very talented chemists to continue doing very exciting research.

Additionally, I was tasked to train several undergraduates throughout my PhD. I would like to thank Juan Sanfiel, my first student, for being patient with me training him when I was in training myself. In many ways, he helped me learn how to be a better teacher in the lab. Thereafter, I had the pleasure of working with Anant Chopra, a very talented individual, who remained my student throughout his undergraduate degree. I will always be thankful to him for he made sure I always have clean NMR tubes, besides helping me out with my projects. Additionally, I have had the chance to train Phuong Nguyen, another very talented

Table of Contents

List of Tables

List of Figures

List of Schemes

Chapter 1. Introduction

1.1 Non-covalent interactions in organic chemistry

Before the 20th century, the description of chemical bonds was mainly based on intuition and empirical studies and the attractive interactions between atoms, ions, or molecules were generally called chemical bonds. With the advent of quantum mechanical theory, along with the development of valence bond and molecular orbital theories, questions on the physical characteristics of chemical bonds were raised. Based on different behaviors of valence electrons, these interactions were classified mainly into covalent and non-covalent interactions among others. In a covalent bond, electron pairs are shared between the interacting atoms, wherein the electrons may come from either both atoms or only one of them. Non-covalent interactions, on the other hand, involve electrostatic interactions arising from either permanent or induced dipoles. Covalent bonds have been studied in-depth over the past few decades, whereas non-covalent interactions did not receive much attention until the 1980's when the Nobel Prize in Chemistry was awarded to Donald J. Cram, Jean-Marie Lehn, and Charles J. Pedersen in recognition of their works in supramolecular chemistry. Thereafter, non-covalent interactions were studied in more detail and their criticality in supramolecular chemistry, biochemistry, materials chemistry, medicinal chemistry, nanotechnology, and even organic synthesis were gradually recognized. These interactions were classified into different categories including Van Der Waals forces, London Dispersion forces, hydrogen bonding, π–π interactions, cation–π interactions, etc. to name a few.

Chemical reactivity involves bond breaking and formation, thus changing the electronic state of atoms, ions, or molecules involved in the reaction. Outcomes of chemical reactions depend on the factors determining the environment in which they occur, e.g., temperature, pressure, solvent, concentration, etc. In addition to these *"controllable"* variables, nature often takes advantage of non-covalent interactions to affect chemical transformations by placing atoms or functional groups in close spatial proximity to the reactive sites. This is how enzymes catalyze very specific and selective transformations without blasting at

substrates with raw power like human-designed reagents tend to. For example, two amino acid residues [174]Lys and [89]Glu synergistically engage in hydrogen bonding interactions in the enzymatic pocket of dimethylallyl tryptophan synthase (DMTS) to direct prenylation of an indole ring at the C-4 position in the presence of a more reactive C-7 position. In the laboratory, chemists have a good hold over the "*controllable*" variables in dictating chemical reactivity. However, non-covalent interactions as reaction variables have not yet gained generality status in the laboratory setting. Since most of the non-covalent interactions are weak, they are hard to observe, control, or manipulate. Computational chemistry provides a powerful tool to study these non-covalent interactions as it is easy to manipulate their strengths by modifying the distances and adjacent substituents on the interacting molecules/groups. However, synthetically changing these variables is a challenging task. We have employed caged molecular motifs to lock select heteroatoms in close spatial proximity to a variety of organic functional groups to study the effects of their non-covalent interactions in a more specific and controllable way. The effects were dramatic. Most notably, we successfully observed, isolated, and characterized the first-ever symmetric organic fluoronium cation both in solution and in the solid state. We hope that the results presented in this dissertation will shed light on the research of non-covalent interactions as well as provide new strategies in synthetic organic chemistry.

1.2 Brief Overview

In this work, each chapter represents a body of previously published work with only minor changes made to fit the format of the dissertation. In chapters 2-5, we present the synthesis, characterization, and the unusual chemical reactivity of a ring-unsubstituted aliphatic para quinone methide (*p*-QM). This p-QM resists all attempts at reductive aromatization, rearranges upon treatment with soft nucleophiles, protonates with strong acids to form a crystallizable cation and undergoes unprecedented metal free photochemical oxygen insertion with QM fragment playing critical role in this transformation. In chapter 6, we study the correlation between aromatic substitution and the strength of amide NH---F hydrogen bonding interaction in 1,8-disubstituted naphthalene derivatives. In chapter 7, we present detailed spectroscopic and crystallographic analysis of the effects of aromatic substitution on the orientation of OH

proton in 9,10-dihydroanthracene-bicycloheptane scaffolds. In systems with electron rich aromatic rings, the alcoholic proton locks in the "*in*" orientation to engage in strong *non-conventional* hydrogen bonding interaction with the adjacent aromatic ring whereas it switches to the *"out"* form when the aromatic rings are electron deficient. Chapter 8 presents the first ever X-ray crystallographic analysis of a symmetrical organic fluoronium ion, thereby providing an ultimate proof for the existence of often considered impossible species. Besides its crystallographic evidence, we investigated various vibrational modes in this cation through IR spectroscopic analysis. All the experimental data are combined in chapter 9 with sub-sections for each chapter.

Chapter 2. A Case of Serendipity: Synthesis, Characterization, and Unique Chemistry of a Stable, Ring Unsubstituted Aliphatic p-Quinone Methide

2.1 Introduction

p-Quinone methides (p-QMs) are remarkable chemical species most often encountered in the biochemical realm. They and their derivatives play an important role in DNA alkylation and crosslinking,[1] in addition to serving as intermediates in organic synthesis.[2-4] Due to their importance in both biological as well as chemical processes, p-QMs have been subjected to intensive study, although they are usually unstable and exist mainly as reactive intermediates.[5] Simple aliphatic p-QMs prove to be especially unstable,[6] which means that they react quickly with just about anything in the reaction medium. Imagine instead a stable, isolable aliphatic p-QM in hand – the chemist could thus investigate interesting chemical reactivity on his own terms, and his reactions of choice.

Previous attempts at the synthesis and isolation of simple p-QMs suggest that certain substitutions at the 2, 6 and 7 positions on the quinone ring are important for enhancement of stability (the simplest p-QM is naturally highly unstable) (Scheme **2.1**). A few very select substituted forms have been synthesized and studied for their physical and chemical properties. For example, Chitwood et al. have synthesized the highly resonance stabilized 7,7-diphenyl p-QM.[7] Hyatt synthesized and studied the chemistry of the likewise stable 7,7-dicyano p-QM.[8] Four different versions of 7-cyano-7-carboxy ester p-QMs have successfully been made and studied as stable molecules.[9] In contrast, Murray et al. observed that 7,7-bis(trifluoromethyl) p-QM is stable only below -196°C and quickly polymerizes upon warming to room temperature.[10] This particular p-QM motif can only be stabilized by replacing hydrogens at the 2 and 6 positions with alkyl groups.[11] Generally speaking, p-QMs containing alkyl groups at the 7-position are very reactive and dimerize upon attempted isolation unless the 2 and 6 positions have bulky substituents, as observed by Cook and Norcross.[12] Additionally, stabilization of unsubstituted p-QMs using transition metals was first reported by Vigalok et al.;[13] this strategy was followed up by several other groups.[14] In general, p-QMs are most often observed as reactive intermediates unless otherwise stabilized by resonance (for example as

part of a polycyclic structure[15] or through attachment of electron-delocalizing functional groups) or transition metals. In fact, the actual "quinone methide" form may be only one of a large family of other competing resonance structures,[16] and it stands to reason that simple unsubstituted aliphatic p-QMs are generally very unstable in solution. To our knowledge, there has been no evidence of a stable aliphatic p-QM unsubstituted at the 2 and 6 positions.

2.2 Synthesis

The story began with the attempted synthesis of the corresponding tertiary chloride from alcohol **3**, which was in turn formed through a Grignard reaction on the known ketone **2**.[17, 18] To our surprise, treatment of alcohol **3** with SOCl$_2$ and catalytic Et$_3$N resulted instead in demethanolation to form the quinone methide **1** (Scheme **2.1**) as a lemon yellow solid after purification (56% yield). The downfield shift of the bridge protons near the -OH from 2.96 ppm in alcohol **3** to 3.37 ppm in the product suggested a change in hybridization of the tetrasubstituted carbon from sp^3 to sp^2. Moreover, the disappearance of methyl protons (3.74 ppm) and the hydroxyl proton (0.47 ppm) in ^{1}H NMR as well as the appearance of a peak around 186.1 ppm in the ^{13}C NMR of the product indicated the formation of the p-QM **1**. The UV-vis spectrum of the product showed two absorbances at 281 nm and 340 nm corresponding to orbital transitions on the aromatic rings and the p-QM fragment, respectively.
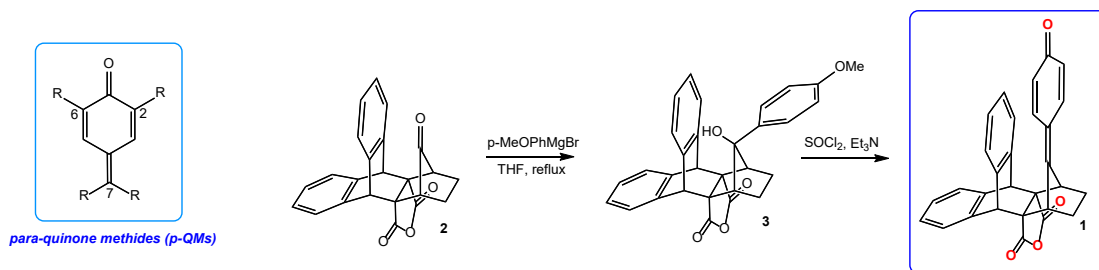
Scheme 2.1. *Generic p-QM motif and synthesis of the aliphatic para-quinone methide (p-QM)* **1**.

This demethanolation to form **1** makes sense in retrospect - the sterically hindered carbocation generated by the departure of the -OH leaving group can (for both steric and electronic reasons) only trap chloride from the backside "out" position. This process forces the aromatic rings to clash, thus adding steric strain to the system. Therefore, it is energetically favorable for the molecule to undergo the unexpected

demethanolation instead to form p-QM **1**. Any process that involves the retention of aromaticity is liable to be disfavored, affording the p-QM structure stability.

2.3 X-ray Crystal Structure

Accordingly, p-QM **1** turned out to be exceptionally kinetically stable and remained intact when dissolved in various solvents such as acetonitrile and THF. Its high stability allowed us to crystallize it from CH_2Cl_2 for an X-ray structure determination (Figure **2.1**). A side view of the structure shows that, unlike graphene sheets in graphite,[19, 20] the QM fragment and neighboring aromatic ring are not perfectly stacked, but bent slightly away from each other. For example, whereas carbon 7 is roughly 2.8 Å from the plane of the neighboring aromatic ring, carbon 4 is about 3.1 Å away. Furthermore, the bond angle between the bridge carbons near the QM moiety and carbon 7 has been reduced to 98.18^0 in **1** which is lower than the same bond angle observed for the p-QM (114.37^0) reported by Taljaard and co-workers.[21] In contrast, the bond angle between bridge carbon, carbon 7 and carbon 4 on the QM moiety is 130^0, which is larger than the same bond angle in Taljaard's p-QM (122^0).[21] These strained bond angles, induced by the Baeyer strain of the norbornyl cage of **1**, might explain some of the unique chemical reactivity associated with the p-QM **1** detailed below. The molecule co-crystallizes with CH_2Cl_2, whose presence is notable by a close approach of Cl to the said aromatic ring (3.62 Å).
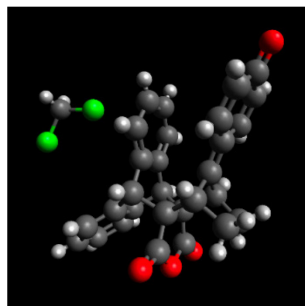
*Figure 2.1. X-ray crystal structure of p-QM **1** (including a molecule of solvent DCM)*

2.4 Reactions

We turned next to detailing **1**'s reaction chemistry through three archetypical chemical transformations: hydrogenation, hydride reduction, and nucleophilic addition. It did not take long to discover that **1** behaves

in ways that contrast with conventional quinone methide chemistry. Typically, stable p-QMs hydrogenate through 1,6-addition in order to facilitate the formation of an aromatic ring. For example, the catalytic hydrogenation of 7,7-dicyano p-QM yields (p-hydroxyphenyl)malononitrile as a result of 1,6-addition.[8] When **1** was subjected to standard catalytic reduction (H$_2$, Pd/C) the major product revealed regioselective hydrogenation of the two endocyclic double bonds. The reaction, which was done on mg scales, afforded 77% crude NMR yield; 49% isolated and analytically pure product (Scheme **2.2**). Isolated yields for the reactions in general are low due to the difficulty we encountered in working on very small scales.
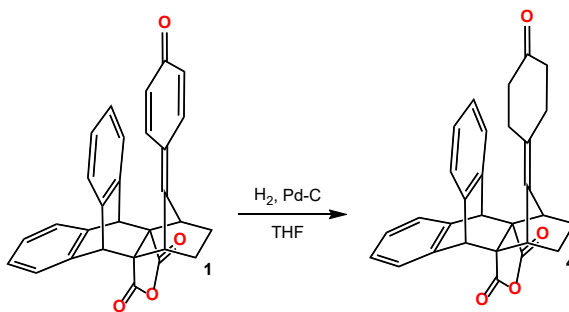
Scheme 2.2. Catalytic hydrogenation of p-QM 1.

p-QM **1**'s resistance to aromatization by *catalytic* reduction led us to investigate its behavior with a strong carbonyl reducing agent. Precedent also reveals that more stabilized p-QMs generally aromatize upon LiAlH$_4$ reduction; for example, treatment of the p-QM 2,6-di-t-Bu-7,7-dimethyl p-QM yields 2,6-di-*t*-butyl-4-isopropenylphenol as a result of 1,6-addition.[12] Interestingly, we found that the resistance to aromatization can be overcome in this particular case. Treatment of **1** with LiAlH$_4$ resulted in rearranged alcohol **5** as the major product (70% by crude NMR, 34% isolated yield, Scheme **2.3**) which presumably arises in the workup step, wherein water can affect rearrangement, aromatization, and trapping.

The appearance of aromatic protons in the range 6.85 – 7.00 ppm and a singlet peak for the OH proton at 0.67 ppm in the ^{1}H NMR of the product indicated that the aromatic ring is pointing inward (previous works from our group have shown that the proton peak for the OH group appears *downfield* in the negative region of the ^{1}H NMR if the OH group is pointing in).[17] The structure of **5** was also confirmed by X-ray crystallography, most notably confirming the two "pancaked" aromatic rings. In the crystal structure, **5** has

lost its plane of symmetry, which is not apparent on the NMR time scale. DFT calculations (ωB97XD/6-311+G**) suggest the in-OH diastereomer to be 5.75 kcal/mol more stable than the observed out-OH (Figure **2.2**). However, the nucleophilic attack of water on the putative cationic intermediate that forms the energetically more stable product is apparently blocked by the "stacked" aromatic ring. The closest approach of the two pancaked aromatic rings in **5** is 3.0 Å which is similar to the mean C-C distance in 2,2-cyclophanes but less than its higher homologs; for example, the distance between the neighboring aromatic rings is almost 4.0 Å for 4,4-cyclophanes.[22] Once again, the crystal incorporates a CH_2Cl_2 molecule in the unit cell; in contrast to **1**, a hydrogen atom instead makes a close approach to plane of the 'bottom" aromatic ring (ca. 2.9 Å).
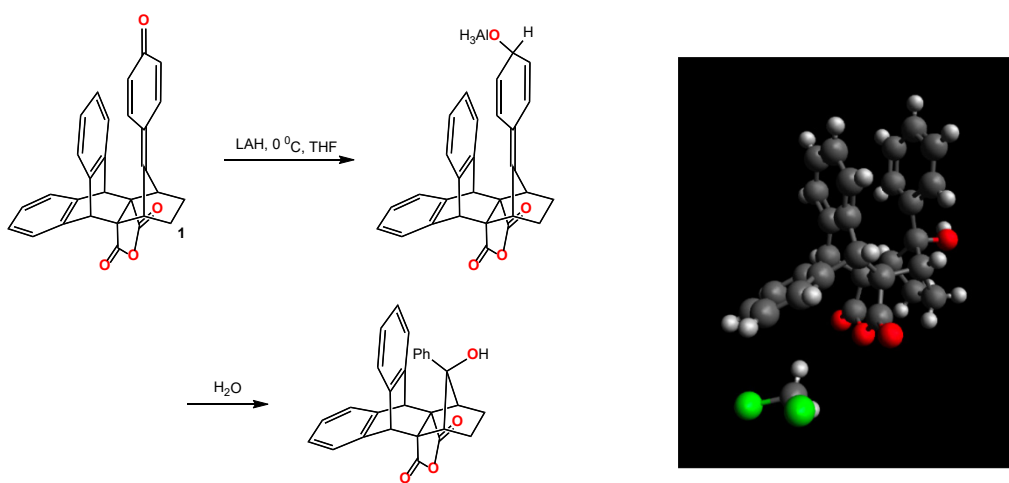
Scheme 2.3. *LiAlH$_4$ reduction of p-QM **1** to afford **5**. X-ray crystal structure of **5** (including a molecule of DCM solvent).*
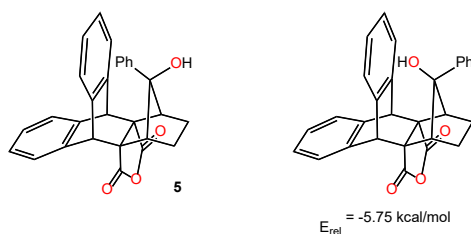
Figure 2.2. *Relative energy of **5** and its diastereomer at ωB97XD/6-311+G**.*

α,β-Unsaturated carbonyl compounds are well known for undergoing conjugate addition reactions of all kinds;[23, 24] thiols are particularly promiscuous nucleophiles for this purpose. A few p-QMs are known to

react with nucleophiles through 1,6-addition to yield an aromatic product.[25, 26] When **1** was treated with β-mercaptoethanol and triethylamine, it formed the aromatic ring that is expected to result from a 1,6-addition. However, rather than trapping the thiol in what would be a strain inducing process, a skeletal rearrangement results instead (90% yield by crude NMR, 30% isolated). Presumably, protonation of the carbonyl group is followed by an attack on the adjacent aromatic ring. The resultant putative benzylic carbocation is reduced by a hydride source (either the amine or the thiol itself). The net reaction is addition of a hydrogen molecule to **1** with each H atom attaching to two spatially remote positions *nine* heavy atoms removed from each other (Scheme **2.4**). That the C_s symmetry of the molecule has been broken is evident in the more complex ^{1}H NMR (in CD_3CN) of the product. Additionally, the coupling constant (15 Hz) between the protons resonating at 2.2 ppm and 3.1 ppm indicates that they are benzylic and geminal to each other. The product was finally confirmed by its X-ray crystal structure, which clearly reveals the rearranged skeleton and the newly installed benzylic methylene.

  In conclusion, we have synthesized and characterized an indefinitely solution stable ring unsubstituted aliphatic p-quinone methide **1**. It exhibits counterintuitive reaction chemistry as it resists attempts at aromatization by catalytic reduction, but nevertheless aromatizes and rearranges with strong reducing agents in spite of substantial strain induction. Finally, it experiences a skeletal rearrangement upon nucleophilic addition. We hope that these findings provide some new insights into the physical and chemical properties of this important class of organic molecules.
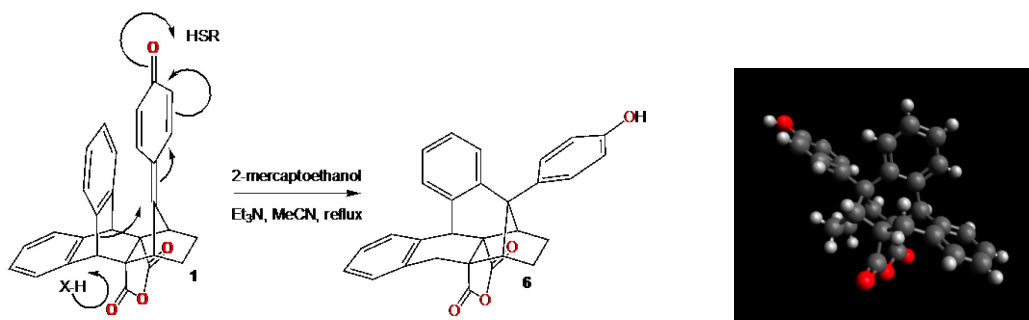
Scheme 2.4. *Thiol/amine reduction/rearrangement of p-QM **1** to form **6**; X-ray structure of **6**.*

2.5 REFERENCES

1. Wang, P.; Song, Y.; Zhang, L.; He, H.; Zhou, X. *Curr. Med. Chem.* **2005,** *12*, 2893-2913.

2. Poss, A. J.; Belter, R. K. *Tetrahedron Lett.* **1987,** *28*, 2555-2558.

3. Angle, S. R.; Turnbull, K. D. *J. Am. Chem. Soc.* **1989,** *111*, 1136-1138.

4. Kende, A. S.; Liebeskind, L. S.; Mills, J. E.; Rutledge, P. S.; Curran, D. P. *J. Am. Chem. Soc.* **1977,** *99*, 7082-7083.

5. Sugumaran, M. *Int. J. Mol. Sci.* **2016,** *17*, 1576-1598.

6. Cunane, L. M.; Chen, Z. W.; Shamala, N.; Mathews, F. S.; Cronin, C. N.; McIntire, W. S. *J. Mol. Biol.* **2000,** *295*, 357-74.

7. Martin, J. C.; Chitwood, J. L.; Gott, P. G.; Krutak, J. J. *J. Org. Chem.* **1971,** *36*, 2216-2222.

8. Hyatt, J. A. *J. Org. Chem.* **1983,** *48*, 129-131.

9. Iwatsuki, S.; Itoh, T.; Meng, X. *Macromolecules* **1993,** *26*, 1213-1220.

10. Murray, J. J. *J. Org. Chem.* **1968,** *33*, 3306-3308.

11. Sheppard, W. A. *J. Org. Chem.* **1968,** *33*, 3297-3306.

12. Cook, C. D.; Norcross, B. E. *J. Am. Chem. Soc.* **1956,** *78*, 3797-3799.

13. Vigalok, A.; Milstein, D. *J. Am. Chem. Soc.* **1997,** *119*, 7873-7874.

14. Poverenov, E.; Milstein, D. in *Quinone Methides*, Rokita, S. E., Ed. John Wiley & Sons, Inc.: USA, 2009; Vol. 1, pp 69-88.

15. Turner, A. B. *Q. Rev. Chem. Soc.* **1964**, 347-360.

16. Toteva, M. M.; Richard, J. P. *Adv. Phys. Org. Chem.* **2011,** *45*, 39-91.

17. Guan, L.; Holl, M. G.; Pitts, C. R.; Struble, M. D.; Siegler, M. A.; Lectka, T. *J. Am. Chem. Soc.* **2017,** *139*, 14913-14916.

18. Holl, M. G.; Struble, M. D.; Singal, P.; Siegler, M. A.; Lectka, T. *Angew. Chem.* **2016,** *128*, 8406-8409.

19. Bernal, J. D.; Bragg, W. L. *P. R. Soc. Lond. A-Conta.* **1924,** *106*, 749-773.

20. Haering, R. R. *Can. J. Phys.* **1958,** *36*, 352-362.

21. Taljaard, B.; Taljaard, J. H.; Imrie, C.; Caira, M. R. *Eur. J. Org. Chem.* **2005,** *2005*, 2607-2619.

22. Keehn, P. M. in *Cyclophanes*, Keehn, P. M.; Rosenfeld, S. M., Eds. Academic Press: 1983; Vol. 45, pp 69-238.

23. Kanai, M.; Shibasaki, M. In *Catalytic Asymmetric Synthesis*, 2nd ed.; Ojima, I., Ed. Wiley-VCH: New York, 2000; pp 569-592.

24. Perlmutter, P., *Conjugate Addition Reactions in Organic Synthesis*. Pergammon Press: 1992.

25. Nakagawa, Y.; Hiraga, K.; Suga, T. *Biochem. Pharmacol.* **1983,** *32*, 1417-1421.

26. Richard, J. P.; Toteva, M. M.; Crugeiras, J. *J. Am. Chem. Soc.* **2000,** *122*, 1664-1674.

Chapter 3: A Protonated Quinone Methide Stabilized by a Combination of Partial Aromatization and π-Interaction: Spectroscopic and Crystallographic Analysis

3.1 Introduction

Noncovalent cation-π interactions are of prime importance in various areas of study such as chemistry, materials science and biology.[1-6] Among the first recognized examples was reported in 1981 when Kebarle et al. showed that a naked K^+ ion in the gas phase binds preferentially to benzene over water.[7] The nascent field soon ramified greatly to include interactions of π-systems with other metal cations,[8] ammonium salts,[9, 10] and sulfonium ions,[11] to name but a few examples. One region of the wide spectrum of potential interactions remains both relatively unexplored and interesting to us – namely the interaction of *carbocationic* centers with the π-faces of aromatic rings in proximity. From a biochemical perspective, a few intriguing X-ray structural studies of enzymatic systems suggest that key aromatic amino acid residues play a role in stabilizing carbocation intermediates.[4, 12-15] Being coordinatively unsaturated, carbo-cations are expected to interact somewhat differently with π - systems than ammonium cations, for example.[16,17-19] On the other hand, experimental examples of chemical systems that explore the nature of carbocation-π interactions in aromatic systems are fairly rare.[20]
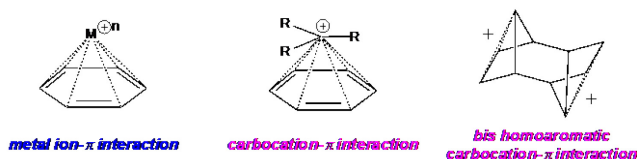
Figure 3.1. *Generalized aryl cation-π interactions and an example of carbocation-π interacting system.*

In this chapter, we present an unusual carbocation resulting from protonation at the carbonyl oxygen of a recently reported para-quinone methide (p-QM **1**, Figure **3.2**).[21] NMR, UV-Vis, and crystallographic analyses show that the protonated form is stabilized not only by the expected partial aromatization of the

p-QM moiety, but also by a mild through-space, π-cation interaction with the proximate aromatic ring. Single crystal X-ray analysis revealed an interesting structure consisting of a hydrogen-bound complex involving two molecules of the precursor and one shared proton.

3.2 Results and Discussion

Previous studies reveal that under acidic conditions, relatively stable p-QM's undergo solvolysis through 1,6-addition. For example, 2,6,7,7-tetralkyl-substituted p-QM's undergo spontaneous alcoholysis when treated with acids in MeOH.[22] The high stability of p-QM **1** suggested to us that it instead would prove refractory to discrete methanolysis under similar conditions. Although true enough, it provided the first experimental hint of the facile protonation of **1**. A lemon-yellow solution of p-QM **1** in methanol instantly turned dark amber upon the addition of a drop of concentrated sulfuric acid, indicative of possible carbocation formation; even when stirred at room temperature for 24 h, **1** was recovered quantitatively after work-up. We hypothesized that the colour change corresponded to the protonation of the QM-carbonyl oxygen rather than protonation of an anhydride oxygen. Our hypothesis was backed by DFT calculations at ωB97XD/6-311+G** that predicts the carbonyl oxygen to be the most basic site in **1** by a large measure (Figure **3.2**).
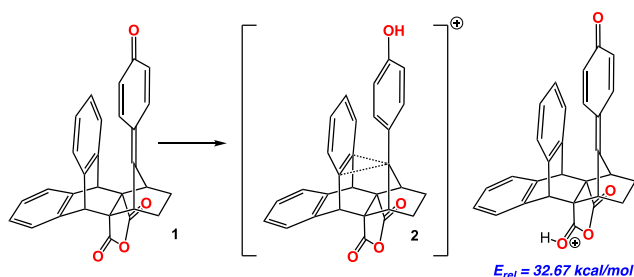
*Figure 3.2. Protonation of 1, and the relative stability of the anhydrido-protonated form at ωB97XD/6-311+G**.*

The resultant cation **2** is also calculated to be some 35.8 kcal/mol and 16.4 kcal/mol more stable than the reactants for protonated acetone and benzophenone. More importantly, calculations predict a direct correlation between the electronic nature of the neighboring aromatic ring and the basicity of the QM

moiety, i.e., the more electron rich the aromatic ring, the more basic the QM carbonyl group, suggesting the possibility for a fruitful carbocation-π interaction. The isodesmic relation[23] (Equation **3.1**) was calculated to be *exothermic* by 3.4 kcal/mol when the neighboring aromatic ring contains an amino group in the top position (X = NH_2) and *endothermic* by 2.3 kcal/mol when it possesses a nitro group at the same position (X = NO_2). Thus, a combination of partial aromatization and delocalization of positive charge onto the proximate aromatic ring seems to account for the predicted basicity of **1**. Interestingly, DFT calculations (ωB97XD/6-311+G**) also predict the carbonyl oxygen to be more basic than the aniline nitrogen of the top-amine version of p-QM **1** by 8.4 kcal/mol in vacuum and by 2.5 kcal/mol in acetonitrile (IEFPCM solvent model) (Figure **3.3**).

$\Delta E = 3.4$ kcal/mol (X = NH_2)
$\Delta E = -2.3$ kcal/mol (X = NO_2)
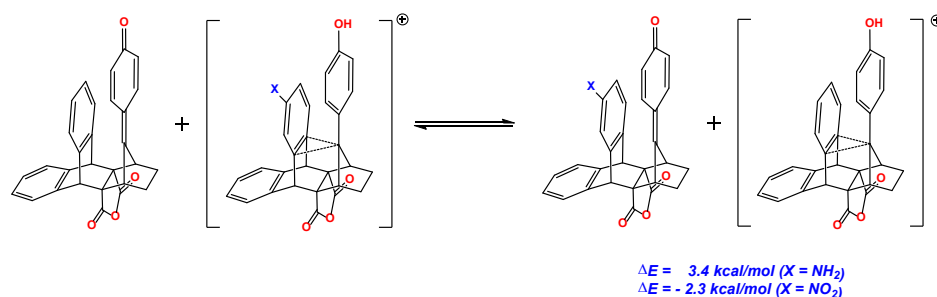
*Equation 3.1. Isodesmic relation comparing p-QM **1** with substituted forms.*

$E_{rel} = 8.4$ kcal/mol (in vacuum)
$E_{rel} = 2.5$ kcal/mol (in aceonitrile)
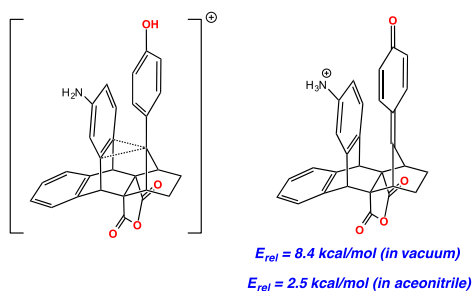
Figure 3.3. Protonation of the carbonyl oxygen vs aniline nitrogen.

Experimentally, a variety of protic acids and solvents were sampled in order to ascertain an optimal system for spectroscopic characterization. Initial trial experiments revealed acetonitrile to be the most flexible solvent for this purpose. Thereupon, we screened acetic acid, trifluoroacetic acid and triflic acid for their protonating ability. ^{1}H NMR analysis of p-QM **1** treated with all three protic acids suggests a fast exchange process in MeCN at the carbonyl oxygen of **1** at room temperature. The changes in the proton chemical

shifts of the QM moiety of **1** are moderate in CH$_3$COOH, intermediate in CF$_3$COOH, whereas limiting values are reached in TfOH (Figure **3.4**).

When treated with only 2 equiv. of triflic acid in CD$_3$CN at room temperature, the corresponding carbocation **2** forms cleanly (Scheme **3.1**). The ^{1}H NMR (in CD$_3$CN) clearly demonstrates the protonation of **1** at the carbonyl oxygen. The protons on the QM moiety are perturbed to a greater extent (6.07 ppm to 7.14 ppm and 7.01 ppm to 7.83 ppm) than the aromatic protons (6.79 ppm to 6.86 ppm, 7.25 ppm to 7.32 ppm, 7.35 ppm to 7.38 ppm and 7.37 ppm to 7.44 ppm) (Figure **3.4**). Similar trends are observed for both benzylic and aliphatic bridge protons (4.84 ppm to 5.0 ppm and 3.59 ppm to 4.01 ppm respectively), the latter being affected to a greater extent indicating their proximity to the cationic site in the molecule (Figure **3.5**).
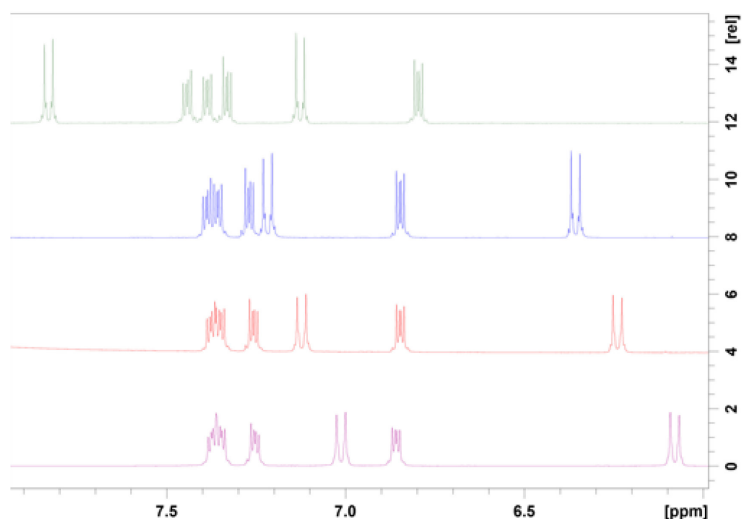
Figure 3.4. *Behavior of aromatic and QM protons when p-QM 1 is treated with different acids in CD$_3$CN. Doublets indicate protons on the QM fragment and multiplets represent protons on the aromatic rings. Bottom to top: (p-QM 1, p-QM 1 with acetic acid, p-QM 1 with trifluoroacetic acid, p-QM 1 with triflic acid).*

14
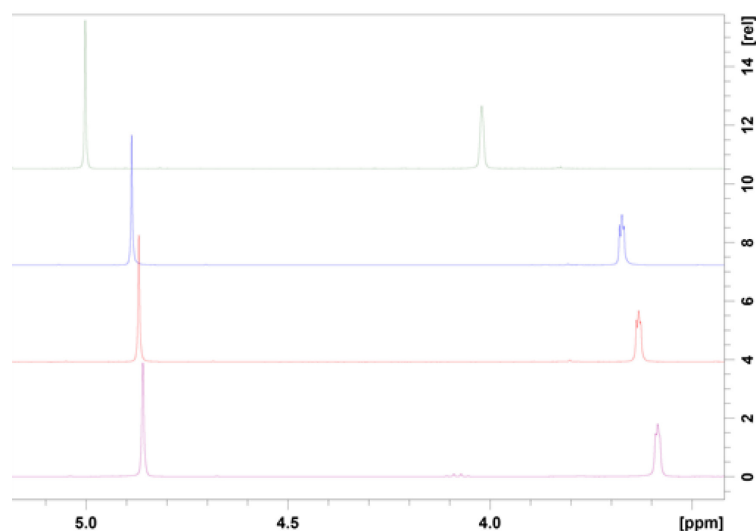
Figure 3.5. *Behavior of the bridge protons when p-QM 1 is treated with different acids in CD₃CN. Protons in the region*

3.5 – 4 ppm represent the bridge protons near the QM fragment while those in the region 4.8 – 5.1 ppm represent the

benzylic bridge protons. Bottom to top (p-QM 1, p-QM 1 with acetic acid, p-QM 1 with trifluoroacetic acid, p-QM 1

with triflic acid).

Nevertheless, this apparent fast exchange in the ^{1}H NMR spectrum suggested that ^{13}C NMR would be more illustrative, as chemical shifts could be more accurately calculated for comparison. The ^{13}C NMR resonance of the QM carbonyl group shifts upfield to 149.4 ppm, which is in agreement with the calculated ^{13}C NMR value for this carbon (calc. 149 ppm at B3LYP/6-311++G**). Conversely, the trisubstituted alkenyl, now a trisubstituted alkyl, carbon moves strongly downfield (204 ppm), consistent with the calculated ^{13}C NMR resonance value for this carbon (calc. 202 ppm at B3LYP/6-311++G**). The ^{13}C chemical shifts of the nearby aromatic ring are affected as well, albeit to a lesser extent. ^{13}C NMR spectra of **1** in the presence of HOAc and TFA are slightly changed, but only in the presence of TfOH are substantial, limiting shifts comparable to calculation noted. Taken together, the chemical shift data point to protonation by TfOH to form **2**, wherein partial aromatization of the QM moiety, and modest delocalization of charge on the proximate aromatic ring through a π-interaction focused at carbon 7 occur.
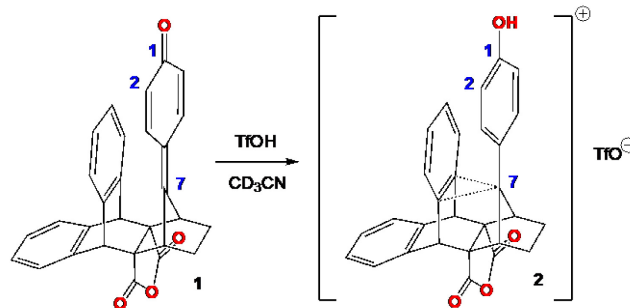
Scheme 3.1. *Protonation of p-QM* **1**.

p-QM **1** exhibits two absorption maxima at 281 nm and 337 nm in the UV-Vis spectrum (MeCN); in contrast, cation **2** shows three absorption peaks at 283 nm, 339 nm and 417 nm (Figure **3.6**). The new absorption in the visible region can be accounted for by preferential lowering of the primarily QM-centered LUMO upon protonation at the QM carbonyl group.
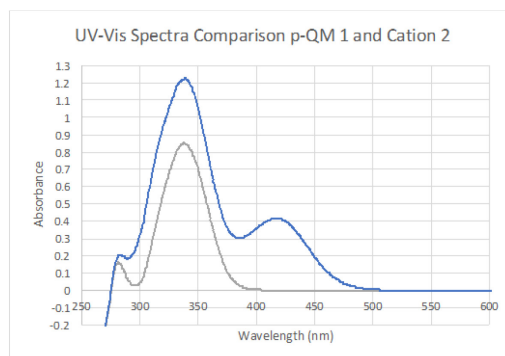
Figure 3.6. *UV-Vis spectra of p-QM* **1** *(gray) and cation* **2** *(blue) in MeCN.*

Another illuminating piece of data was provided by X-ray crystallographic analysis. Interestingly, the unit cell contains cation **2** stabilized by hydrogen bonding to other QM carbonyl oxygen atoms (Scheme **3.1** and Figure **3.9**). Changes in bond lengths (e.g. the C_1-C_2 bond attached to the p-QM carbonyl shrinks from 1.457 Å in the p-QM **1** to 1.431 Å and 1.433 Å in the QM molecules sharing the proton and 1.431 Å in the independent half protonated QM upon protonation) and interatomic distances are also consistent with partial aromatization of the QM moiety and some through-space delocalization of charge (approach of C_7 to the adjacent aromatic ring carbons changes from 2.894, 2.939 Å in the parent p-QM **1** to 2.842, 2.860 Å

and 2.866, 2.860 Å in the QMs sharing the proton and 2.857, 2.864 Å in the independent half protonated QM molecule).

The crystallographic analysis of a single unit also shows the existence of one and a half triflate ions that carry an overall charge of -1.5. The data were consistent with the existence of two electron density peaks, carrying an overall charge of +1.5 representing the two protons found near the carbonyl oxygens on the QM fragments. One of those peaks is found approximately equidistant from O4A and O4C, which suggests that one H atom is shared with both O atoms (Figure **3.7**). However, the other proton peak is attached to O4B, which is donor to O4B* (O4B* = O atom related to O4B by one inversion center), and its occupancy factor must be 0.5 as there would be an impossibly short O4B−H4B···H4B*−O4B* (the starred atoms are generated by inversion symmetry) contact otherwise. Contoured difference Fourier maps show unequivocally the existence of those two peaks (Figure **3.8**).
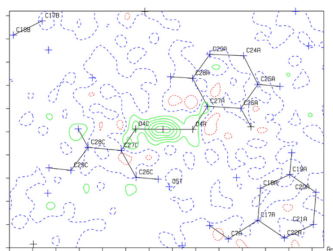
Figure 3.7. Contoured Fourier map of the proton shared by the two p-QM molecules (O4A and O4C represent the carbonyl oxygen atoms of the QM moieties).
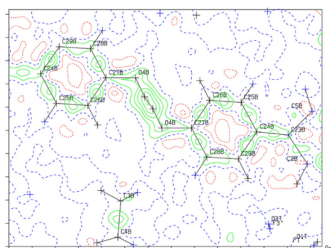
Figure 3.8. Contoured Fourier map of the independent hydrogen bound proton (O4B represents the carbonyl oxygen of the QM attached to the proton whereas O4B* denotes the oxygen atom on QM generated by the Mercury program).
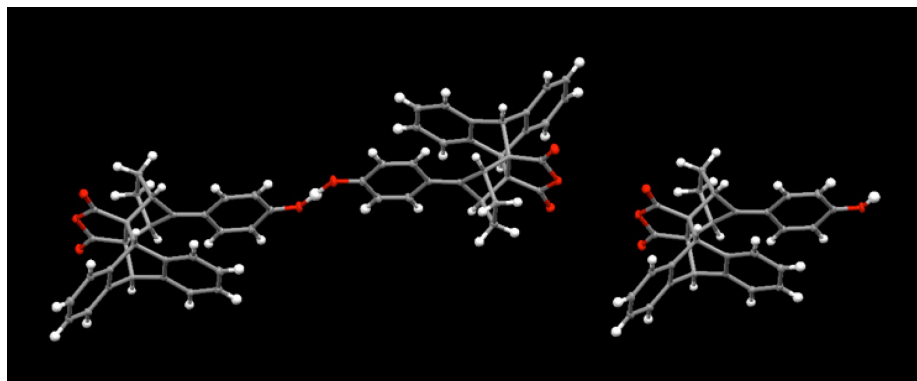
Figure 3.9. *Crystal structure of the protonated-hydrogen bonded forms of p-QM **1**. The asymmetric crystal unit contains three target molecules and one and a half triflate counterions (TfO⁻ counterions have been removed for clarity).*

Finally, we turned back to DFT calculations in order to compare the X-ray structure with an optimized geometry for a carbocation-π interaction in a system resembling cation **2** but lacking structural constraints. DFT calculations (at ωB97XD/6-311+G**) predict that in model system A (Figure **3.10**), the carbocation-π interaction manifests itself similarly, although with stricter coplanarity of the aromatic and p-QM rings and loss of C_s symmetry.
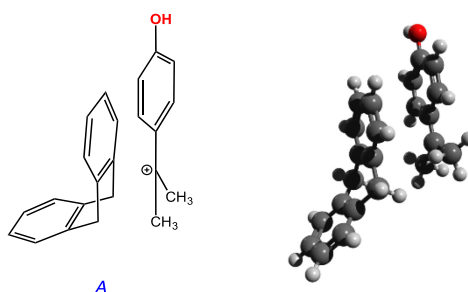
Figure 3.10. *Model system **A** used for comparing the optimized geometry of carbocation$-\pi$ interactions with cation **2** and its optimized geometry at ωB97XD/6-311+G**.*

3.3 Conclusion

We have reported the spectroscopic and crystallographic analysis of a cation generated by the facile protonation of aliphatic p-QM **1**. Both calculations and experimental data suggest that it is stabilized by

partial aromatization of the QM fragment as well as a modest through-space carbocation-π interaction with the neighboring aromatic ring. A single crystallographic unit contains three p-QM molecules sharing two protons with an overall charge of +1.5, along with one and a half triflate counterions. Finally, this protonated p-QM provides a rare experimental example of a simple, crystallizable chemical system that allows the direct study of a carbocation-π interaction.

3.4 References

1. Mahadevi, A. S.; Sastry, G. N. *Chem. Rev.* **2013,** *113*, 2100-2138.

2. Hong, B. H.; Bae, S. C.; Lee, C. W.; Jeong, S.; Kim, K. S. *Science* **2001,** *294*, 348-351.

3. Dougherty, D. A. *Acc. Chem. Res.* **2013,** *46*, 885-893.

4. Faraldos, J. A.; Antonczak, A. K.; Gonzalez, V.; Fullerton, R.; Tippmann, E. M.; Allemann, R. K. *J. Am. Chem. Soc.* **2011,** *133*, 13906-13909.

5. Dougherty, D. A. *Science* **1996,** *271*, 163-168.

6. Torrice, M. M.; Bower, K. S.; Lester, H. A.; Dougherty, D. A. *P. Natl. A. Sci. U. S. A.* **2009,** *106*, 11919-11924.

7. Sunner, J.; Nishizawa, K.; Kebarle, P. *J. Phys. Chem.* **1981,** *85*, 1814-1820.

8. Kim, D.; Hu, S.; Tarakeshwar, P.; Kim, K. S. *J. Phys. Chem. A.* **2003,** *107*, 1228-1238.

9. Shepodd, T. J.; Petti, M. A.; Dougherty, D. A. *J. Am. Chem. Soc.* **1986,** *108*, 6085-6087.

10. Petti, M. A.; Shepodd, T. J.; Barrans, R. E.; Dougherty, D. A. *J. Am. Chem. Soc.* **1988,** *110*, 6825-6840.

11. Kearney, P. C.; Mizoue, L. S.; Kumpf, R. A.; Forman, J. E.; McCurdy, A.; Dougherty, D. A. *J. Am. Chem. Soc.* **1993,** *115*, 9907-9919.

12. Christianson, D. W. *Chem. Rev.* **2006,** *106*, 3412-3442.

13. Chang, C. H.; Wen, H. Y.; Shie, W. S.; Lu, C. T.; Li, M. E.; Liu, Y. T.; Li, W. H.; Wu, T. K. *Org. Biomol. Chem.* **2013,** *11*, 4214-4219.

14. Ito, R.; Hashimoto, I.; Masukawa, Y.; Hoshino, T. *Chem. Eur. J.* **2013,** *19*, 17150-17158.

15. Ma. J. C.; Dougherty, D. A. *Chem. Rev.* **1997,** *97*, 1303-1324.

16. Miklis, P. C.; Ditchfield, R.; Spencer, T. A. *J. Am. Chem. Soc.* **1998,** *120*, 10482-10489.

17. Oliveira, F. G.; Esteves, P. M. *J. Braz. Chem. Soc.* **2011,** *22*, 1979-1986.

18. Ditchfield, R.; Spencer, T. A. *Tetrahedron Lett.* **2011,** *52*, 3674-3677.

19. Ditchfield, R.; Spencer, T. A. *Org. Biomol. Chem.* **2016,** *14*, 9543-9548.

20. Prakash, G. K. S.; Farnia, M.; Keyanian, S.; Olah, G. A.; Kuhn, H. J.; Schaffner, K. *J. Am. Chem. Soc.* **1987,** *109*, 911-912.

21. Kazim, M.; Siegler, M. A.; Lectka, T. *Org. Lett.* **2019,** *21,* 2326-2329.

22. Cook, C. D.; Norcross, B. E. *J. Am. Chem. Soc.* **1956,** *78*, 3797-3799.

23. Hehre, W. J.; Ditchfield, R.; Radom, L.; Pople, J. A. *J. Am. Chem. Soc.* **1970,** *92*, 4796-4801.

Chapter 4: Discovery and Mechanistic Study of a Totally Organic $C_{(aryl)}$–$C_{(alkyl)}$ Oxygen Insertion Reaction

4.1 Introduction

The insertion of an oxygen atom into a C-C bond is often facile when one of the carbon atoms is part of an acyl group. The archetypical example, the eponymous Baeyer-Villager insertion reaction,[1] is synthetically highly useful[2] and its mechanistic details, highly reliant on nucleophilic attack on the carbonyl, are straightforward and well-understood.[3] One established pathway involves nucleophilic attack of peroxide at the electrophilic acyl carbon; thereupon alkyl (or aryl) migration results in scission of the weak O-O bond and formation of the product (Figure **4.1**).
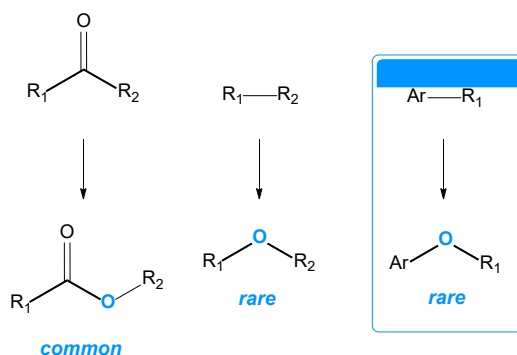
Figure 4.1. *Oxygen insertion motifs.*

On the other hand, insertion of an oxygen atom into other types of C-C bonds varies from extremely rare to all but nonexistent. Insertion of an oxygen atom from O_2 itself presents an even greater level of complexity as a stronger bond must be broken in the process. Selective insertion into a $C_{(aryl)}$-$C_{(alkyl)}$ bond is known in only a very few instances; the most notable example involves the work of Cristobal et al.[4] wherein an oxygen atom is inserted into an $C_{aromatic}$-C_{sp}^3 carbon of a transition metal complex. In this system, the presence of a proximate N-H bond and an iridium center are necessary for the oxygen insertion to proceed. In any case, the mechanism by which this oxygenation occurs remains mysterious and its understanding out of reach, such that the authors themselves state: "it has to be noted that, as in the case of many O_2 mediated

reactions with organic or organometallic substrates, it is not possible to advance mechanistic proposals for the oxidations described herein." The present system, as shall be seen, proves more amenable to mechanistic investigation.

4.2 Results and Discussion

Our studies began with recently reported para quinone methide (p-QM) **1**,[5] which displays a variety of unusual reaction chemistry. We photolyzed p-QM **1** at various wavelengths with the rather vague goal of inducing a dimerization reaction, known to happen in other quinone methides.[6] Instead we observed a highly selective oxygen insertion reaction at the *proximate* aromatic ring (Scheme **4.1**). Evidently the trace amounts of oxygen in the reaction mixture sufficed to ensure conversion. When the reaction is run under a pure oxygen atmosphere, both the rate and yield (90% conversion by NMR) of the reaction increase markedly. The ^{1}H NMR of the product reveals that the mirror plane bisecting the starting material has been annihilated. Unlike in p-QM **1**, the bridge protons appear at different chemical shifts, i.e., 3.45 and 3.88 ppm for the allylic protons and 4.16 and 5.5 ppm for the benzylic bridge protons. The precise structure of the product was confirmed by X-ray crystallography (Figure **4.2**).
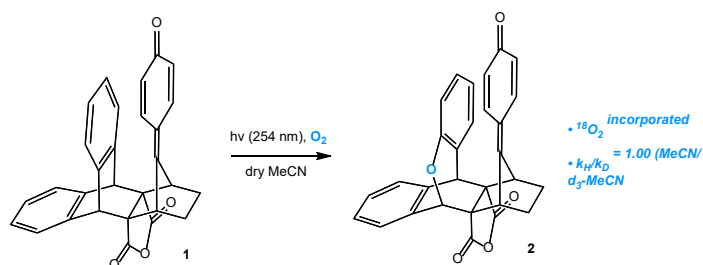
Scheme 4.1. *Photooxygenation of p-QM* **1**.
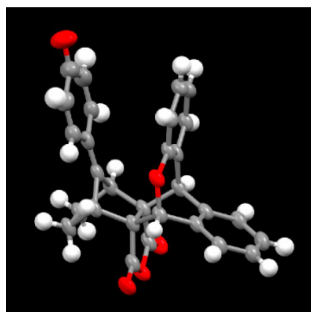
Figure 4.2. *X-ray crystal structure of* **2**.

21

4.3 Mechanistic Studies

The first and most important clue is stereochemical. As stated, the oxygenation reaction occurs exclusively across a C-C bond proximal to the QM moiety, suggesting its involvement in an important way. With this hint in mind, we undertook some simple control experiments to narrow the range of mechanistic possibilities. For example, ketone **3**[7] undergoes *no* oxygenation (no transformation whatsoever) under identical conditions, confirming that the QM moiety is necessary for oxygenation to occur. Moreover, ketone **3** also fails to oxygenate (at all wavelengths probed) in the presence of singlet oxygen sensitizers (e.g. Rose Bengal[8]) and strong excited state electron acceptors such as 1,2,4,5-tetracyanobenzene.[9] In all cases, ketone **3** was quantitatively recovered (Scheme **4.2**).

Conclusive evidence for the source of the incorporated oxygen atom comes from a simple labeling study employing $^{18}O=^{18}O$ gas, whereupon the ^{18}O label appears cleanly in the product. The role of the solvent provides additional clues; photolysis works comparably well in MeCN, PhCN, and t-BuCN, whereas photolysis in PhCF$_3$ and other aprotic solvents (also oxygenated) results in recovered starting material. The kinetic isotope effect (KIE) for photolysis in d$_3$-MeCN is approximately 1.0.
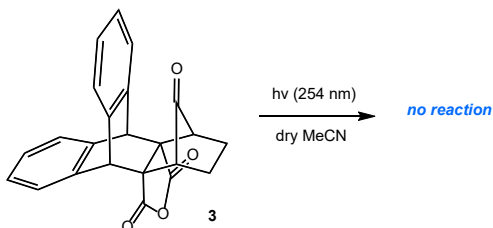
Scheme 4.2. Photooxygenation of control **3**.

Several conclusions can be drawn from these results: 1) protic solvents are not necessary for successful oxygenation, suggesting that hydrogen atoms (or protons) are not transferred at any point in the process; 2) the lack of a hydrogen-based KIE is also congruent with this fact. 3) Non-nitrilic, non-protic solvents, in contrast, produce *no oxygen insertion product.*   4) Nitrile-based solvents are apparently necessary for success, suggesting a *chemical role* for them in the mechanism. 5) In the presence of water, oxygenation is overridden in favor of hydrolysis, a fact that will be discussed below. With these data in hand, a plausible

mechanistic scenario takes shape that is supported by both experiments and calculations (Scheme **4.3**).

Excitation (254 nm) produces an aromatic ring centered excited state (1_{S1}*) that engages in intramolecular

cyclization with the proximate QM moiety[10] through a barrierless transition state **TS1$_{S1}$** located 65.1 kcal

mol^{-1} above the starting substrate 1_{S1} (calculations performed at the IEFPCM[MeCN] M06-2X/6-

311+G(2d,2p)//B3LYP/6-31G(d) level using the program Gaussian 09). The key features of this transition

state being a C-C bond breaking and forming distances of 2.21 Å and 1.66 Å respectively leading to relatively

stable benzyl diradical **4$_{S1}$** with a lifetime sufficient to trap molecular oxygen (still a fast process). The

reaction of O_2 with free radicals is known to be rapid,[11] and in this case, results in the triplet peroxyradical

5$_{T1}$, which is electrophilic at the peroxyl group and relatively more nucleophilic at the phenol oxygen

(calculated NBO charges of -0.18 eV and -0.58 eV respectively). Reaction with the abundant solvent (namely

a nitrile of some sort) then occurs to afford intermediate **6$_{T1}$**. With the stage set – the orbital alignment

excellent and electronic polarization optimal – facile scission of the O-O bond (distance 1.60 Å) by **TS2$_{T1}$**

with a computed Gibbs free activation energy ($\Delta G^{\neq}$) of only 0.1 kcal mol^{-1}, releases a transient, putative

nitrile oxide[12] byproduct and diradical **7$_{T1}$**. This diradical species, stereoelectronically well positioned for

pseudoaxial oxygen attack upon neighboring aromatic ring, then reacts to form resonance stabilized aryl

radical **8$_{T1}$** by C-O bond forming (distance = 1.92 Å) transition state **TS3$_{T1}$** with an activation barrier of 10.4

kcal mol^{-1}. Subsequent C-C bond homolysis by **TS4$_{T1}$** displaying a C-C bond breaking distance of 2.17 Å

(calculated $\Delta G^{\neq}$ = 13.3 kcal mol^{-1}), forms triplet state intermediate **2$_{T1}$**. Finally, relaxation to the ground

state affords singlet state product **2** corresponding to computed **2$_{S1}$** (Scheme **4.3**).

In solutions containing CH_3OH, a competent hydrogen atom donor,[13] radical **4$_{S1}$** can be intercepted as

reduced product **10**, offering us a "snapshot" of the reaction in progress (Scheme **4.4**). In aqueous solutions,

the reaction path is somewhat different. The biradical reacts as a zwitterion (suggesting a singlet state)

with water in an overall photohydration.[14] In fact, irradiation in a mixture of MeCN/H_2O results in exclusive

formation of alcohol **11** (Scheme **4.4**). These results also bolster the hypothesis that the nitrile nitrogen

atom (instead of hydrogen atoms) must intercept diradical **5$_{T1}$**.
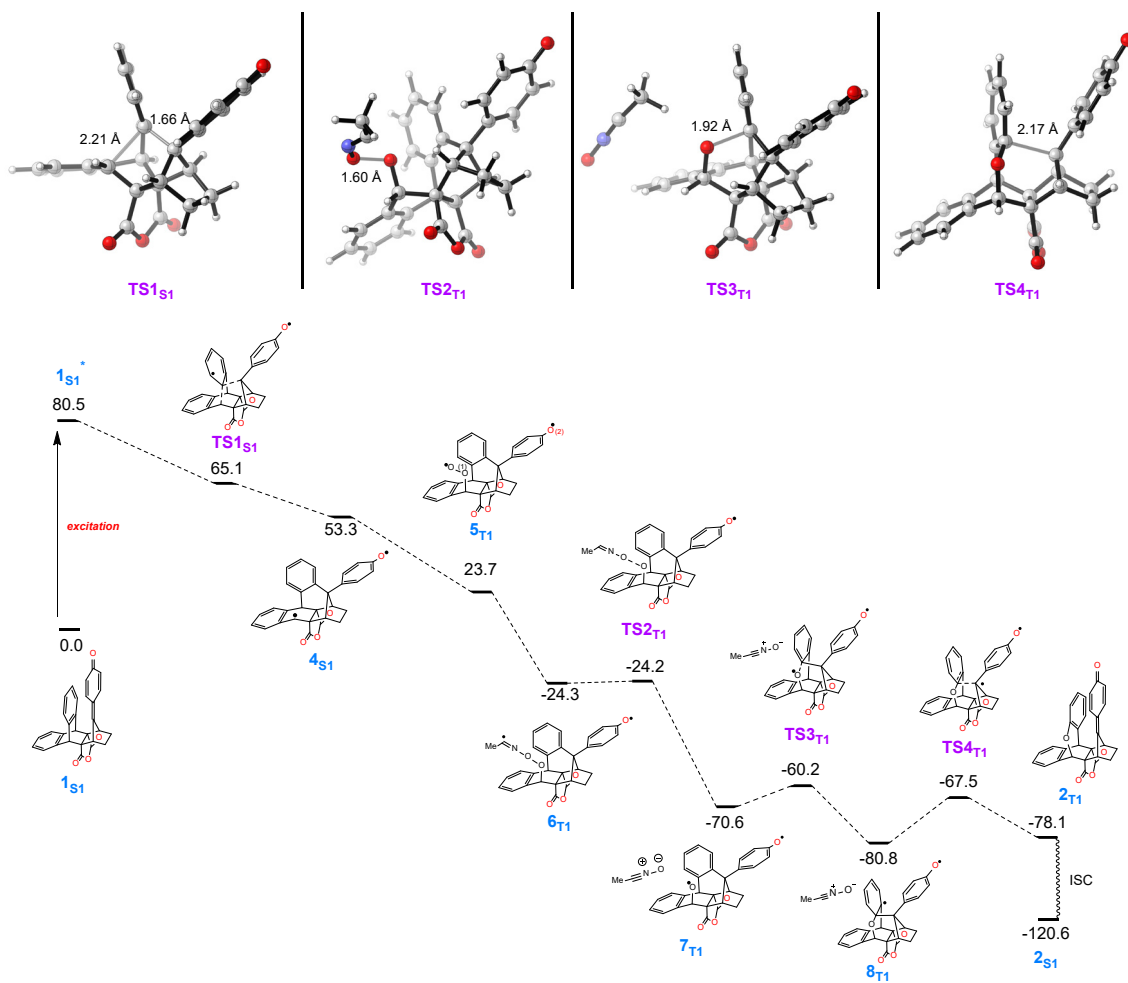
Scheme 4.3. *Proposed mechanism for oxygen insertion into **1**.*
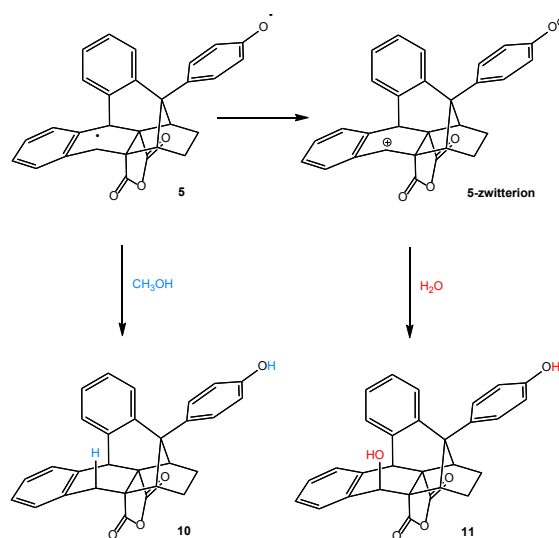
Scheme 4.4. *Photoreduction and photohydration alternatives.*

4.4 Conclusion

We have chronicled an unusual photooxygenation reaction in stable p-quinone methide (p-QM) **1**. Mechanistic details point to the criticality of the p-QM moiety, the excitation of an adjacent aromatic ring, diradical intermediates, and also to the indispensable nitrile solvent. Although fairly unique and complex, the results described herein may eventually point the way towards making oxygen insertions more general (e.g. the use of a stable, exogenous QM photocatalyst). Further investigations toward this goal are now underway.

4.5 References

1. a) Baeyer, A.; Villiger, V. *Ber. Dtsch. Chem. Ges.* **1899**, *32*, 3625-3633; b) Baeyer, A. Villiger, V. *Ber. Dtsch. Chem. Ges.* **1900**, *33*, 858-864.

2. a) Zhou, L.; Lin, L.; Liu, X.; Feng, X. in *Molecular Rearrangements in Organic Synthesis*, ed. Rojas, C. M. Wiley-VCH, Weinheim, Germany, 2015, p. 35-57; b) ten Brink, G.-J.; Arends, I. W. C. E.; Sheldon, R. A. *Chem. Rev.* **2004**, *104*, 4105-4123; c) Krow, G. R. *Org. React.* **1993**, *43*, 251-798; d) Renz, M.; Meunier, B. *Eur. J. Org. Chem.* **1999**, *4*, 737-750; e) Strukul, G. *Angew. Chem., Int. Ed.* **1998**, *37*, 1198-1209.

3. a) Werner, A.; Piguet, A. *Ber. Dtsch. Chem. Ges.* **1904**, *37*, 4295-4315; b) Wittig, G. Pieper, G. *Ber. Dtsch. Chem. Ges.* **1940**, *73*, 295-297; c) Criegee, R.; Schnorrenberg, W.; Becke, J. *Justus Liebigs Ann. Chem.* **1949**, *565*, 7-21; d) Criegee, R. *Justus Liebigs Ann. Chem.* **1948**, *560*, 127-135; e) Doering, W.; Dorfman, E. *J. Am. Chem. Soc.* **1953**, *75*, 5595-5598; f) Doering, W.; Speers, L. *J. Am. Chem. Soc.*, 1950, **72**, 5515-5518.

4. Cristobal, C.; Alvarez, E.; Paneque, M.; Poveda, M. L. *Organometallics* **2013**, *32*, 714-717.

5. a) Kazim, M.; Siegler, M. A.; Lectka, T. *Org. Lett.* **2019**, *21*, 2326-2329; b) Kazim, M.; Siegler, M. A.; Lectka, T. *J. Org. Chem.*, 2019, **84**, 8284-8288.

6. a) Turner, A. B. *Q. Rev. Chem. Soc.* **1964**, *4*, 347-360; b) Cook, C. D.; Norcross, B. E. *J. Am. Chem. Soc.* **1959**, *81*, 1176-1180; c) Bauer, R. H.; Coppinger, G. M. *Tetrahedron* **1963**, *19*, 1201-1206.

7. a) Guan, L.; Holl, M. G.; Pitts, C. R.; Struble, M. D.; Siegler, M. A.; Lectka, T. *J. Am. Chem. Soc.* **2017**, *139*, 14913-14916; b) Holl, M. G.; Struble, M. D.; Singal, P.; Siegler, M. A.; Lectka, T. *Angew. Chem.* **2016**, *128*, 8406-8409.

8. a) Kochevar, I. E.; Redmond, R. W. *Methods Enzymol.* **2000**, *319*, 20-28; b) Ludvikova, L.; Fris, P.; Heger, D.; Sebej, P.; Wirz, J.; Klan, P. *Phys. Chem. Chem. Phys.* **2016**, *18*, 16266-16273.

9. a) Tsujimoto, K.; Nakao, N.; Ohashi, M. *J. Chem. Soc. Chem. Commun.* **1992**, *4*, 366-367; b) Albini, A.; Mella, M.; Freccero, M. *Tetrahedron* **1994**, *50*, 575-607; c) Koshima, H.; Ding, K.; Chisaka, Y.; Matsuura, T.; Ohashi, Y.; Mukasa, M. *J. Org. Chem.* **1996**, *61*, 2352-2357.

10. For related reactions of p-QMs see a) Zhao, K.; Zhi, Y.; Shu, T.; Valkonen, A.; Rissanen, K.; Enders, D. *Angew. Chem., Int. Ed.* **2016**, *55*, 12104-12108; b) He, F. S.; Jin, J. H.; Yang, Z. T.; Yu, X.; Fossey, J. S.; Deng, W. P. *ACS Catal.* **2016**, *6*, 652-656.

11. Maillard, B.; Ingold, K.; U. Scaiano, J. C. *J. Am. Chem. Soc.* **1983**, *105*, 5095-5099.

12. Efforts to trap the putative nitrile oxide proved unsuccessful, as all suitable trapping agents unfortunately interfered with the oxygenation insertion itself. Given that the oxygenations were performed on very small scale by necessity, the nitrile oxide would be formed in miniscule amounts.

13. Boyle Jr. W. J.; Bunnett, J. F. *J. Am. Chem. Soc.* **1974**, *96*, 1418-1422.

14. a) Marshall, J. A. *Acc. Chem. Res.* **1969**, *2*, 33-40; b) Kropp, P. J. *J. Am. Chem. Soc.* **1967**, *89*, 3650-3652; c) McCall, M. T.; Whitten, D. G. *J. Am. Chem. Soc.* **1969**, *91*, 5681-5682; d) Kropp, P. J.; Krauss, H. J. *J. Am. Chem. Soc.* **1967**, *89*, 5199-5208; e) Brousmiche, D. W.; Xu, M.; Lukeman, M.; Wan, P. *J. Am. Chem. Soc.* **2003**, *125*, 12961-12970.

Chapter 5: A DFT Case Study of the Mechanism of a Metal-Free Oxygen Atom Insertion into a *p*-Quinone Methide C(sp^3)–C(sp^2) Bond

5.1 Introduction

Oxygen atom insertion is a fundamental transformation in both biological and chemical settings, as often called upon in the construction of ethers, esters and alcohols from ubiquitous C–H and C–C bonds. From a biological standpoint, the cytochrome P450 enzymes are well-known for their ability to facilitate oxygen atom insertion events providing bioactive compounds and related natural products, though the mechanism of these processes is an often-debated topic.[1]

The venerable Baeyer–Villiger reaction, in contrast, is a commonly employed synthetic strategy for preparing esters and lactones from carbonyl-containing substrates.[2] In large part, the widespread use of this reaction derives from an understanding of the mechanism, thus, demonstrating how with mechanistic insight, utility and experimental implementation follow. The mechanistic details of this reaction—involving nucleophilic attack of peroxide at an electrophilic acyl carbon—whereupon alkyl (or aryl) migration follows with concomitant scission of the weak O–O peroxy-bond furnishes RCO$_2$R' functional group-containing products. Notwithstanding, an inherent feature of this reactivity is the presence of a carbonyl group fulfilling the important role of directing C–C bond activation for oxygen atom insertion, in addition to the migratory aptitude of groups and stereoelectronic effects[3] (Figure **5.1A**).

Alternatively, oxygen atom insertion into intrinsically inert C–C bonds, e.g., C(sp^3)–C(sp^2) bonds is a more formidable challenge, especially when attempting to enable site-selectivity. This is especially true if dioxygen is the source of oxygen, despite its abundance. Nevertheless, this type of reactivity holds great potential, e.g., in photodynamic therapies, and recycling and synthesis as a powerful strategy for the rapid construction of molecular complexity utilizing readily available oxygen.[4] The key to unlocking this reactivity, arguably, is through mechanistic understanding, hand-in-hand with experimental investigations.

In this regard, we recently reported the synthesis of a *p*-quinone methide (*p*-QM) (**1**, Figure **5.1B**) that upon

photolysis, in the presence of trace amounts of oxygen, underwent a highly selective oxygen insertion

reaction at the proximate aromatic ring, as confirmed by ^{1}H NMR, ^{13}C NMR, and X-ray crystallography.[5c]

This type of reactivity is less commonly encountered, and, thus, represents one among a very few instances

of selective oxygen atom insertion into an intrinsically inert $C(sp^3)$–$C(sp^2)$ chemical bond. On a related

note, underscoring the emerging importance of oxygen atom insertion is a recent report by the Aratani

and Yamada groups, wherein direct oxygen atom insertion into a biaryl $C(sp^2)$–$C(sp^2)$ σ-bond was achieved[6]

(Figure **5.1B**).
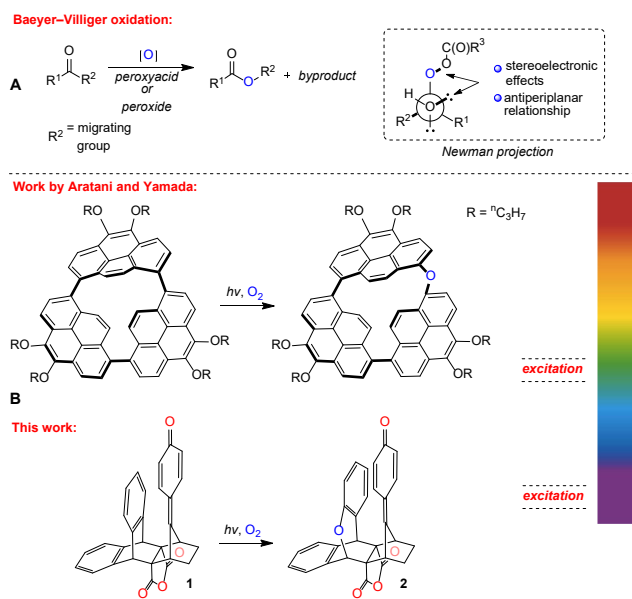
Figure 5.1. *(A) General depiction of a Baeyer-Villiger oxidation. (B) Existing strategies showcasing oxygen atom insertion into different bonds.*

A common theme between both of these disclosures was alleviation of strain, e.g., angle strain (Baeyer

strain) and torsional strain (Pitzer strain) as intrinsic features for driving reactivity forward.[7] Incidentally, in

terms of *p*-QM (**1**) we proposed a preliminary rationale for oxygen insertion; however, upon deeper

consideration it became evident further investigation was required to explain the reactivity of this system.

Toward this aim, there were a number of aspects needing to be addressed and/or further clarified, including

(i) the role of solvent (acetonitrile), (ii) the absence of nitrile-derived byproducts, (iii) the possibility of H_2O-

facilitated reaction pathway(s), and, (iv) ultimately, a rigorous mechanistic investigation of different, presumably viable, modes of reactivity. Accordingly, herein we describe a computational investigation exploring nonmetal-based oxygen atom insertion into $C(sp^3)$–$C(sp^2)$ bonds using a *p*-QM substrate (**1**) as an exemplar case. We posit that this disclosure will help evolve understanding of the mechanistic details inherent to photochemical processes.

5.2 Results and Discussion

Strain and Photo-Induced Reactivity. Density functional theory (DFT) and time-dependent (TD)-DFT calculations at the $((IEFPCM)_{(CH3CN)})UB3LYP-D3/6-311++G(2d,2p)//UB3LYP/6-31G(d)$ level of theory were performed using the Gaussian 09 program[8,9,10] to gain insight into the mechanism at hand. Accordingly, with the aim of clarifying the basis of site-selective oxygen atom insertion into the $C(sp^3)$–$C(sp^2)$ bridgehead bond of *p*-QM (**1**), several underlying contributors came to the forefront (Figure **5.2**). As a point of departure, we sought to gain insight into the susceptibility of the bridgehead C–C bond, which was observed to undergo cleavage experimentally. In probing this aspect, using the X-ray crystal structure coordinates of *p*-QM (**1**) as input, *in silico* optimization provided computed *p*-QM with nearly identical structural features, e.g., bond distances, angles, etc.[5c]

Notably, the computed bond dissociation Gibbs free energy (BDFE) of the bridgehead bond of **1** equated to 61.4 kcal mol^{-1} well below typical C–C bond strengths, e.g., Ph-Me with a BDFE of 102 kcal mol^{-1}.[11] The weakening of this bond, in part, derives from steric repulsion between the *p*-QM and proximal aryl bridgehead carbons as conferred by short C⋯C distances of 2.99 Å, a metric well below the sum of the van der Waals radii of two carbons (Pauling van der Waal radius of C = 1.70 Å).[12] Further were various aberrant angles and torsions throughout the polycyclic framework resulting in Baeyer strain, e.g., $\theta_{C(1)-C(2)-C(5)} = 105.9°$, $\theta_{C(2)-C(5)-C(26)} = 116.2°$, $\theta_{C(26)-C(30)-C(28)} = 97.4°$.
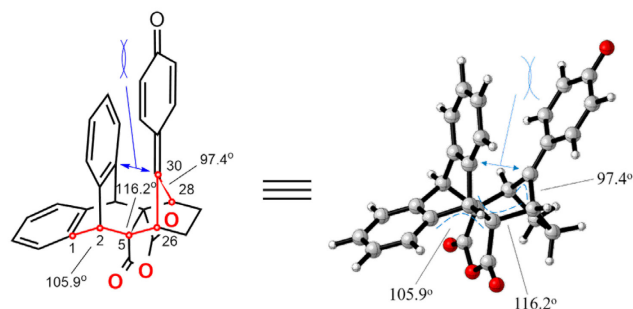
Figure 5.2. *Figure 2. 2D (left-hand side) and 3D (right-hand side) structures of 1 with a few bond angles identified.*
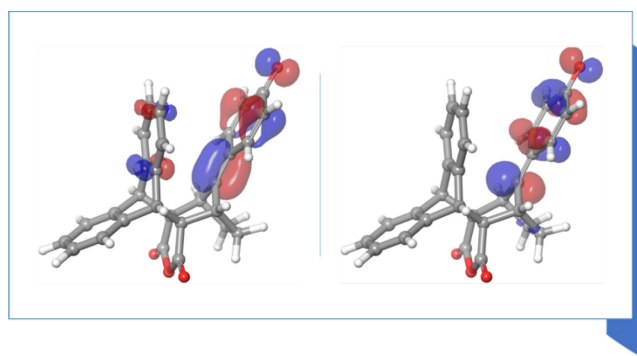
Figure 5.3. *Computed (UB3LYP-D3/6-311++G (2d,2p)//UB3LYP/6-31G(d)) HOMO (left-hand side) and LUMO (right-hand side) of 1.*

Associated with these elements of strain was the important role of the *p*-QM moiety in triggering reactivity as clearly seen from the computed highest occupied molecular orbital (HOMO) and lowest unoccupied molecular orbital (LUMO) of *p*-QM (**1**) with orbital densities completely localized on the quinone ring moiety (Figure **5.3**).

Pathways 1–4. With a glimpse into the inherent strain and indispensable role of the *p*-QM moiety of **1**, our attention turned to examining several reaction scenarios deemed most probable. Collectively, these differing processes defined four pathways, all of which featured pivotal peroxyradical **5**$_{T1}$ and/or benzyl diradical **4**$_{T1}$ (Figures **5.4, 5.5,** and **5.7**, pathways 1–4).
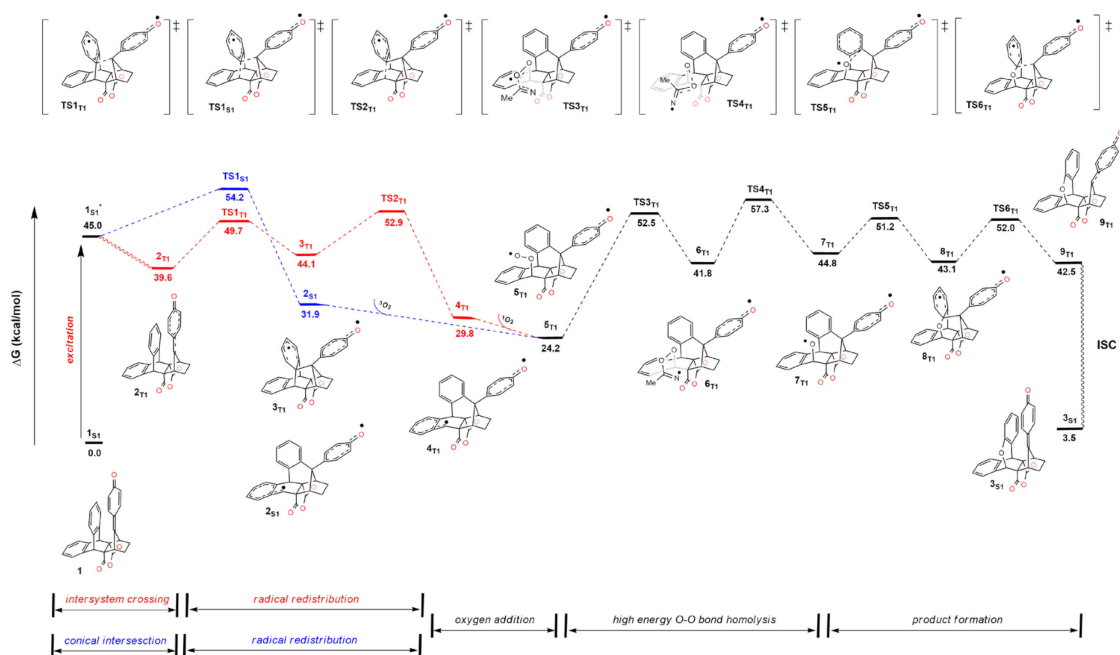
Figure 5.4. *Comparative free energy profiles for oxygen atom insertion via pathways 1 (blue) and 2 (red). These profiles share a common pathway upon formation of intermediate 5_{T1}.*

A brief overview of computed pathways **1** and **2** reveals great differences between them until intermediate 5_{T1}, primarily the involvement of singlet vs. triplet dioxygen, wherein the two pathways converged after 5_{T1} to provide product 3_{S1}. Markedly, only singlet state species were involved in the steps preceding intermediate 5_{T1} in pathway **1** (blue line), whereas pathway **2** proceeded through intersystem crossing (ISC) following photolysis, wherein rearrangement of the bicyclo[2.2.2]-framework of **1** occurred. Here, two distinct steps were found to exist with the intermediates being triplet state species (pathway 2, red line) (Figure **5.4**).

Taking a finer look at the mechanistic details of pathway 1, excited state intermediate $1S_1^*$, residing 45.0 kcal mol^{-1} above ground state starting structure $1S_1$ on the reaction coordinate diagram, initially forms following the absorption of a photon of light. Either internal conversion back to the ground state or propagation forward along the reaction pathway then occurs with the latter involving funneling through a conical intersection emptying onto the ground state surface at intermediate 2_{S1} via transition state **TS1$_{S1}$**, displaying C···C bond making and breaking distances of 1.66 and 2.21 Å (Figure **5.4**). Singlet state

intermediate 2_{S1} next reacts with triplet dioxygen to furnish intermediate 5_{T1}, with spin density localized

on the quinone ring and the peroxyradical group, clearly foreshadowing subsequent reactivity (Figure **5.6**).

With the stage set, peroxyradical oxygen addition to the abundant solvent occurs by energetically

demanding transition state **TS3$_{T1}$** (calculated $\Delta G^{\ddagger}$ = 28.3 kcal mol^{-1}) featuring a C···O bond forming distance

of 1.75 Å. This endergonic process leads to iminyl radical 6_{T1}, wherein the spin is dispersed across the

quinone ring and the peroxy-iminyl substructure. Subsequent O–O bond homolysis (transition state **TS4$_{T1}$**)

with a O···O bond breaking distance of 2.10 Å and moderate Gibbs free energy activation barrier ($\Delta G^{\ddagger}$) of

15.5 kcal mol^{-1} is then surmounted to provide triplet state intermediate 7_{T1}, concomitant with a putative

nitrile-derived oxaziridine-like byproduct. Thereafter, attack of the oxygen-centered radical of 7_{T1}, upon

the neighboring aromatic ring, ensues to form resonance-stabilized aryl radical 8_{T1} by C···O bond forming

(distance = 1.91 Å) transition state **TS5$_{T1}$** with a calculated activation barrier of 6.40 kcal mol^{-1}. At that

stage, C–C bond homolysis by **TS6$_{T1}$**, displaying a C···C bond breaking distance of 2.17 Å and calculated

activation barrier of 8.90 kcal mol^{-1}, forms triplet state intermediate 9_{T1}. Finally, relaxation to the ground

state affords computed singlet state product 3_{S1} corresponding to product **2**.

As for pathway 2, initial intersystem crossing from 1_{S1}^{*} furnishes triplet state intermediate 2_{T1}, which is

39.6 kcal mol^{-1} less stable than starting p-QM (**1**) and dominated by QM ring-localized spin density (Figures

5.4 and **5.6**). Quinone methide and proximal aryl ring C–C bond formation (distance = 2.12 Å) coupled to

migration of quinone ring spin density onto the neighboring aryl ring then occurs by transition state **TS1$_{T1}$**

with an activation energy of 10.1 kcal mol^{-1}. The resulting resonance-stabilized aryl radical 3_{T1} then

undergoes C–C bond scission (distance = 2.07 Å) by transition state **TS2$_{T1}$** with an activation barrier of 8.80

kcal mol^{-1} to furnish benzyl diradical 4_{T1}, wherein the spin density is localized on the quinone ring and

benzylic carbon (Figure **5.6**). At that point, reaction with singlet dioxygen, presumably generated by

oxygen quenching of 1_{S1}^{*} with p-QM (**1**) playing the role of a sensitizer and light,[13] affords peroxyradical

5_{T1}. Thereafter, and as noted above, the remaining steps of this pathway mirror that of pathway 1.

In stepping back and generalizing to the overall feasibility of these two pathways, both are fraught with

the unfavorable energetics of proceeding through transition state **TS3$_{T1}$**, that is, capture of the solvent—

provided the viability of ISC or the event of a conical intersection. Taking this into consideration, these two pathways, nonetheless, offer a more probable mechanism for formation of $\mathbf{3_{S1}}$ from $\mathbf{1_{S1}}$ than highly unfavorable peroxyradical addition to the solvent (singlet state) nitrile nitrogen[5c] $\mathbf{S6_{T1}}$ (calculated $\Delta G^{\ddagger}$ = 78.1 kcal mol^{-1}).
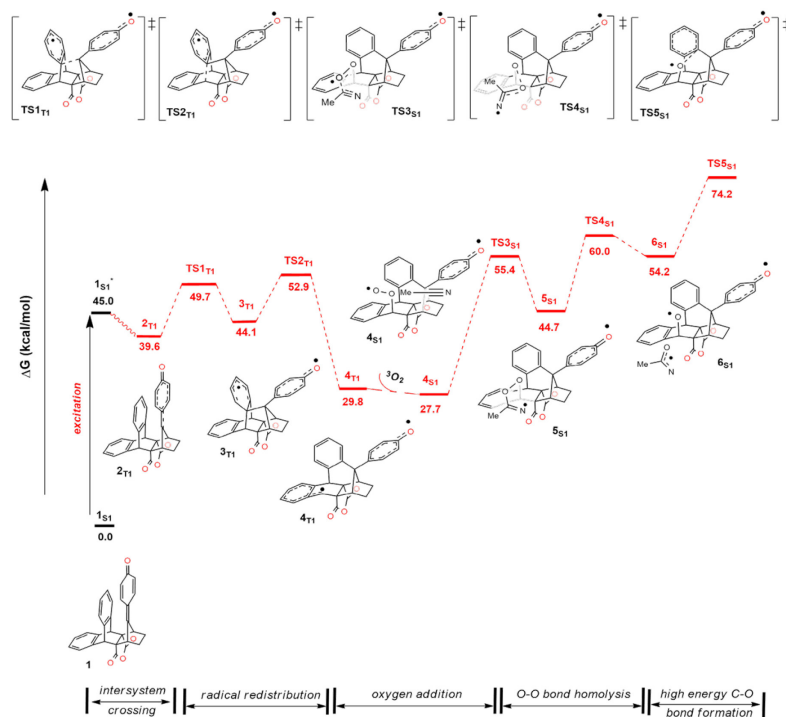
Figure 5.5. *Free energy profile for oxygen atom insertion via pathway 3. This reaction pathway was truncated at high energy transition state TS5$_{S1}$.*

Pathway 3, as a less viable option, builds upon elements of pathways 1 and 2, wherein the common denominator appears to be intermediate $\mathbf{4_{T1}}$ that utilizes triplet state oxygen to provide marginally more stable intermediate $\mathbf{4_{S1}}$ (Figure **5.5**). This singlet state intermediate then reacts with solvent by energetically demanding transition state $\mathbf{TS3_{S1}}$, which is 27.7 kcal mol^{-1} less stable than intermediate $\mathbf{4_{S1}}$. The product of solvent capture (intermediate $\mathbf{5_{S1}}$) then undergoes O–O bond homolysis (distance = 1.97 Å) by transition state $\mathbf{TS4_{S1}}$ affording oxygen-centered radical $\mathbf{6_{S1}}$. At that point, oxygen addition to the nearby aryl ring was computed to be highly unfavorable with an activation barrier of 20.0 kcal mol^{-1} for surmounting transition state $\mathbf{TS5_{S1}}$, located well above $\mathbf{1_{S1}}$ or, for that matter, $\mathbf{1_{S1}}^{*}$. Given this escalating

energetic profile, and, with it, infeasibility of this mechanistic scenario, further investigation of this pathway was not pursued. Finally, having ruled this pathway out as a possibility we explored one final option, namely pathway 4.
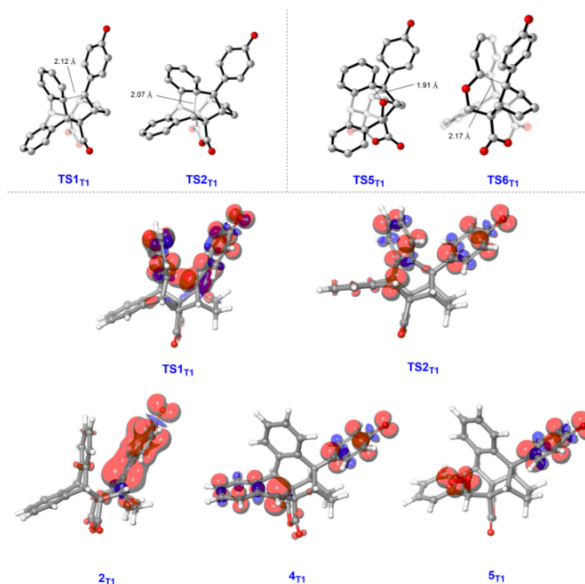
Figure 5.6. *Calculated geometries of transition state structures (triplet state) with key bond metrics shown in Å, along with spin densities of prominent transition states and intermediates.*

Pathway 4, in reserving principle elements of pathway 2, affords 3_{S1} from 1_{S1} by a series of energetically favorable steps making this pathway the most feasible among the pathways investigated (Figure **5.7**). The finer details of pathway 4 similarly evolve until triplet state peroxyradical 5_{T1}. At that juncture, peroxyradical 5_{T1} combines with benzyl diradical 4_{T1}, despite a slight entropic penalty, to provide a more stable dimer intermediate (7_{S1}) located 8.5 kcal mol^{-1} below triplet state precursor 5_{T1} on the reaction coordinate by a process (ETS_{T1}) with an estimated activation barrier of 14.0 kcal mol^{-1} determined from BDFE values. Dimer break-up affording 7_{T1} from 7_{S1}^{*} by a well-defined first-order saddle point was also investigated; however, this enterprise proved intractable, and, with it, the assumption is light-mediated O–O bond homolysis[14,15] has a sufficiently large energy to make propagation of oxygen-centered radical 7_{T1} towards product favorable, as opposed to recombination back to 7_{S1}. Alternatively, one could invoke the formation of a putative dimer with a tetraoxygen functionality acting as a bridging element.

34

Notwithstanding, the energy of this process was prohibitively high ($S8_{S1}$) at 79.2 kcal mol^{-1}, thus, ruling out this possibility. Irrespective, from 7_{T1}, transition state $TS5_{T1}$ emerges with an activation barrier of 6.40 kcal mol^{-1} and C···O bond forming distance of 1.91 Å. The resulting resonance-stabilized aryl radical 8_{T1} then undergoes C–C bond homolysis via transition state $TS6_{T1}$ having a C···C bond breaking distance of 2.17 Å and a computed activation barrier of 8.90 kcal mol^{-1} leading to triplet state intermediate 9_{T1}. Finally, relaxation to the ground state affords computed singlet state 3_{S1} corresponding to product **2**.

Synopses. In reflecting upon the above mechanistic possibilities, proposed pathway 4 stands out as the most viable option. Governing this preference is strain, photo-responsive functionality (QM moiety), and spin and/or charge delocalization within *p*-QM (**1**). Nonetheless, the insights from this model system, arguably, provide a compelling case of nonmetal-mediated oxygen atom insertion benefiting from abundant molecular oxygen as the terminal oxidant and light!
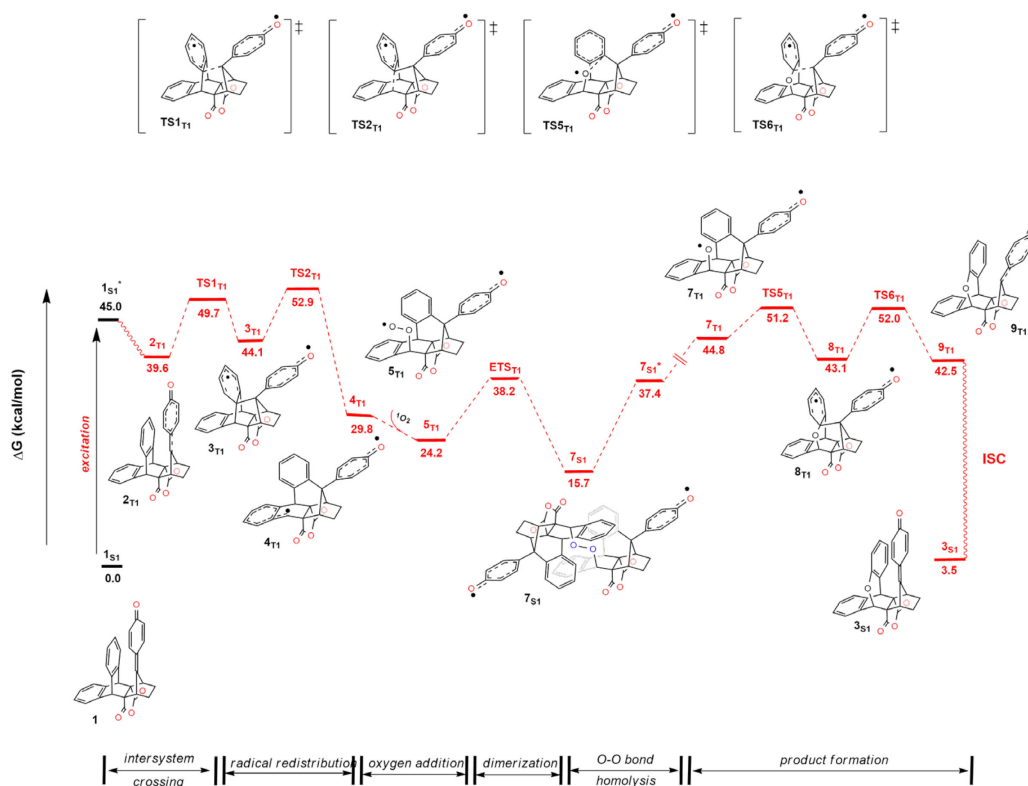
Figure 5.7. *Free energy profile for oxygen atom insertion via pathway 4. This pathway involves dimer species 7$_{S1}$ as a pivotal intermediate deemed necessary to access the product.*

Further to this point, the experimental observations realized in our previous report[5c] are concordant with the computational findings associated with pathway 4, namely solvent and H_2O-related implications. Experimentally, nitrile solvents were found to be an integral component for reactivity, which was previously an open-ended question that we now attribute to charge stabilization and/or quinone carbonyl polarization triggering photolysis-driven bond breaking and sensitization—among other events. This plausible indirect involvement of solvent in the mechanism also sheds light on the questions raised relating to the observed absence of nitrile-derived byproducts. Lastly, the possibility of obtaining hydrated side products can be accounted for by either reaction of the peroxide group present in the dimer with H_2O or a possible change in the mechanism (ionic vs. radical) that would be influenced by a change in the chemical environment, i.e., H_2O-induced.

5.3 Conclusion

In this chapter, additional insights regarding the mechanism of oxygen atom insertion into an aromatic p-QM $C(sp^3)$–$C(sp^2)$ bond of **1** were provided. Employing DFT calculations, a feasible pathway, among others investigated, was uncovered that hinged upon the formation of a key dimeric intermediate. Further, this pathway revealed a mechanistic scenario that supported the absence of nitrile-derived byproducts, while providing viable reasoning for the formation of hydrated side products in the presence of H_2O, thus, supporting empirical findings. Salient to this reactivity were the roles of earth abundant molecular oxygen as an oxidant and light as a driving force. As this type of reactivity is still in its infancy, it is projected that the results of this study will serve as an instructive conceptual resource, for emerging studies exploring nonmetal-based oxygen atom insertion processes.

5.4 References

1. Hamdane, D.; Zhang, H.; Hollenberg, P. *Photosynth Res.* **2008**, *98*, 657–666.

2. (a) Baeyer, A.; Villiger, V. *Ber. Dtsch. Chem. Ges*. **1900**, *33*, 858–864. (b) Baeyer, A.; Villiger, V. *Ber. Dtsch. Chem. Ges.* **1899**, *32*, 3625–3633.

3. ten Brink, G.-J.; Arends, I. W. C. E.; Sheldon, R. A. *Chem Rev.* **2004**, *104*, 4105–4124.

4. (a) Frahm, M.; von Drathen, T.; Gronbach, L. M.; Voss, A.; Lorenz, F.; Bresien, J.; Villinger, A.; Hoffmann, F.; Brasholz, M. *Angew. Chem. Int. Ed.* **2020**, *59*, 12450-12454 (b) Klaper, M.; Linker, T. *J. Am. Chem. Soc.* **2015**, *137*, 13744–13747. (c) Lucky, S. S.; Soo, K. C.; Zhang, Y *Chem. Rev.* **2015**, *115*, 1990–2042 (d) Wencel-Delord, J.; Dröge, T.; Liu, F.; Glorius, F. *Chem. Soc. Rev.* **2011**, *40*, 4740–4761. (e) Wendlandt, A. E.; Suess, A. M.; Stahl, S. S. *Angew. Chem. Int. Ed.* **2011**, *50*, 11062–11087. (f) Montagnon, T.; Noutsias, D.; Alexopoulou, I.; Tofi, M.; Vassilikogiannakis, G. *Org. Biomol. Chem.* **2011**. *9*, 2031–2039. (g) Montagnon, T.; Tofi, M.; Vassilikogiannakis, G. *Acc. Chem. Res.* **2008**, *41*, 1001–1011. (h) Chin, K. K.; Trevithick-Sutton, C. C.; McCallum, J.; Jockusch, S.; Turro, N. J.; Scaiano, J. C.; Foote, C. S.; Garcia-Garibay, M. A. *J. Am. Chem. Soc.* **2008**, *130*, 6912–6913. (i) Tromberg, B.; Kimel, S.; Orenstein, A.; Barker, S.; Hyatt, J.; Nelson, J.; Roberts, W.; Berns, M. *J. Photochem. Photobiol., B* **1990**, *5*, 121–126.

5. (a) Kazim, M.; Siegler, M. A.; Lectka, T. *Org. Lett.* **2019**, *21*, 2326–2329. (b) Kazim, M.; Siegler, M. A.; Lectka, T. A *J. Org. Chem.* **2019**, *84*, 8284–8288. (c) Kazim, M.; Foy, H.; Siegler, M. A.; Dudding, T.; Lectka, T. *J. Org. Chem.* **2019**, *84*, 14349–14353.

6. Kurosaki, R.; Hayashi, H.; Suzuki, M.; Jiang, J.; Hatanaka, M.; Aratani, N.; Yamada, H. *Chem. Sci.* **2019**, *10*, 6785–6790.

7. Anslyn, E. V.; Dougherty, D. A. *Modern Physical Organic Chemistry*; University Science Books: Sausalito, 2006.

8. Frisch, M. J.; Trucks, G. W.; Schlegel, H. B.; Scuseria, G. E.; Robb, M. A.; Cheeseman, J. R.; Scalmani, G.; Barone, V.; Mennucci, B.; Petersson, G. A.; Nakatsuji, H.; Caricato, M.; Li, X.; Hratchian, H. P.; Izmaylov, A. F.; Bloino, J.; Zhang, G.; Sonnenberg, J. L.; Hada, M.; Ehara, M.; Toyota, K.; Fukuda, R.; Hasegawa, J.; Ishida, M.; Nakajima, T.; Honda, Y.; Kitao, O.; Nakai, H.; Vreven, T.; Montgomery, J. A., Jr.; Peralta, J. E.; Ogliaro, F.; Bearpark, M.; Heyd, J. J.; Brothers, E.; Kudin, K. N.; Staroverov, V. N.; Kobayashi, R.; Normand, J.; Raghavachari, K.; Rendell, A.; Burant, J. C.; Iyengar, S. S.; Tomasi, J.; Cossi, M.; Rega, N.; Millam, J. M.; Klene, M.; Knox, J.e.; Cross, J. B.; Bakken, V.; Adamo, C.; Jaramillo, J.; Gomperts, R.; Stratmann, R. E.; Yazyev, O.; Austin, A. J.; Cammi, A. R.; Pomelli, C.; Ochterski, J. W.; Martin, R. L.; Morokuma, K.; Zakrzewski, V. G.; Voth, G. A.; Salvador, P.; Dannenberg, J. J.; Dapprich, S.; Daniels, A. D.; Farkas, Ö.; Foresman, J. B.; Ortiz, J. V.; Cioslowski, J.; Fox, D. J. Gaussian 09, Revision E.01; Gaussian, Inc., Wallingford, CT, 2009.

9. Chai, J.-D.; Head-Gordon, M. *Phys. Chem. Chem. Phys.* **2008**, *10*, 6615–6620.

10. Dennington, R.; Keith, T.; Millam, J. GaussView, version 5; Semichem, Inc., Shawnee Mission, 2009.

11. Pedley, J. B.; Naylor, R. D.; Kirby, S. P. *Thermochemical Data of Organic Compounds*. 2nd ed.; Chapman and Hall: New York, 1986.

12. Batsanov, S. S. Van der Waals Radii of Elements. *Inorganic Materials.* **2001**, *37,* 871–885.

13. (a) Ge, J.; Lan, M.; Zhou, B.; Liu, W.; Guo, L.; Wang, H.; Jia, Q.; Niu, G.; Huang, X.; Zhou, H.; Meng, X.; Wang, P.; Lee, C.-S.; Zhang, W.; Han, X. *Nat. Commun.* **2014**, *5*, 4596–4604. (b) Dolmans, D. E.; Fukumura, D.; Jain, R. K. *Nat. Rev. Cancer* **2003**, *3*, 380–387.

14. Abel, B.; Assmann J.; Botschwina, P.; Buback, M.; Kling, M.; Oswald, R.; Schmatz, S.; Schroeder, J.; Witte, T. *J. Phys. Chem. A* **2003**, *107*, 5157–5167.

15. Yaremenko, I. A.; Vil', V. A.; Demchuk, D. V.; Terent'ev, A. O. *Beilstein J. Org. Chem.* **2016**, *12*, 1647–1748.

16. Becke, A. D. *J. Chem. Phys.* **1993**, *98*, 5648–5652.

17. Lee, C.; Yang, W.; Parr, R. G. *Phys. Rev. B* **1988**, *37*, 785–789.

18. González, C.; Schlegel, H. B. *J. Phys. Chem.* **1990**, *94*, 5523–5527.

19. Fukui, K. *Acc. Chem. Res.* **1981**, *14*, 363–368.

20. Cancès, E.; Mennucci, B.; Tomasi, J. *J. Chem. Phys.* **1997**, *107*, 3032–3041.

21. Grimme, S. *J. Comput. Chem.* **2006**, *27*, 1787–1799.

22. Legault, C. Y. CYLview, version 1.0b; Universite de Sherbrooke: Quebec, Canada, 2009, http://www.cylview.org.

23. *Schrödinger Release 2019–2*: *Jaguar*; Schrödinger, LLC: New York, 2019.

Chapter 6: Close Amide NH⋯F Hydrogen Bonding Interactions in 1,8-

Disubstituted Naphthalenes

6.1 Introduction

The interaction of C-F bonds, especially in proteins, with proximate functional groups is a topic of lively interest and discussion.[1-6] Their importance in dictating protein structure and function is not yet fully answered, including the dilemma of whether such interactions themselves are due to propinquity, attractive interactions, or a combination thereof. Over the past several years we have investigated close interactions between C-F bonds and common organic functional groups in relatively small molecules that are often dictated by forced proximity, along with some measure of attraction and repulsion.[7-13] The case of the amide NH⋯F interaction is presumably one of the more interesting, due to the ubiquity of amide residues in proteins. Nevertheless, a search of the Cambridge Crystallographic Database (CCD) indicates only a few substantial interactions; most are self-evidently weak and long range. The closest such interaction we found was approximately 1.93 Å.[14] We thought it would be illustrative and useful to investigate the closest range and thus strongest model interaction we could conceive in order to achieve a fuller understanding. In this note, we employ the 1,8-disubstituted naphthalene scaffold to investigate a series of amide NH⋯F interactions that are by spectroscopic measures more intense than those exhibited in the available crystal structure database. Historically, these so-called "proton sponge" derivatives have often been used to investigate the nature of close H-bonding interactions.[15-20] We imagined that a series of these molecules would once again serve as excellent models for the study of amide-NH⋯F interactions (Figure **6.1**).

effects of varying R on NH---F interaction
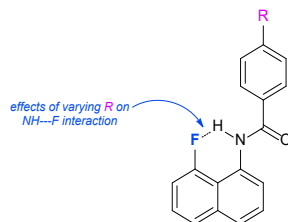
Figure 6.1. *The NH⋯F Interaction in N-(8-fluoronaphthalen-1-yl)benzamide derivatives*

6.2 Results and Discussion

Chemical intuition suggests that the *trans*-amide conformation of these *N*-(8-fluoronaphthalen-1-yl)benzamide derivatives would make the N-H proton particularly available to engage in hydrogen bonding to the neighboring "peri" fluorine atom. On the other hand, $\pi-\pi$ interactions in aromatic compounds[21-24] are well known to skew the rotameric preferences of aryl amides. To shed light on the relative stabilities of the rotamers - and thereby possible H-bonding interactions - we turned to DFT calculations. At ωB97XD/6-311+G**, we located the cis and trans rotamers for each derivative (Figure **6.2**). In trans structures **1-4**, the NH hydrogen resides at a position maximizing the NH$\cdots$F interaction, whereas it bends out of the plane of naphthalene ring in cis structures **1a-4a**, thus attenuating the interaction (Figure **6.2**). As it were, the desired rotamers were predicted to be more stable by at least 2.3 kcal/mol as we would ordinarily expect. Additionally, the amide NH$\cdots$F distances in the series **1-4** are predicted to lie in the range of 1.84–1.86 Å (gas phase), smaller than the shortest distance of 1.93 Å observed crystallographically.[14]
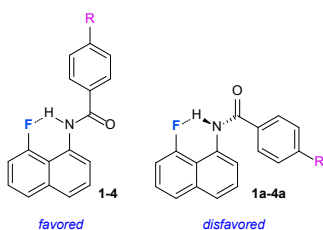
Figure 6.2. *Rotameric forms located by DFT calculations (ωB97XD/6-311+G**) with* **1-4** *favored over* **1a-4a** *by >2.7 kcal/mol.*

Curiously, replacing the fluorine with hydrogen attenuates the preference for the desired rotamer and no stability trend is observed when test molecules **5** were optimized at the same level of theory (Figure **6.3**). In fact, the NH proton bends out of the plane of the naphthalene ring in both optimized rotamers. Similarly, no noticeable trend was observed when rotamers of 7-fluoro-1-aminonaphthalene derivatives were optimized (**6**, Figure **6.3**). These calculations suggested to us that the relative stability of desired rotamers could be attributed in part to favorable NH$\cdots$F interactions. Therefore, having a fluorine atom at that position may prove essential to the investigation as it locks the structure in the desired orientation.
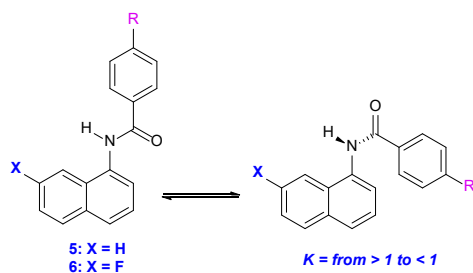
Figure 6.3. Rotamers of *5* and *6* optimized for rotameric preferences with DFT calculations at ωB97XD/6-311+G**; R = NMe$_2$; OMe; H; NO$_2$.

After DFT calculations pointed us in the right direction, we synthesized the desired molecules from commercially available 1,8-diaminonaphthalene **8**. Treatment of **8** with isoamyl nitrite followed by HF-pyridine resulted in the formation of 8-fluoro-1-aminonaphthalene **10**,[25] which was then acetylated with a series of substituted benzoyl chlorides to afford N-(8-fluoronahphthalen-1-yl)benzamide derivatives in 75-85% yields (Scheme **6.1**). The dimethylamino analogue **4** was synthesized by reduction/alkylation of p-NO$_2$ derivative **3** (Scheme **6.1**).
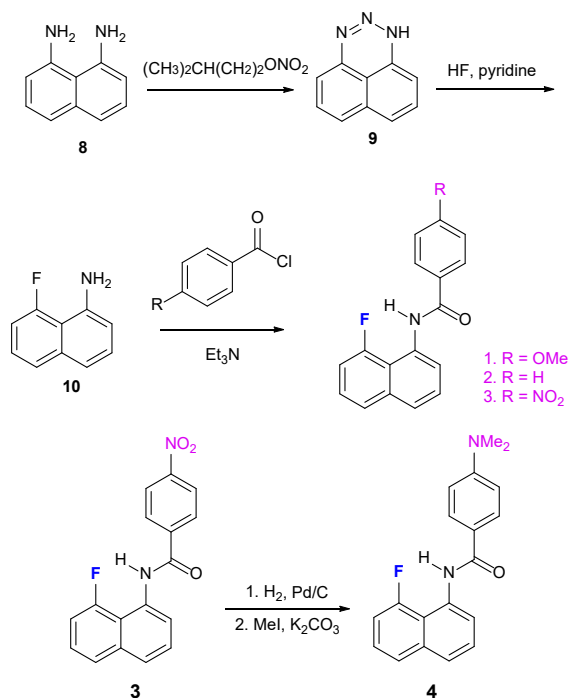
Scheme 6.1. Synthesis of N-(8-fluoronahphthalen-1-yl) benzamide derivatives.

The two rotamers can easily be distinguished based on the NH···F spin-spin coupling constants predicted by DFT calculations (B3LYP/6-311++G**). In *trans*-amide conformations, the calculated coupling constants lie between 24-27 Hz, whereas for the undesired rotamers as well as rotamers of **5** and **6** those numbers drop to 0-2 Hz. Experimentally, the ^{1}H NMR spectra of all derivatives show NH protons as apparent doublets (J_{H-F} = 20-21 Hz). On the other hand, the ^{19}F NMR spectra reveal complex multiplets. Both ^{1}H and ^{19}F NMR spectra indicate that the products of Scheme **1** are locked exclusively in the desired *trans* orientation. The ^{19}F NMR of all the derivatives also reveal consistent 16 Hz coupling constants corresponding to the interaction of the F nucleus with the ortho proton on the naphthalene ring system[16] (calcd 16.4 Hz, Figure **6.4**). Additionally, the coupling constants for the series are predicted to show a slight increase as the substituent on the benzene ring becomes more electron withdrawing (from 24.7 Hz for p-NMe$_2$ to 27 Hz for p-NO$_2$). However, this modest trend is not clearly discernable in the actual ^{19}F NMR data primarily due to the complex nature of the multiplets.
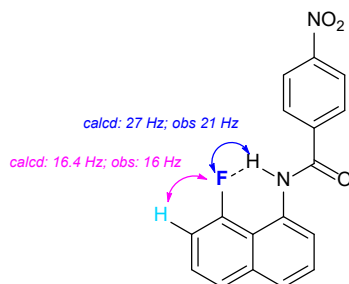
Figure 6.4. Major coupling constants observed experimentally and predicted by B3LYP/6-311++G** (compound **3**).

We then conducted an IR analysis of the NH···F interactions. It is generally accepted that the increasing strength of a classical hydrogen bond results in lengthening of the donor-H bond and an attendant shortening of the acceptor-H distance, inducing a red shift in the IR-stretching frequency.[26-30] An initial DFT analysis (ωB97XD/6-311+G**) of the synthesized molecules predicts a similar trend for NH stretches in the IR as the nature of substituent becomes more electron withdrawing, a possible indication of increasing hydrogen bond strength (Table **6.1**).

NH stretch cm^{-1}	R = NMe$_2$	OMe	H	NO$_2$
predicted	3517	3516	3503	3501
experimental	3486	3482	3477	3471

Table 6.1. Calculated (scaled) and experimentally observed NH stretching frequencies in 1 through 4.

The NH stretch in the experimentally observed IR spectra of the derivatives shows a continuous high energy shift as the aromatic ring becomes more electron deficient. The NH stretch of p-NO$_2$ derivative appears at 3470.5 cm^{-1}, which is ca. 16 cm^{-1} red shifted compared to the same stretch in the p-NMe$_2$ derivative, thus implying a significantly stronger H bond in the former case (Table **6.1** and Figure **6.5**). Although substituent effects have a relatively smaller effect on high energy shifts in the NH stretching frequency of benzamides, this fact does not necessarily imply a weak substituent effect on the hydrogen bond strength itself since the high energy shift in IR is considered only a semi-quantitative measure.[31]
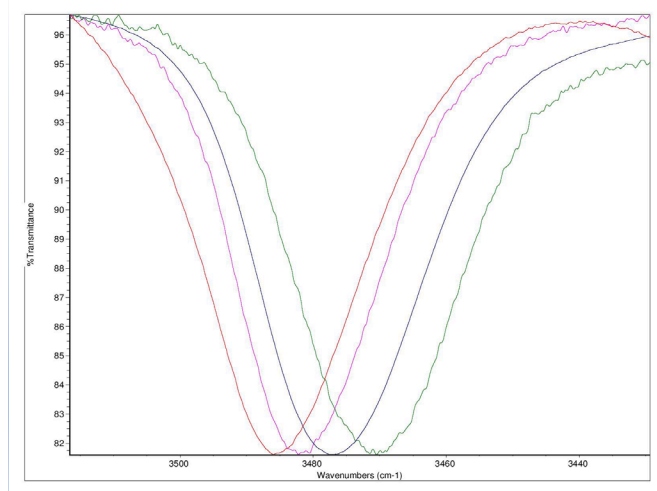
Figure 6.5. Experimentally observed NH stretches in IR spectra; red (p-NMe$_2$); purple (p-OMe); blue (p-H); green (p-NO$_2$).

X-ray crystallographic analysis gives additional insight into the influence of fluorine substitution on crystal packing. We recently reported the crystal structure of a substituted trityl fluoride that is significantly different than the corresponding trityl hydride, confirming the inability of fluorine to act as an "isostere" for hydrogen when it comes to directionality/ordering.[32] Single crystal X-ray analysis of the p-NO$_2$ derivative

3 reveals an interesting feature; the naphthalene rings are aligned face to face in a $\pi-\pi$ interaction (Figure **6.6**), which is significantly different than the crystal structure of *N*-(naphthalen-1-yl)benzamide, wherein the phenyl ring engages in T-shaped $\pi-\pi$ interactions with the naphthalene ring system.[33] This motif results in the formation of naphthalene-based sheets held by intermolecular hydrogen bonding between the amide N-H and a neighboring molecule's carbonyl oxygen at 2.12 Å. Moreover, the NH···F and N-H distances of 2.22 Å and 0.87 Å are observed in the crystal structure of p-NO$_2$ benzamide derivative (Figure **6.6**).
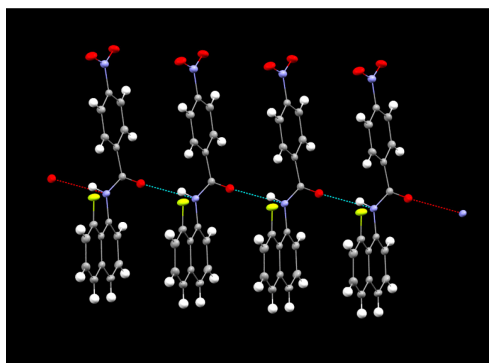
*Figure 6.6. X-ray crystal structure of p-NO$_2$ benzamide derivative (**3**) with extended hydrogen bonding network forming sheets of naphthalene rings.*

Finally, we imagined that an even larger high energy IR shift could be observed if the substituent is more electron withdrawing than p-NO$_2$Ph. A DFT analysis predicted that replacing the benzamide derivatives with trifluoroacetamide would show a significant red shift of an additional 39 cm^{-1} in NH stretching frequency compared to p-NO$_2$Ph derivative. In fact, when 8-fluoro-1-aminonaphthalene is acetylated with trifluoroacetic anhydride (Scheme **6.2**, 86%), the NH stretch of the product appears at 3443 cm^{-1}, red shifted by 28 cm^{-1} compared to the p-NO$_2$ derivative (Figure **6.7**). Additionally, its ^{19}F NMR spectrum shows a multiplet corresponding to aromatic fluorine with a spin-spin coupling constant of 19.1 Hz to the proximate N-H, even larger than that observed in **3**.
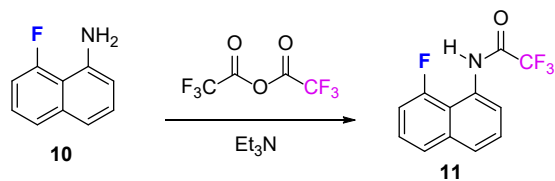
Scheme 6.2. *Synthesis of the trifluoroacetamide derivative **11**.*
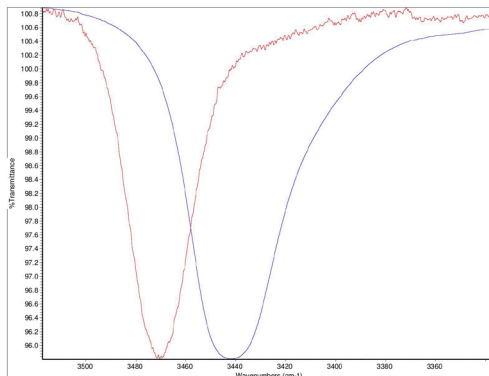
Figure 6.7. *Experimentally observed NH stretches in IR spectra; red (p-NO$_2$Ph) peak at 3470.5 cm^{-1}; blue (CF$_3$) peak at 3442.9 cm^{-1}.*

Single crystal X-ray analysis of the trifluoroacetamide derivative **11** also reveals an interesting structure. Similar to the benzamide derivatives, the crystal is characterized by sheets and bifurcated C-F···HN bonding with an amide carbonyl oxygen and fluorine on position 8 of the naphthalene ring (NH···F, 2.12 Å), (NH···O, 2.19 Å), (N-H···F$_3$C, 2.25 Å). Another interesting feature of trifluorobenzamide derivative's crystal structure is the close F···F distance (2.98 Å) between the neighboring molecules' CF$_3$ groups (Figure **6.8**).
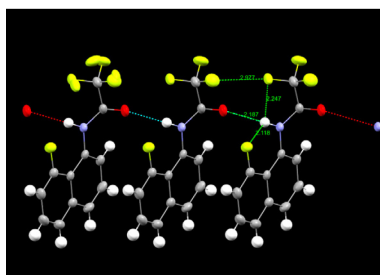
Figure 6.8. *X-ray crystal structure of trifluoroacetamide derivative **11** depicting an extended hydrogen bonding network forming sheets of naphthalene rings.*

The X-ray crystal structures of **3** and **11**, however, depict amide NH···F distances of 2.22 Å and 2.12 Å respectively, which are greater than the shortest NH···F distance found in the CCD and our predicted gas phase distances. This increased distance in the crystal structures can be attributed to intermolecular hydrogen bonding with neighboring molecule's carbonyl oxygen. In dilute solutions, however, we conclude that the intramolecular NH···F interaction dominates and the distance could be approximated to, or even smaller, than 1.93 Å. We optimized a few of the structures with the shortest NH···F distances reported in the CCD[34-37] at ωB97XD/6-311+G** and calculated spin-spin coupling constants for the NH···F interactions therein at B3LYP/6-311++G**. DFT calculations predict an inverse correlation of the NH···F coupling constants and distances between the interacting nuclei (Figure **6.9**). The largest amide NH···F coupling constant reported in the literature is 17.1 Hz.[35] This is smaller than those observed in our molecules which are, both predicted and experimentally, more than 20 Hz, indicating the *possibility* of an amide NH···F distance shorter than those observed so far. The trend in Figure **6.9** predicts NH···F distances in the series of our benzamide derivatives to be approximately 1.90 Å in dilute solutions, in line with DFT geometry calculations. However, when it comes to crystal packing, the NH proton skews out of the plane of naphthalene ring as a result of competitive intermolecular NH···OC hydrogen bonding.
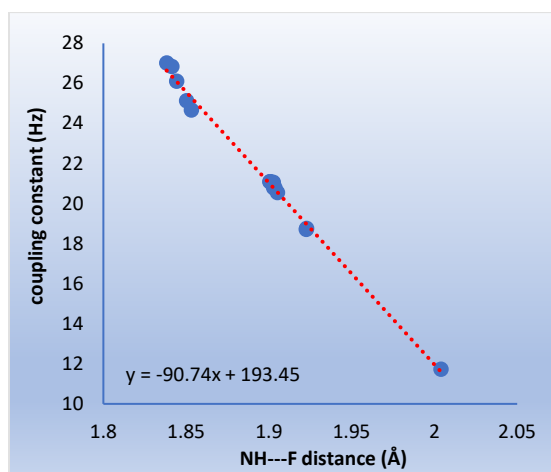
*Figure 6.9. Correlation between calculated NH···F distances and corresponding coupling constants calculated at B3LYP/6-311++G** using molecules 1-4 and 11-20.*

6.3 Conclusion

In this chapter, we have synthesized a series of N-(8-fluoronaphthalen-1-yl)benzamide derivatives and established a correlation between the strength of NH···F hydrogen bonding interaction and substituents on the benzamide ring. Both ^{1}H and ^{19}F NMR spectra indicate the exclusive formation of the desired geometry, attributed to the favorable hydrogen bonding interactions, most notably through strong spin-spin coupling of H and F. Moreover, IR analysis of the series predicts a direct correlation between the electron withdrawing nature of substituent and the hydrogen bond strength. X-ray crystallographic analysis reveals the formation of sheets characterized by face-to-face $\pi-\pi$ interactions between the naphthalene rings. We hope that these results provide additional insights into the increasingly important role of fluorine in hydrogen bonding interactions.

6.4 References

1. Vishnumurthy, K.; Row, T. N. G.; Venkatesan; K. Photoch. *PhotoBio. Sci.* **2002**, *6*, 427-430.

2. Kawahara, S.; Tsuzuki, S.; Uchimaru, T. *J. Phys. Chem. A* **2004**, *108*, 6744-6749.

3. Jackel, C.; Koksch, B. *Eur. J. Org. Chem.* **2005**, *21*, 4482-4503.

4. Riley, K. E.; Merz, K. M. *J. Phys. Chem. B* **2005**, *109*, 17752-17756.

5. Chopra, D.; Nagarajan, K.; Row, T. N. G. *J. Mol. Struct.* **2008**, *888*, 70-83.

6. Zhou, P.; Zou, J.; Tian, F.; Shang, Z. *J. Chem. Inf. Model.* **2009**, *49*, 2344-2355.

7. Struble, M. D.; Guan, L.; Siegler, M. A.; Lectka, T. *J. Org. Chem.* **2016**, *81*, 8087-8090.

8. Holl, M. G.; Struble, M. D.; Singal, P.; Siegler, M. A.; Lectka, T. *Angew. Chem. Int. Ed.* **2016**, *55*, 8266-8269.

9. Struble, M. D.; Kelly, C.; Siegler, M. A.; Lectka, T. *Angew. Chem. Int. Ed.* **2014**, *53*, 8924-8928.

10. Holl, M. G.; Pitts, C. R.; Lectka, T. *Acc. Chem. Res.* **2020**, *53*, 265-275.

11. Pitts, C. R.; Siegler, M. A.; Lectka, T. *J. Org. Chem.* **2017**, *82*, 3996-4000.

12. Holl, M. G.; Struble, M. D.; Siegler, M. A.; Lectka, T. *J. Fluorine Chem.* **2016**, *188*, 126-130.

13. Holl, M. G.; Pitts, C. R.; Lectka, T. *Angew. Chem. Int. Ed.* **2018**, *57*, 2758-2766.

14. Zhu, W.; Yang, W.; Zhou, W.; Liu, H.; Wei, S.; Fan, J. A. *J. Mol. Struct.* **2011**, *1004*, 74-81.

15. Cox, C.; Wack, H.; Lectka, T. *Angew. Chem. Int. Ed.* **1999**, *38*, 798-800.

16. Scerba, M. T.; Leavitt, C. M.; Diener, M. E.; DeBlase, A. F.; Guasco, T. L.; Siegler, M. A.; Bair, N.; Johnson, M. A.; Lectka, T. *J. Org. Chem.* **2011**, *76*, 7975-7984.

17. Alder, R. W.; Bowmann, P. S.; Steele, W. R. S.; Winterman, D. R. *Chem. Commun.* **1968**, *13*, 723-724.

18. Staab, H. A.; Saupe, T. *Angew. Chem. Int. Ed.* **1988**, *27*, 865-879.

19. Alder, R. W. *Chem. Rev.* **1989**, *89*, 1215-1223.

20. Hibbert, F.; Emsley, J. *Adv. Phys. Org. Chem.* **1990**, *26*, 255-379.

21. Hunter, C. A.; Sanders, J. K. M. *J. Am. Chem. Soc.* **1990**, *112*, 5525-5534.

22. Hunter, C. A.; Singh, J.; Thornton, J. M. *J. Mol. Biol.* **1991**, *218*, 837-846.

23. Martinez, C. R.; Iverson, B. L. *Chem. Sci.* **2012**, *3*, 2191-2201.

24. Sony, S. M. M.; Ponnuswamy, M. N. *Cryst. Growth Des.* **2006**, *6*, 736-742.

25. Zhu, Z.; Colbry, N. L.; Lovdahl, M.; Mennen, K. E.; Acciacca, A.; Beylin, V. G.; Clark, J. D.; Belmont, D. T. *Org. Prep. Process Res. Dev.* **2007**, *11*, 907–909.

26. Arunan, E.; Desiraju, G. R.; Klein, R. A.; Sadlej, J.; Scheiner, S.; Alkorta, I.; Clary, D. C.; Crabtree, R. H.; Dannenberg, J. J.; Hobza, P.; Kjaergaard, H. G.; Legon, A. C.; Mennucci, B.; Nesbitt, D. J. *Pure Appl. Chem.* **2011**, *83*, 1637-1641.

27. Joseph, J.; Jemmis, E. D. *J. Am. Chem. Soc.* **2007**, *129*, 4620-4632.

28. Duarte, L. J.; Silva, A. F.; Richter, W. E.; Bruns, R. E. *J. Phys. Chem. A* **2019**, *123*, 6482-6490.

29. Mao, Y.; Gordon, M. H. *J. Phys. Chem. Lett.* **2019**, *10*, 3899-3905.

30. Wang, C.; Mo, Y. *Inorg. Chem.* **2019**, *58*, 8577-8586.

31. Rosenberg, M.; Loewenschuss, A.; Marcus, Y. *Phys. Chem. Chem. Phys.* **2000**, *2*, 2699-2702.

32. York, G. D.; Siegler, M. A.; Patel, D. D.; Lectka, T. *J. Fluor. Chem.* **2019**, *228*, 109377.

33. Zhu, R.; Ren, Y.; Li, W. *Acta Cryst.* **2011**, E**67**, o3204. DOI: 10.1107/S1600536811045946.

34. Zhao, X.; Wang, X. Z.; Jiang, X. K.; Chen, Y. Q.; Li, Z. T.; Chen, G. J. *J. Am. Chem. Soc.* **2003**, *125*, 15128-15139.

35. Li, C.; Ren, S. F.; Hou, J. L.; Yi, H. P.; Zhu, S. Z.; Jiang, X. K.; Li, Z. T. *Angew. Chem. Int. Ed.* **2005**, *44*, 5725-5729.

36. Zhu, K. Y.; Wu, J.; Li, C.; Zhu, J.; Hou, J. L.; Li, C. Z.; Jiang, X. K.; Li, Z. T. *Crys. Growth Des.* **2007**, *7*, 1490-1496.

37. Bhandary, S.; Gonde, S.; Chopra, D. *Cryst. Growth Des.* **2019**, *19*, 1072-1085.

Chapter 7: Switching a HO···π Interaction to a Nonconventional OH···π Hydrogen Bond: A Completed Crystallographic Puzzle

7.1 Introduction

Nonconventional hydrogen bonds between X-H, where X is an electronegative atom, and the π cloud of an aromatic ring (Figure **7.1**) have significant importance in chemistry and structural biology.[1–10] For example, Steiner and Koellner screened a list of 529 high resolution protein crystal structures and noted that one in almost 11 protein residues with aromatic side chains act as π-hydrogen bond acceptors.[11] Additionally, several examples of small molecules depicting such interactions are reported in the literature.[12–20] Nonetheless, many aspects of these intriguing non-covalently bonded interactions remain relatively unexplored. We thought it important to construct a rigid molecular system exhibiting close, yet tunable OH···π HB properties in order to establish a more detailed understanding of this timely problem. In this regard, we report the syntheses of a few substituted analogues based on the fused 9,10-dihydroanthracene-bicycloheptane scaffold (e.g. compound **1**) that facilitate a more thorough investigation of nonconventional OH···π hydrogen bonds (Figure **7.2**). Most importantly, these analogues permitted us to characterize *three distinct geometric stages of interaction:* the exclusive HO··· π, the partitioned HO··· π/OH···π and the exclusive OH···π.

Figure 7.1. *Generic HO···π and OH···π rotameric forms leading to through space arene activation and a nonconventional H-bonding interaction.*
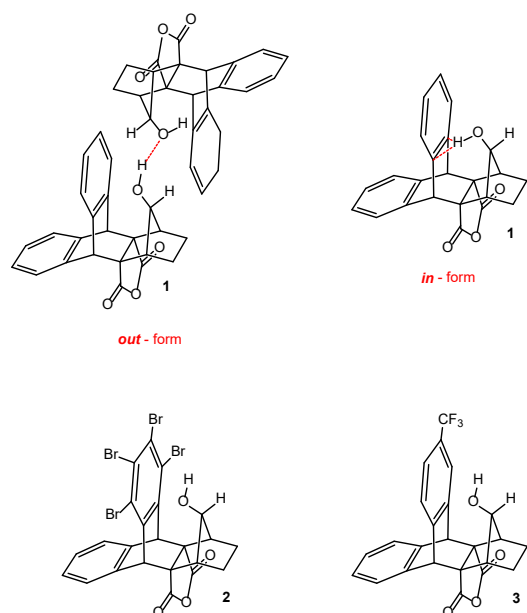
Figure 7.2. Structures of compounds 1 (the in-form engages in nonconventional HB while the out-form engages in a conventional HB), 2 and 3.

Our previous analysis of compound **1** focused on the fortuitous HO···π interaction that resulted in a strong through-space activation of the adjacent *"top"* ring towards electrophilic aromatic substitution (EAS) reactions.[21] However, crystallographic analysis of compound **1** revealed that the oxygen-bound hydrogen atom is partitioned between two orientations. In the *in*-form, it engages in a nonconventional OH···π hydrogen bond with the top ring's π system (OH···C_{aryl} distance = 2.03 Å) whereas in the *out*-form, it engages in a conventional OH···O hydrogen bond with an oxygen atom of a neighboring molecule (OH···O distance = 1.94 Å) (Figure **7.2**).[21] Furthermore, when the *top* ring was functionalized with deactivating groups, the oxygen-bound hydrogen could no longer benefit from a strong OH···π hydrogen bond. For example, in the crystal structure of tetrabrominated analogue **2**, the oxygen-bound hydrogen was exclusively locked in the *out*-form (Figure **2**).[21]

It is important to note that the OH···π distance observed in the *in*-form of **1** is very close to the shortest such distance established crystallographically (1.98 Å).[22] Therefore, this observed nonconventional hydrogen bond could be classified as one of the stronger OH···π interactions. However, none of the

molecules reported in our previous article exhibited the oxygen bound hydrogen to be locked *exclusively* in the *in*-form to allow a more extensive investigation of this phenomenon.

It has been suggested that stronger hydrogen bonds have more covalent character, whereas weaker hydrogen bonds are dominated by electrostatic interactions.[23] Boxer and co-workers established a direct correlation between the electronic nature of the aromatic ring and the strength of various π-hydrogen bonds in solution employing substituted benzene complexes.[14,24] Their results indicate that the electrostatic properties of the hydrogen bond acceptor, namely the aromatic ring, dominate these interactions in solution.[24] We imagined that an electron rich analogue of compound **1** might benefit from a significantly stronger OH$\cdots\pi$ hydrogen bond and thus lock the system in the *in*-form, thus providing the missing "third stage."

7.2 Results and Discussion

To test this hypothesis, we turned to DFT calculations (ωB97XD/6-311+G**). The *in*-form is predicted to be favored by 6.7 kcal/mol when the *top* ring is substituted by an amino group. Similarly, in molecule **1** (R = H), the *in*-form is predicted to be 5.8 kcal/mol more stable than the *out*-form (gas phase), in part due to favorable OH$\cdots\pi$ interactions. However, in the *top*-CF_3 analogue (compound **3**, Figure **7.2**), the *in* and *out* forms are predicted to be almost isoenergetic (Figure **7.3**). This apparent drop in selectivity can be attributed to less propitious OH$\cdots\pi$ interactions in an electron-poor system. On the other hand, we imagined that a protonated amino analogue might switch the rotameric preference as the substituent becomes an electron withdrawing group ($-NH_3^+$ vs. $-NH_2$). When optimized (ωB97XD/6-311+G**), the *out*-form of top NH_3^+ analogue is predicted to be more stable by roughly 10 kcal/mol compared to the respective *in*-form, indicating a protonation-driven switch from a favorable OH$\cdots\pi$ hydrogen bond in the NH_2 derivative to a complete HO$\cdots\pi$ interaction in the NH_3^+ version (Figure **7.3**).
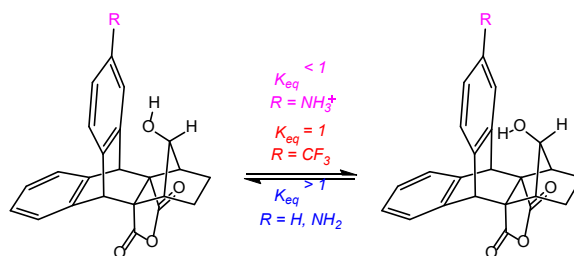
Figure 7.3. *Isodesmic relation comparing the energies of in and out rotamers (DFT – ωB97XD/6-311+G**); R = NH_3^+, CF_3, H, NH_2.*

After DFT calculations pointed us in the right direction, we embarked upon the synthesis of the *top*-NH_2 analogue **5**. Subjecting **1** to nitrating conditions results in exclusive formation of **4** (Scheme **7.1**). Formation of the nitrate ester is evident from the ^{1}H NMR wherein the hydroxyl proton disappears in the product and the proton on C1 appears deshielded at 4.72 ppm in **4** (-0.22 ppm and 3.85 ppm respectively in **1**). Hydrogenation at 3 atm. simultaneously clove the nitrate ester and reduced the aromatic nitro group to generate the target molecule **5** (Scheme **7.1**).
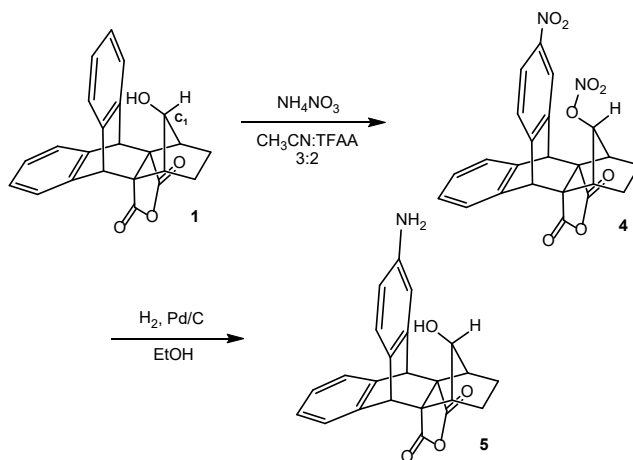
Scheme 7.1. *Synthesis of compound **5**.*

7.3 IR Spectroscopic Analysis

We envisioned that IR spectroscopy would be a critical tool in the investigation of this system. Generally speaking, increasing the strength of a classical hydrogen bond results in lengthening of the donor-H bond and a concomitant shortening of the acceptor⋯H distance, thereby inducing a lower energy shift in the

respective IR-stretching frequency.[25-29,32] Compounds **1**, **3** (top CF$_3$ analogue)[30] and **5** were considered;

initial DFT analysis at ωB97XD/6-311+G** predicts increasing red shifts of the OH stretching frequencies of

the *in*-forms as the adjacent *top* ring becomes more electron rich (Table **7.1**). As expected, the *out*-forms

show no significant trend in these candidates, as their oxygen bound hydrogen atoms do not engage in

OH$\cdots\pi$ interactions. Experimentally, the IR spectrum of **5** locates an OH stretch at 3553 cm^{-1} that is red

shifted by roughly 50 cm^{-1} and 25 cm^{-1} compared to the same stretch in **3** and **1**.[21] This observation is

congruent with a stronger hydrogen bond in **5** (Table **7.1** and Figure **7.4**). The IR spectrum of **5** also locates

the N-H stretch at 3395 cm^{-1} (consistent with DFT calculations which predict the NH stretch to appear

roughly 160 cm^{-1} less than the OH stretch) (Figure **7.5**, red spectrum).

OH stretch cm^{-1}	R = CF$_3$	H	NH$_2$
predicted (in forms)	3762	3745	3707
experimental	3606	3578	3553

Table 7.1. *Calculated (scaled) and experimentally observed OH stretching frequencies in* **1**, **3** *and* **5***.*

  Interestingly, calculations indicate that the OH stretches of the *in*-forms are affected differently in these

molecules depending on the nature of substituent on the adjacent *top* ring. For example, OH stretches of

the *in*-forms are predicted to be "*blue*" shifted by 34 cm^{-1} in **3**, almost identical (no shift) in **1** and "*red*"

shifted by 18 cm^{-1} in **5** compared to OH stretches in their corresponding *out*-forms. These calculations

suggest that electron-deficient rings have a propensity to induce blue shifts whereas electron rich rings can

induce red shifts in OH stretching frequencies.
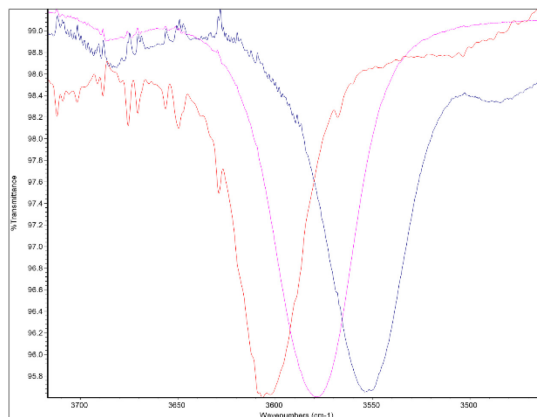
Figure 7.4. *The OH region of IR spectra for compounds **1**, **3** and **5**. Red (R = CF$_3$); purple (R = H); blue (R = NH$_2$).*

   When compound **5** was subjected to protonation with one equiv. of 1M HCl in CH$_2$Cl$_2$, we observed a large

blue shift in the OH stretching region. The OH stretching frequency in **5** (3553 cm^{-1}) shifts to 3685 cm^{-1},

indicating a significantly weaker (probably absent) OH···π hydrogen bonding interaction in the protonated

form (Figure **7.5**). The IR spectrum of **5**–H$^+$ also locates the NH stretch at 3600 cm^{-1} (predicted 3707 cm^{-1}

and 3605 cm^{-1} for OH and NH stretches by DFT calculations [IEFPCM-DCM solvation]). In addition, none of

the peaks in the IR spectrum of **5**–H$^+$ show widths characteristic of excess protic acid. Finally, as seen for

compound **3**, DFT calculations also predict that the OH stretch in the *in* form of **5**–H$^+$ is blue shifted by

roughly 14 cm^{-1} compared to the same stretch in the corresponding *out* rotamer.
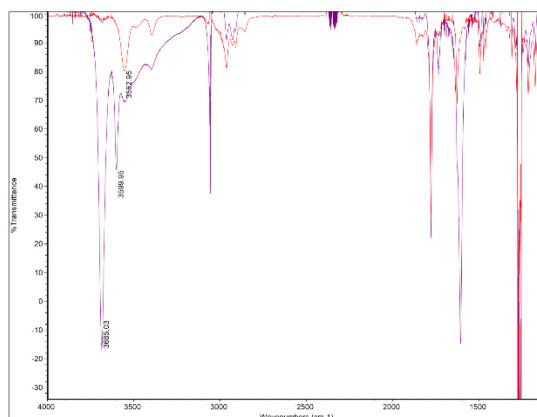
Figure 7.5. *Comparison of IR spectra for compounds **5** and **5**-H$^+$; red (R = NH$_2$); purple (R = NH$_3$$^+$).*

7.4 X-Ray Crystallographic Analysis

Single crystal X-ray analysis of compound **5** reveals an interesting hydrogen bonding network. As hypothesized, the OH group is found *exclusively* in the *in*-form, thus engaging in a nonconventional hydrogen bond with the adjacent *top*-aromatic ring and locating the alcoholic proton at 2.108 Å and 2.237 Å from carbons para and meta to the amino group (predicted 2.074 Å and 2.213 Å), thus classifying it among the stronger such interactions observed crystallographically. On the other hand, the lone pairs of the OH group readily hydrogen bond to an NH_2 group of another molecule (NH···O distance 2.03 Å; N-H distance 0.88 Å). As a result, an extended hydrogen bond network comprised of two conventional (NH···O) and two nonconventional (OH···π) hydrogen bonds anchors compound **5** in the crystal (Figure **7.6**). Additionally, the carbonyl oxygen on the anhydride ring also engages in a longer-range conventional HB interaction with a neighboring molecule's NH_2 hydrogens (NH···O distance 2.245 Å).
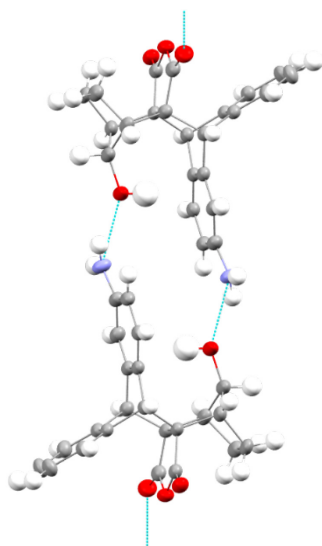
Figure 7.6. *X-ray crystal structure of compound **5** depicting dimerization as a consequence of an extended network of two conventional and two nonconventional hydrogen bonds.*
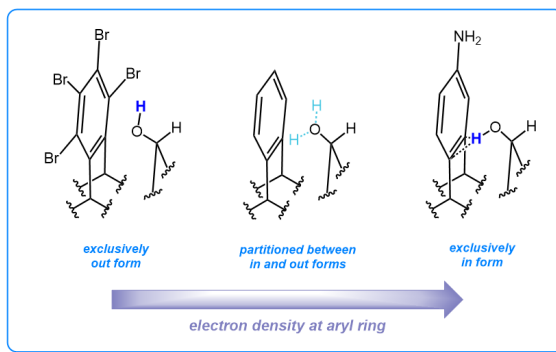
Figure 7.7. *Abbreviated structures of compounds 2, 1 and 5 in the solid state showing a stepwise switch from HO⋯π to*

a nonconventional OH⋯π hydrogen bond.

Most importantly, the X-ray crystal structure of **5** provided the final missing piece of the crystallographic puzzle. We previously observed that in systems with electron deficient aromatic rings, the OH group was locked in the *out*-form (compound **2**) whereas in a non-substituted π-system (compound **1**), it was partitioned between the *in* and *out* forms in the crystal structure.[21] We observe an electron rich π-system (compound **5**) locking the hydrogen of the OH group in the *in*-orientation, thereby providing a continuous series of crystallographic "snapshots" of a three-stage, tuneable system (Figure **7.7**).

7.4 Molecular Orbital Interactions

We imagined that a favorable interaction between the aryl-centered π system and OH σ* MOs can lead to a significant OH⋯π hydrogen bond. On the other hand, preferential interaction of oxygen-centered non-bonding *"n_o"* and aryl centered π* MOs can skew the system towards the rotameric HO⋯π form. Therefore, we analyzed the relevant MOs in fragments of compounds **1**, **3**, **5** and [**5**–H]$^+$ (ωB97XD/6-311+G**). Consistent with chemical intuition, DFT predicts an incremental change in the energies of aromatic ring-centered π and π* orbitals as the substituents become more electron-donating (Figure **7.8**).
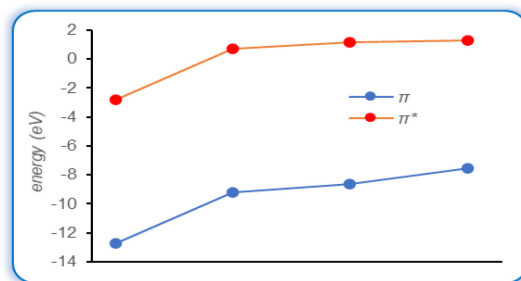
Figure 7.8. *Energies of aromatic centered HOMO (π) and LUMO (π*); left to right: R = NH_3^+, CF_3, H, NH_2.*
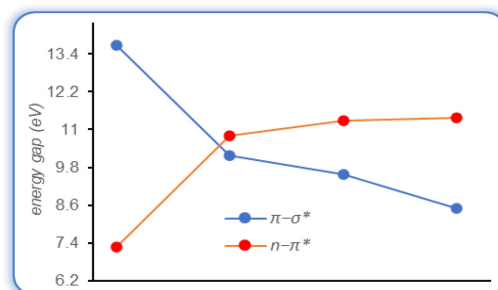
Figure 7.9. *Energy gaps for $n_o - \pi$* and $\pi - \sigma$* interactions; left to right R = NH_3^+, CF_3, H, NH_2.*

Additionally, energies of the oxygen centered n_o and OH σ* MOs were obtained after optimizing both orientations of the oxygen bound hydrogen. Interestingly, analysis of charge transfer from an oxygen-based n_o to π* and aromatic π to OH σ* reveals that increasing electron density on the aromatic ring lowers the energy gap for π–σ* overlap. This in turn makes OH$\cdots\pi$ interactions more favorable, whereas it simultaneously increases the n_o–π* overlap gap (Figure **7.9**). For example, in compound **5**, an aromatic π to OH σ* interaction is preferred (energy gap = 8.5 eV vs 11.4 eV for n_o to π*) which locks the system exclusively in the *in*-form. On the contrary, electron transfer from n_o to the aromatic π* is energetically preferred in **5**-H$^+$ (energy gap = 7.3 eV vs. 13.7 eV for aromatic π to OH σ*), thereby favoring the *out*-form (Figure **7.9** and Figure **7.10**).
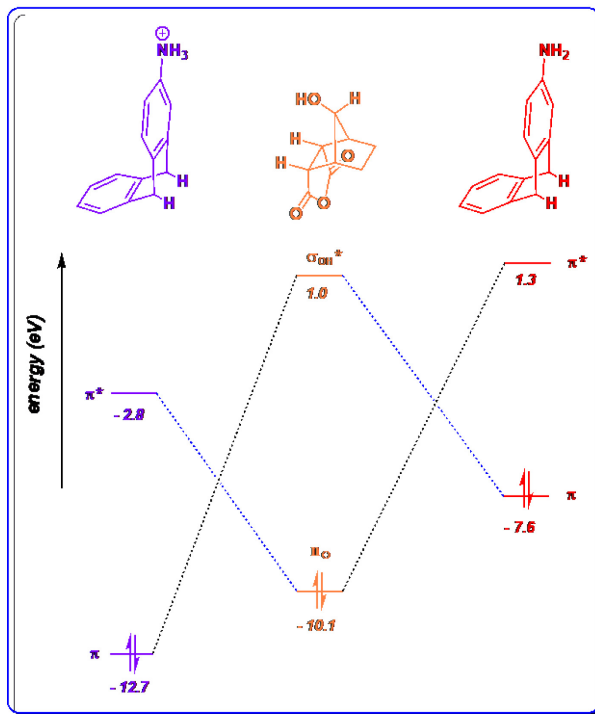
Figure 7.10. *MO diagram representing favorable $n_o – \pi^*$ and $\pi – \sigma^*$ interactions in fragments of 5–H⁺ and 5*

(ωB97XD/6-311+G**).

Additionally, electrostatic surface potentials (ESP) can provide an alternative explanation since these interactions are largely electrostatic in nature. A negative ESP on the aromatic fragment in **5** attracts the positive region of the OH bond, thereby locking the alcoholic proton in the *"in"* orientation. On the contrary, a positive ESP on the aromatic fragment in **5**–H⁺ attracts the negative region of the OH containing fragment, thereby reversing the orientation of the alcoholic proton.

Isodesmic relations comparing the energies of *in* and *out* rotamers (Figure **7.3**) can also be explained in terms of the π–σ^* and n_o–π^* overlapping trends observed in Figure **7.9**. For example, π–OH σ^* interactions are dominant in **1** and **5**, which pushes the equilibrium towards the *in*-form, whereas dominant n_o–π^* interactions in **5**–H⁺ swing the equilibrium towards the *out*-form. For **3**, however, the two interactions have similar energy gaps (10.2 eV and 10.8 eV for π–OH σ^* and n_o–π^* respectively) that keep the equilibrium constant near unity (gas phase).

58

7.5 ^{1}H NMR Analysis

We utilized coupling constants between the OH and geminal protons as a qualitative assessment of the extent of OH···π interactions. The supposition is that stronger OH···π interactions slow exchange and thereby allow couplings to be measured. In systems with weak or nonexistent OH···π interactions, more rapid exchange is expected. Experimentally, alcoholic protons in the series appear as doublets with coupling constants of 3.9 Hz, 5.4 Hz, 7.5 Hz, 10.9 Hz and 11.8 Hz in **2**, **3**, **6** (monobrominated analogue)**, 1** and **5** respectively (Figure **7.11**).[21] Calculations (B3LYP/6-31G(d) and B3LYP/6-311+G(2d,p)) also predict stronger coupling (13–14 Hz for *in*-forms vs. 0–6 Hz for *out*-forms). As expected, increasing electronic density on the adjacent *top* ring holds the alcoholic proton more tightly due to stronger OH···π hydrogen bonding; therefore, geminal coupling is observed.

We previously observed that the alcoholic proton in prototype molecule **1** appears fairly shielded (-0.21 ppm) and sharp compared to the *out* diastereomer **7**, in which it appears relatively deshielded (1.16 ppm) as a broadened peak. Additionally, the alcoholic protons in **3** and **6** appear some 0.39 ppm and 0.36 ppm deshielded compared to the same proton in **1**.[21] Furthermore, the proton geminal to the OH group appears at 3.85 ppm and 2.52 ppm in **1** and its diastereomer **7**, suggesting that H···arene interactions experience shielding effects.[21] We attributed these observations to aromatic ring current effects, i.e., reducing H···π distance shields the interacting proton. We argued that weak OH···π interactions in **3** and **6** lock the alcoholic proton in the *out*-form, therefore it is affected by ring current to a lesser extent.[21]

However, the OH proton of **5** appears at 0.37 ppm, some 0.58 ppm downfield compared to **1**. Calculations (B3LYP/6-31G(d) and B3LYP/6-311+G(2d,p)) predict the alcoholic protons of the *in*-forms to be *deshielded* compared to the *out*-forms in these molecules, whereas ring current interactions should *shield* the interacting protons (Table **7.2**). These effects become apparent in the ^{1}H spectra as we move from **3** to **6** to **1**. In **5**, however, hydrogen bond effects dominate, and the hydroxyl proton moves back to the positive region of ^{1}H spectrum (0.37 ppm, Figure **7.11**). Finally, an outlier is observed in **2** wherein the "alcoholic proton" resonates downfield than **5**. The aromatic electron density in this system is probably low enough

that the hydroxyl proton is "locked" in the *out*-form. Therefore, it can benefit neither from OH···π hydrogen bonding nor from enhanced ring current effects.
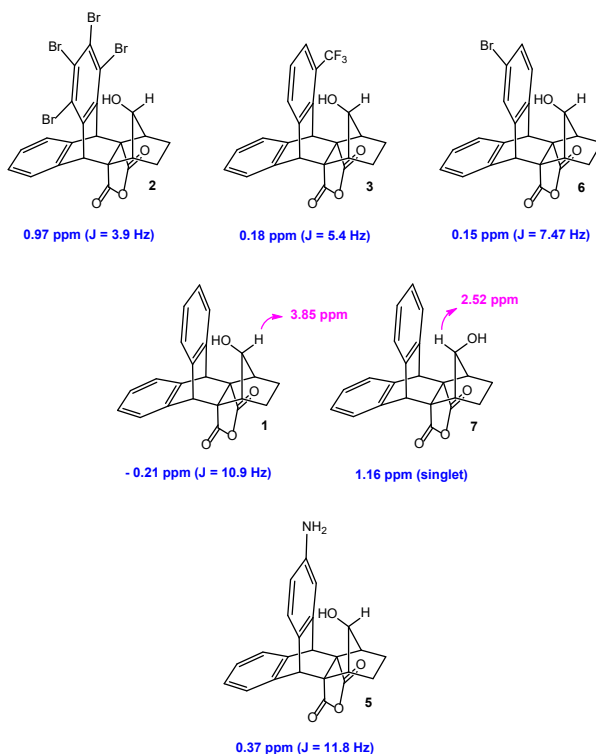
Figure 7. 11. Chemical shifts of alcoholic protons and their coupling constants in the experimental ^{1}H spectra of 1, 2, 3, 5, 6 and 7.

[1]H chemical shift	R = NH$_3^+$	CF$_3$	Br	H	NH$_2$
in-form	2.72	2.72	2.49	2.48	1.52
out-form	0.78	0.95	0.19	0.30	0.46
experimental	-	0.18	0.15	- 0.21	0.37

Table 7.2. Calculated (scaled)[31] chemical shifts of alcoholic protons in the in and out forms of 1, 3, 5, 5–H⁺ and 6 (B3LYP/6-31G(d)) and the experimentally observed values.

7.6 Conclusion

In this article, we have investigated the effects of an aromatic ring's electronic nature on the strength of OH···π hydrogen bonding interactions. Both predicted and experimental IR stretches indicate a direct

correlation between the strength of these interactions and electron density of the π system. The OH stretching frequency red shifts by roughly 50 cm^{-1} when the substituent on the aryl ring is modified from CF$_3$ to NH$_2$, indicating a significantly stronger HB interaction in the latter case. X-ray crystal structures of various analogues reveal that electron deficient systems lock the "oxygen-bound hydrogen" in the *out*-form whereas electron rich systems reverse its orientation. Additionally, the crystal structure of top amino analogue **5** reveals an extended hydrogen bond network that effectively dimerizes the system. DFT calculations further suggest that systems with electron rich aromatic rings show more favorable π–OH σ* interactions whereas systems with electron poor aromatic rings depict preferential n–π* interactions. Finally, ^{1}H NMR analysis reveals that stronger OH···π interactions slow exchange of the "alcoholic proton", thereby increasing its coupling constant with the geminal proton. We hope that these results provide additional insights into the significant role of nonconventional hydrogen bonding interactions across a variety of scientific fields.

7.7 References

1. Malone, J. F.; Murray, C. M.; Charlton, M. C.; Docherty, R.; Lavery, A. J. *J. Chem. Soc. Far. Trans.* **1997**, *93*, 3429-3436.

2. Meyer, E. A.; Castellano, R. K.; Diederich, F. *Angew. Chem. Int. Ed.* **2003**, *42*, 1210-1250.

3. Burley, S. K.; Petsko, G. A. *FEBS Lett.* **1986**, *203*, 139-143.

4. Zheng, H.; Comeforo, K.; Gao, J. *J. Am. Chem. Soc.* **2009**, *131*, 18-19.

5. Duan, G.; Smith, V. H.; Weaver, D. F. *J. Phys. Chem. A* **2000**, *104*, 4521-4532.

6. Hughes, R. M.; Waters, M. L. *J. Am. Chem. Soc.* **2006**, *128*, 13586-13591.

7. Toth, G.; Murphy, R. F.; Lovas, S. *J. Am. Chem. Soc.* **2001**, *123*, 11782-11790.

8. Ji, X.; Zhang, P.; Armstrong, R. N.; Gilliland, G. L. *Biochemistry* **1992**, *31*, 10169-10184.

9. Xiao, G.; Liu, S.; Ji, X.; Johnson, W. W.; Chen, J.; Parsons, J. F.; Stevens, W. J.; Gilliland, G. L.; Armstrong, R. N. *Biochemistry* **1996**, *35*, 4753-4765.

10. Sulpizi, M.; Carloni, P. *J. Phys. Chem. B* **2000**, *104*, 10087-10091.

11. Steiner, T.; Koellner, G. *J. Mol. Biol.* **2001**, *305*, 535-557.

12. Banerjee, P.; Chakraborty, T. *J. Phys. Chem. A* **2014**, *118*, 7074-7084.

13. Malenov, D. P.; Janjic, G. V.; Veljkovic, D. Z.; Zaric, S. D. *Comput. Theor. Chem.* **2013**, *1018*, 59-65.

14. Saggu, M.; Levinson, N. M.; Boxer, S. G. *J. Am. Chem. Soc.* **2011**, *133*, 17414-17419.

15. Mohan, N.; Vijayalakshmi, K. P.; Koga, N.; Suresh, C. H. *J. Comput. Chem.* **2010**, *31*, 2874-2882.

16. Toth, G.; Bowers, S. G.; Truong, A. P.; Probst, G. *Curr. Pharm. Des.* **2007**, *13*, 3476-3493.

17. Motherwell, W. B.; Moïse, J.; Aliev, A. E.; Nic, M.; Coles, S. J.; Horton, P. N.; Hursthouse, M. B.; Chessari, G.; Hunter, C. A.; Vinter, J. G. *Angew. Chem. Int. Ed.* **2007**, *46*, 7823-7826.

18. Aliev, A. E.; Arendorf, J. R. T.; Pavlakos, I.; Moreno, R. B.; Porter, M. J.; Rzepa, H. S.; Motherwell, W. B. *Angew. Chem. Int. Ed.* **2015**, *54*, 551-555.

19. Paruch, K.; Vyklicky, L.; Wang, D. Z.; Katz, T. J.; Incarvito, C.; Zakharov, L.; Rheingold, A. L. *J. Org. Chem.* **2003**, *68*, 8539-8544.

20. Hong, J.; Yang, G.; Duan, C.; Guo, Z.; Zhu, L. *Inorg. Chem. Commun.* **2005**, *8*, 988-991.

21. Guan, L.; Holl, M. G.; Pitts, C. R.; Struble, M. D.; Siegler, M. A.; Lectka, T. *J. Am. Chem. Soc.* **2017**, *139*, 14913-14916.

22. Mataka, S.; Mitoma, Y.; Sawada, T.; Thiemann, T.; Taniguchi, M.; Tashiro, M. *Tetrahedron* **1998**, *54*, 5171-5186.

23. Desiraju, G. R.; Steiner, T. The Weak Hydrogen Bond in Structural Chemistry and Biology; Oxford University Press: New York, 2001.

24. Saggu, M.; Levinson, N. M.; Boxer, S. G. *J. Am. Chem. Soc.* **2012**, *134*, 18986-18997.

25. Arunan, E.; Desiraju, G. R.; Klein, R. A.; Sadlej, J.; Scheiner, S.; Alkorta, I.; Clary, D. C.; Crabtree, R. H.; Dannenberg, J. J.; Hobza, P.; Kjaergaard, H. G.; Legon, A. C.; Mennucci, B.; Nesbitt, D. J. *Pure Appl. Chem.* **2011**, *83*, 1637-1641.

26. Joseph, J.; Jemmis, E. D. *J. Am. Chem. Soc.* **2007**, *129*, 4620-4632.

27. Duarte, L. J.; Silva, A. F.; Richter, W. E.; Bruns, R. E. *J. Phys. Chem. A* **2019**, *123*, 6482-6490.

28. Mao, Y.; Gordon, M. H. *J. Phys. Chem. Lett.* **2019**, *10*, 3899-3905.

29. Wang, C.; Mo, Y. *Inorg. Chem.* **2019**, *58*, 8577-8586.

30. The position of CF_3 group on adjacent *top* ring was kept identical to the NH_2 analogue for consistency in calculations. However, due to synthetic challenges, the synthesized *top* CF_3 analogue places the deactivating group on the side position.

31. Pierens, G. K. *J. Comput. Chem.* **2014**, *35*, 1388-1394.

32. Brinkley, R. L.; Gupta, R. B. *AIChE J.* **2001**, *47*, 948-953.

Chapter 8: Structural Proof of a [C-F-C]+ Fluoronium Cation

8.1 Introduction

"Nonclassical" molecular structures - which demand paradigm shifts in the way we think about core concepts in chemical bonding - are inherently a source of controversy in chemistry. Historically, structural debates have persisted on the notion that data obtained from even the most robust solution-phase spectroscopies (e.g., NMR) are still subject to interpretation; thus, chemists tend to rely on crystallographic techniques to provide indisputable *proof* and bring the case to a definitive close. One example of such a contentious molecular structure is the organic fluoronium ion, as this would require the most electronegative and least polarizable element to engage in two partially covalent bonding interactions. However, in recent years, strides have been made in generating A) indirect evidence for the involvement of a symmetrical [C-F-C]$^+$ fluoronium ion intermediate in solvolysis experiments[1,2] and B) NMR spectroscopic evidence for a metastable fluoronium ion in superacidic media.[3,4] While these studies strongly support the divalent fluoronium structure over the alternative rapidly equilibrating classical carbocation, the model system has, to date, eluded crystallographic analysis to confirm this phenomenon in the solid state. Concluding a scrupulous effort, we now report a thorough analysis of the first single crystal structure of a [C-F-C]$^+$ fluoronium ion.

According to IUPAC, halonium ions are defined as ions of the form R_2X^+, where X may be any halogen.[5] In the case of organic halonium ions, R is defined as a cyclic or open-chained hydrocarbon backbone. Since they were first discussed as reactive intermediates in organic halogenation reactions in 1937,[6] a large variety of stable and structurally characterizable iodo-,[7,8] bromo-,[9,10] and chloronium[11,12] salts of the type [C-X-C]$^+$ have been synthesized. On the other hand, fluoronium cations, in which formally positively charged divalent fluorine atom (as depicted in a simplifying Lewis dot structure) is symmetrically bound to two carbon atoms, have only been reported thus far in spectroscopic investigations. For instance, Morton *et al.* first reported the existence of a three-membered cyclic fluoriranium ion as an intermediate in mass-spectrometry experiments,[13] while Gabbaï and co-workers obtained the structure of a methylium cation

that shows an intramolecular bonding interaction to an adjacent fluorine atom, allowing a description as an unsymmetrically bridged fluoronium cation (Figure **8.1**).[14]

In 2013, Lectka *et al.* presented the transient generation of a symmetrically bridged fluoronium cation in solution starting from a rigid double-norbornyl type precursor. Its formation as a fleeting reactive intermediate was indicated through isotopic labeling experiments.[1,2] Finally, in 2018 they observed the aforementioned fluoronium ion by NMR spectroscopy;[3,4] yet, the structural proof of this organic fluoronium ion in the solid state remained a lofty goal. In addition to these few spectroscopic examples of carbon-based fluoronium cations, some inorganic cations have been investigated in the past. A crystal structure of a cyclic disilylfluoronium salt was reported by Müller and coworkers in 2006, followed by a structure of an open-chained bissilylated fluoronium cation by Schulz in 2009.[15-17] More recently in 2018, Kraus presented examples of a fluorine atom coordinated by two BrF_2 units (Figure **8.1**).[18,19]
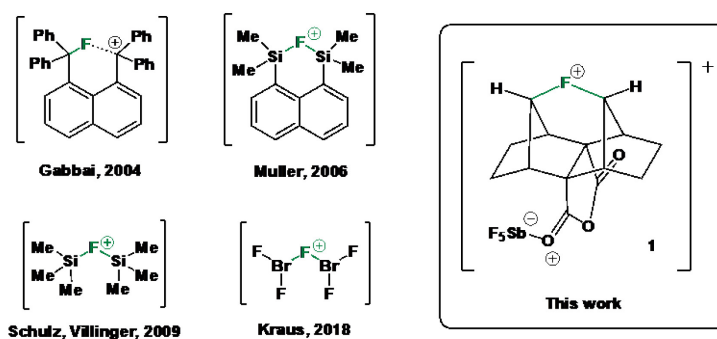
Figure 8.1. Crystallographically characterized fluoronium ions.[4-8]

Following up on the work of one of the coauthors, herein we present a modified synthesis and the first structural investigation of the carbon-based double norbornyl type fluoronium ion **1** (Figure **8.1**) as the $[Sb_2F_{11}]^-$ salt by single crystal X-ray diffraction. Furthermore, the bonding situations of $[C-X-C]^+$ (X = F, Cl, Br, I) are discussed and compared considering detailed AIM calculations and properties of **1** are further analyzed through vibrational spectroscopy.

8.2 Results and Discussion

Our approach is, in principle, based on utilizing the strong Lewis acid SbF_5 as a fluoride ion abstractor.[4] Herein, neat SbF_5 was substituted by the crystalline solvent-adduct $SbF_5 \cdot SO_2$ due to its slightly weakened acidic character and more convenient handling (Scheme **8.1**). By adding precursor **2** to a cooled mixture of $SbF_5 \cdot SO_2$ in SO_2ClF, a yellow solution is formed. Partial evaporation of the SO_2ClF and consecutive slow cooling of the reaction mixture afforded single crystals suitable for X-ray diffraction.
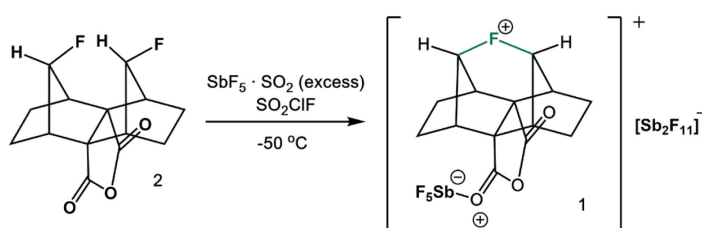
Scheme 8.1. Synthesis of the fluoronium salt [1][Sb₂F₁₁].

The compound $[\mathbf{1}][Sb_2F_{11}] \cdot (SO_2ClF)_3$ (Figure **8.2**) crystallizes in the centrosymmetric monoclinic space group $P2_1/c$ along with three solvent molecules per asymmetric unit. A nearly symmetrical C-F-C bonding array is structurally observed for the first time. The bridging fluorine atom F1 and its adjacent carbon atoms feature bond lengths of 156.6(3) and 158.5(3) pm with an overall C1-F1-C2 bond angle of 115.78(15)°. This is consistent with the data of the quantum-chemical computed structure of cation **1** with C-F bond distances of 157.4 and 160.1 pm and a C-F-C angle of 115.32° (B3LYP/cc-pVTZ). Compared to the unsymmetrical bridging fluorine atom in Gabbaï's bis-naphthalene complex with C-F distances of 142.4 and 244.4 pm, the distances in cation **1** are in between.[14] No interaction between anion and cation can be observed, although as predicted in previous publications, a single SbF_5 coordinates to the anhydride function of the cation. The coordinating SbF_5 is slightly bent out of the anhydride plane with a dihedral angle <(O2-C14-O1-Sb1)=19.0(4)°, resulting in a C_1 symmetry of the cation. Lectka previously assumed C_s symmetry from their NMR analysis of this compound.[3]
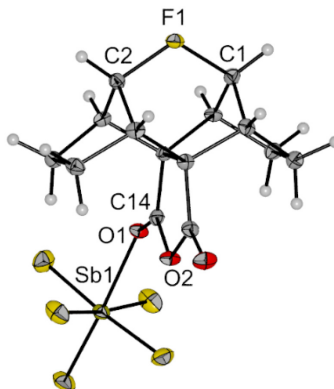
Figure 8.2. *Molecular structure of the fluoronium ion 1 as its [Sb$_2$F$_{11}$]·(SO$_2$ClF)$_3$ salt in the solid state. Anion and solvent molecules are not depicted. Thermal ellipsoids set to 50% probability. Selected bond lengths [pm] and angles [°]: F1−C1 156.6(3), F1−C2 158.7(3), C1−F1−C2 115.64(17), O2−C14−O1−Sb1 19.0(4).*

The vacuum-dried crystalline material was investigated by IR spectroscopy at −40 °C. A comparison with the spectrum of precursor **2** and the calculated vibrational spectra of cation **1** and anion [Sb$_2$F$_{11}$]$^-$ allows the assignment of an antisymmetric C-F stretching mode at 581 cm^{-1} (calc. 560 cm^{-1}), a vibration of the fluorine atom along the O-F axis of the molecule at 502 cm^{-1} (calc. 471 cm^{-1}) and a rocking deformation vibration in the C-F-C plane at 260 cm^{-1} (calc. 291 cm^{-1}) for the experimental spectrum of compound [**1**][Sb$_2$F$_{11}$] (see Figure **8.3**). The band of the symmetric C-F-C stretching vibration is overlaid by strong Sb-F vibrational bands. The C-F-C vibrations are strongly red-shifted compared to conventional monovalent C-F vibrations (usually observable between 1300-900 cm^{-1}),[20] indicating a rather weak C-F bond in fluoronium **1**. This is in line with similar findings of Dopfer *et al.* and their calculations on phenylfluoronium *F*-C$_6$H$_6$F$^+$.[21] Furthermore, a higher symmetric C-F-C mode suggests a strong vibrational coupling between the two C-F modes and a relatively small C-F-C angle. This is indicative for a covalent contribution to the C-F-C bond, which is in agreement with our bond analysis (see below). Lastly, a splitting of the former degenerated C=O vibrations due to coordination of SbF$_5$ to one of the carbonyl functions to bands at 1913 (n(C=O)) and 1614 (n(C=O···SbF$_5$)) cm^{-1} is observable.
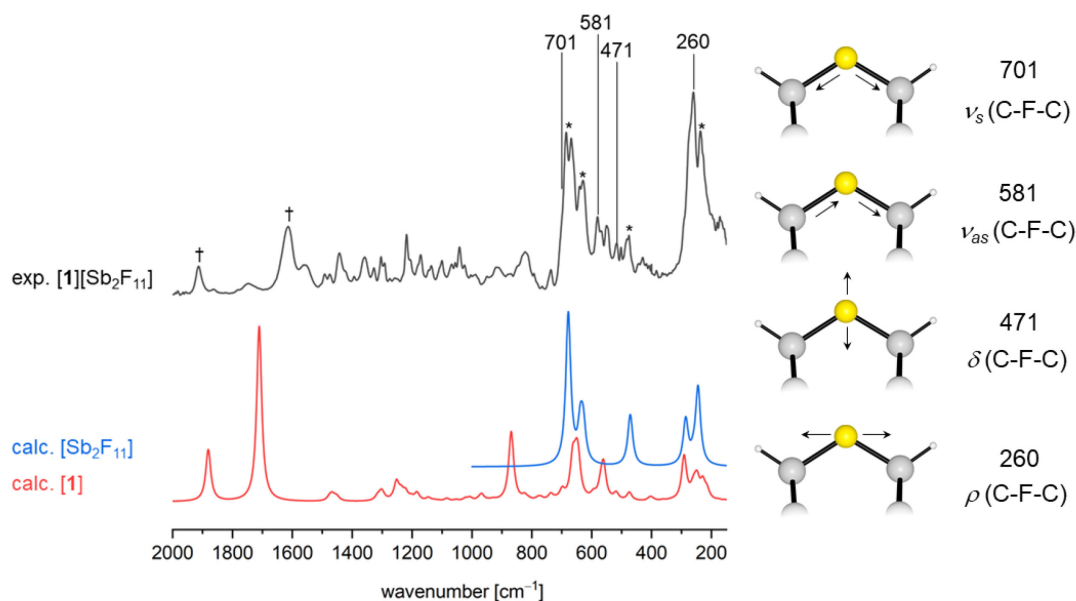
Figure 8.3. *Left side: Experimental infrared spectrum of [1][Sb$_2$F$_{11}$] and calculated spectra of cation 1 and anion [Sb$_2$F$_{11}$]$^-$ at B3LYP/def2-TZVPP level of theory. Bands of the anion are denoted with an asterisk. Bands of coordinated and non-coordinated carbonyl functions are denoted with a dagger. Right side: Depiction of C-F-C specific vibrations of 1 (only relevant part of molecule shown) and their corresponding assignment.*

Previous quantum-chemical studies focused on the atomic or partial charge of the fluorine atom in order to confirm its classification as a *fluoronium ion*.[22] Atomic charges, however, strongly depend on the computational level and are not uniquely defined. In the present case, a non-exhaustive selection of population analyses yields −0.260 (NBO; all charges are given in atomic units), −0.136 (Mulliken), −0.132 (CHELPG), −0.521 (AIM), −0.094 (Merz-Kollmann), +0.058 (Voronoi), and +0.382 (Löwdin) for the bridging fluorine atom. For all methods, the neighboring carbon atoms yield a positive partial charge.

Perhaps a more relevant aspect is how the fluorine atom is bound to its two neighboring sp^3-carbon atoms. As pointed out elsewhere, an AIM analysis shows two bond critical points (BCPs), indicating a chemical bond.[3,4] Judging from the different properties at these BCPs (ρ_{BCP} = 0.95 Å^{-3}; $\nabla^2\rho_{BCP}$ = −6.43 Å^{-5}; ELF$_{BCP}$ = 0.43; |V|/G = 2.05) the bonds are barely covalent, most likely due to some charge-shift character arising from the repulsion between lone pairs of electrons at the fluorine atom and the C-F σ-bonds. This

bond character differs significantly from the one in [H-F-H]$^+$ (ρ_{BCP} = 2.03 Å^{-3}; $\nabla^2\rho_{BCP}$ = −68.44 Å^{-5}; ELF$_{BCP}$ = 0.98; |V|/G = 16.44), which is genuinely covalent.[23]

To compare cation **1** to its heavier analogs, the fluorine atom was replaced by other halogens. The positions of the halogen atoms, the two neighboring carbon atoms, and the two nearest hydrogen atoms were re-optimized, while all other atoms were kept fixed. Table **1** lists the most important properties of the BCPs in these four systems and in [H-F-H]$^+$.

system	r_{X-C} [Å]	r_{BCP-X} − ½ r_{X-C} [Å]	ρ_{BCP} [Å^{-3}]	$\nabla^2\rho_{BCP}$ [Å^{-5}]	ELF$_{BCP}$	ELF$_{max}$	|V|/ G	^{val}LI$_X$	DLI$_{X-C}$	^{val}LI$_{C/H}$
fluoronium	1.5871	0.20	0.946	−6.432	0.43	—	2.05	6.72	0.58	1.84
chloronium	1.8852	0.17	0.964	−2.614	0.80	0.87	2.49	5.82	0.85	1.91
bromonium	2.0236	0.16	0.849	−1.616	0.82	0.83	2.40	4.73	0.89	1.95
iodonium	2.2006	0.14	0.729	−1.099	0.80	0.82	2.33	5.32	0.94	2.03
[H-F-H]$^+$	0.9679	0.35	2.027	−68.62	0.98	—	16.5	7.42	0.27	0.01

Table 8. 1. *Properties of the bonds with the halogen atom in different halonium ions: bond length (r_{X-C}); deviation of the BCP from the mid-point of the bond (r_{BCP-X} − ½ r_{X-C}; for negative values, the BCP is closer to the halogen atom, for positive values, vice versa); electron density at the BCP (ρ_{BCP}); Laplacian at the BCP ($\nabla^2\rho_{BCP}$); ELF at the BCP (ELF$_{BCP}$); value of the the ELF maximum along the bond path (ELF$_{max}$); ratio of the absolute potential and the kinetic energy density at the BCP (|V|/G); localization index of the valence electrons at the halogen atom (^{val}LI$_X$); delocalization index of the bonds with the halogen atom (DLI$_{X-C}$); localization index of the valence electrons at the carbon or hydrogen atom bound to the halogen atom (^{val}LI$_{C/H}$).*

As the X-C bond distance increases and the X-C bond becomes less polarized, the BCP approaches the mid-point of the X-C bond path. With increasing bond length, the electron density and its curvature at the BCP decreases, although the number of electrons associated with this bond increases, which can be seen from raising ELF (Electron Localization Function) values and delocalization indices DLI_{X-C}. The covalent character in the chlorine analogue is slightly larger than in the fluoronium cation and decreases again for the bromonium and iodonium cation. Nevertheless, it never reaches values typical for genuine covalent bonds as in $[H-F-H]^+$. In Figure **8.4**, ELF maps for the fluoronium and chloronium cations are shown for the C-X-C plane (left) and the one perpendicular to that containing the halogen lone pairs (right). All four systems clearly indicate covalent interactions between carbon and the halogen atom, with the fluoronium cation resembling the least a genuine covalent interaction and the chloronium cation the most. In the former, the valence electrons of the fluorine atom seem the least polarized, resembling almost the ELF map of an ion. This might be reinforced by the adjacent hydrogen atoms that draw electron density from the lone pair region in the C-F-C plane, which can be considered as a fluorine specific interaction. For the other halonium cations, the valence shell is clearly separated into a maximum along the C-X bond path and two distinguished lone pairs.

In all, this work – loosely analogous to the report of the norbornyl cation crystal structure in 2013[24] – definitively verifies the nonclassical structure of a controversial and oft-considered "impossible" species.

fluoronium   chloronium
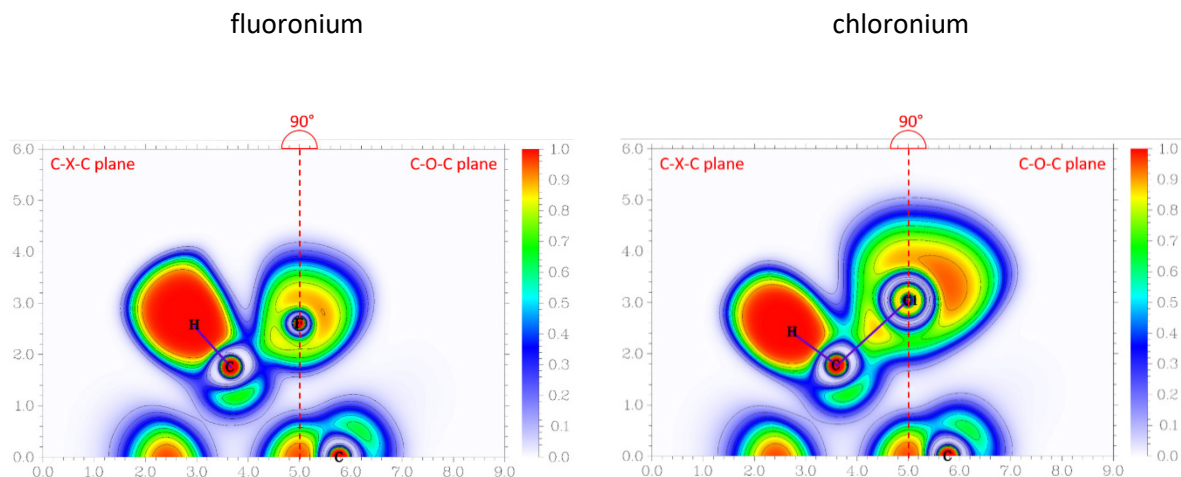
Figure 8. 4. *Electron localization function in the C-X-C plane and the C-O-C plane containing the halogen's lone pairs, perpendicular to the former one. Both planes are merged at the molecule's O-X axis (dashed red line). ELF is defined from 0.0 (white) to 1.0 (red); contours are drawn in intervals of 0.1.*

8.3 References

1. M. D. Struble, M. T. Scerba, M. Siegler, T. Lectka, *Science* **340**, 57-60 (2013).

2. M. D. Struble, M. G. Holl, M. T. Scerba, M. A. Siegler, T. Lectka, *J. Am. Chem. Soc.* **137**, 11476-11490 (2015).

3. C. R. Pitts, M. G. Holl, T. Lectka, *Angew. Chem.* **130**, 1942-1945 (2018).

4. C. R. Pitts, M. G. Holl, T. Lectka, *Angew. Chem. Int. Ed.* **57**, 1924-1927 (2018).

5. A. D. McNaught, A. Wilkinson, *IUPAC. Compendium of Chemical Terminology (the "Gold Book),* 2. Aufl., Blackwell Scientific Publications, Oxford, **1997**.

6. I. Roberts, G. E. Kimball, *J. Am. Chem. Soc.* **59**, 947-948 (1937).

7. V. V. Grushin, *Chem. Soc. Rev.* **29**, 315-324 (2000).

8. F. Bailly, P. Barthen, H.-J. Frohn, M. Köckerling, *Z. anorg. allg. Chem.* **626**, 2419-2427 (2000).

9. R. S. Brown, R. W. Nagorski, A. J. Bennet, R. E. D. McClung, G. H. M. Aarts, M. Klobukowski, R. McDonald, B. D. Santarsiero, *J. Am. Chem. Soc.* **116**, 2448-2456 (1994).

10. H.-J. Frohn, M. Giesen, D. Welting, V. V. Bardin, *J. Fluor. Chem.* **131**, 922-932 (2010).

11. E. S. Stoyanov, I. V. Stoyanova, F. S. Tham, C. A. Reed, *J. Am. Chem. Soc.* **132**, 4062-4063 (2010).

12. S. Hämmerling, G. Thiele, S. Steinhauer, H. Beckers, C. Müller, S. Riedel, *Angew. Chem.* **131**, 9912-9915 (2019).

13. N. Viet, X. Cheng, T. H. Morton, *J. Am. Chem. Soc.* **114**, 7127-7132 (1992).

14. H. Wang, C. E. Webster, L. M. Pérez, M. B. Hall, F. P. Gabbaï, *J. Am. Chem. Soc.* **126**, 8189-8196 (2004).

15. R. Panisch, M. Bolte, T. Müller, *J. Am. Chem. Soc.* **128**, 9676-9682 (2006).

16. M. Lehmann, A. Schulz, A. Villinger, *Angew. Chem. Int. Ed.* **48**, 7444-7447 (2009).

17. M. Lehmann, A. Schulz, A. Villinger, *Angew. Chem.* **2009**, *121,* 7580.

18. S. I. Ivlev, A. J. Karttunen, M. R. Buchner, M. Conrad, F. Kraus, *Angew. Chem. Int. Ed.* **57**, 14640-14644 (2018).

19. S. I. Ivlev, A. J. Karttunen, M. R. Buchner, M. Conrad, F. Kraus, *Angew. Chem.* **130**, 14850-14855 (2018).

20. K. Nakamoto, *Infrared and Raman spectra of inorganic and coordination compounds A: Theory and Applications in Inorganic Chemistry* (John Wiley & Sons Inc, Hoboken, N.J., 2009), p. 390.

21. N. Solcà, O. Dopfer, *J. Am. Chem. Soc.* **125**, 1421–1430 (2003).

22. K. O. Christe, R. Haiges, M. Rahm, D. A. Dixon, M. Vasiliu, *J. Fluor. Chem.* **204**, 6-10 (2017).

23. E. Espinosa, I. Alkorta, J. Elguero, E. Molins, *J. Chem. Phys.* **117**, 5529-5542 (2002).

24. F. Scholz, D. Himmel, F. W. Heinemann, P. v. R. Schleyer, K. Meyer, I. Krossing, *Science* **341**, 62-64 (2013).

Chapter 9: Experimental Section

9.1 General Methods

 Unless otherwise stated, all reactions were carried out under strictly anhydrous, air-free conditions under nitrogen. All solvents and reagents were dried and degassed by standard methods.[1] ^{1}H, ^{13}C and [^{1}H, ^{1}H]-NOESY spectra were acquired on a 400 MHz NMR whereas ^{19}F NMR spectra were collected on a 300 MHz NMR in CDCl$_3$ or CD$_3$CN at 25 °C (unless otherwise stated). The ^{1}H, ^{13}C and ^{19}F chemical shifts are given in parts per million (δ) with respect to an internal tetramethylsilane (TMS, δ 0.00 ppm) standard. NMR data are reported in the following format: chemical shifts (multiplicity (s = singlet, d = doublet, t = triplet, q = quartet m = multiplet), integration, coupling constants [Hz]). IR data were obtained using an FT-IR with a flat CaF$_2$ cell. HRMS analyses were completed using positive ion mode electrospray ionization (Apollo II ion source) on a Bruker 12.0 Tesla APEX -Qe FTICR-MS or Thermo Scientific Q-Exactive Orbitrap mass spectrometer. All measurements were recorded at 25 °C unless otherwise stated. Spectral data were processed with ACD/NMR Processor Academic Edition.

---

[1] Bradley, D.; Williams, G.; Lawton, M. *J. Org. Chem.* **2010**, 75, 8351-8354.

9.2 Experimental Section for Chapter 2

Crystal Structure of p-QM 1:

Figure 9.1. Crystal Structure (mercury image and ORTEP) of the p-QM 1 (Chapter 2)

All reflection intensities were measured at 110 K using a SuperNova diffractometer (equipped with Atlas detector) with Mo $K\alpha$ radiation (λ = 0.71073 Å) under the program CrysAlisPro (Version CrysAlisPro 1.171.39.29c, Rigaku OD, 2017). The same program was used to refine the cell dimensions and for data reduction. The structure was solved with the program SHELXS-2018/3 (Sheldrick, 2018) and was refined on F^2 with SHELXL-2018/3 (Sheldrick, 2018). Numerical absorption correction based on gaussian integration over a multifaceted crystal model was performed using CrysAlisPro. The temperature of the data collection was controlled using the system Cryojet (manufactured by Oxford Instruments). The H atoms were placed at calculated positions using the instructions AFIX 13, AFIX 23 or AFIX 43 with isotropic displacement parameters having values 1.2 or 1.5 U_{eq} of the attached C atoms. The structure is partly disordered. The asymmetric unit contains a lattice DCM solvent molecule, which is disordered as the molecule is located at a site of inversion symmetry. The occupancy factor was constrained to be 0.5.

Crystallographic experimental details

	xs1812a
Crystal data	
Chemical formula	2($C_{29}H_{20}O_4$)·CH_2Cl_2

M_r	949.82
Crystal system, space group	Triclinic, P-1
Temperature (K)	110
a, b, c (Å)	7.9839 (4), 9.8531 (4), 15.2245 (7)
α, β, γ (°)	72.988 (4), 89.602 (4), 80.801 (4)
V (Å^3)	1129.51 (9)
Z	1
Radiation type	Mo $K\alpha$
μ (mm^{-1})	0.21
Crystal size (mm)	0.19 × 0.10 × 0.06
Data collection	
Diffractometer	SuperNova, Dual, Cu at zero, Atlas
Absorption correction	Gaussian *CrysAlis PRO* 1.171.39.29c (Rigaku Oxford Diffraction, 2017) Numerical absorption correction based on gaussian integration over a multifaceted crystal model Empirical absorption correction using spherical harmonics, implemented in SCALE3 ABSPACK scaling algorithm.
T_{min}, T_{max}	0.792, 1.000
No. of measured,	11672, 5200, 4097

independent and observed [$I > 2\sigma(I)$] reflections	
R_{int}	0.025
$(\sin \theta/\lambda)_{max}$ (Å^{-1})	0.650
Refinement	
$R[F^2 > 2\sigma(F^2)]$, $wR(F^2)$, S	0.048, 0.116, 1.04
No. of reflections	5200
No. of parameters	325
No. of restraints	13
H-atom treatment	H-atom parameters constrained
$\Delta\rho_{max}$, $\Delta\rho_{min}$ (e Å^{-3})	0.36, -0.39

Computer programs: *CrysAlis PRO* 1.171.39.29c (Rigaku OD, 2017), *SHELXS2018*/3 (Sheldrick, 2018), *SHELXL2018*/3 (Sheldrick, 2018), *SHELXTL* v6.10 (Sheldrick, 2008).

Crystal Structure of 4

Figure 9.2. Crystal Structure (mercury image and ORTEP) of Compound 4 (Chapter 2)

All reflection intensities were measured at 110(2) K using a SuperNova diffractometer (equipped with Atlas detector) with Mo $K\alpha$ radiation (λ = 0.71073 Å) under the program CrysAlisPro (Version CrysAlisPro 1.171.39.29c, Rigaku OD, 2017). The same program was used to refine the cell dimensions and for data reduction. The structure was solved with the program SHELXS-2018/3 (Sheldrick, 2018) and was refined on F^2 with SHELXL-2018/3 (Sheldrick, 2018). Numerical absorption correction based on gaussian integration over a multifaceted crystal model was applied using CrysAlisPro. The temperature of the data collection was controlled using the system Cryojet (manufactured by Oxford Instruments). The H atoms were placed at calculated positions (unless otherwise specified) using the instructions AFIX 13, AFIX 23 or AFIX 43 with isotropic displacement parameters having values 1.2 or 1.5 U_{eq} of the attached C atoms. The structure is partly disordered.

In the asymmetric unit, the lattice chloroform solvent molecule is found at one site of inversion symmetry and is found disordered over two orientations. The occupancy factor was constrained to be 0.5.

The crystal that was mounted on the diffractometer was slightly twinned. The two components are related by a twofold rotational axis along the reciprocal -0.4467a$\mathbf{*}$ + 0.0009b$\mathbf{*}$ + 0.8947c$\mathbf{*}$ direction. The structure refinement was processed using the HKLF 5 instruction. The BASF scale factor refines to 0.0261(15).

Crystallographic experimental details

	xs1875a
Crystal data	
Chemical formula	$2(C_{29}H_{24}O_4)\cdot CHCl_3$
M_r	992.33
Crystal system, space group	Triclinic, P-1
Temperature (K)	110
a, b, c (Å)	8.3671 (2), 9.4622 (2), 15.1881 (5)

α, β, γ (°)	105.611 (2), 95.547 (2), 94.308 (2)
V (Å^3)	1146.25 (5)
Z	1
Radiation type	Mo $K\alpha$
μ (mm^{-1})	0.26
Crystal size (mm)	0.21 × 0.16 × 0.15
Data collection	
Diffractometer	SuperNova, Dual, Cu at zero, Atlas
Absorption correction	Gaussian *CrysAlis PRO* 1.171.39.29c (Rigaku Oxford Diffraction, 2017) Numerical absorption correction based on gaussian integration over a multifaceted crystal model Empirical absorption correction using spherical harmonics, implemented in SCALE3 ABSPACK scaling algorithm.
T_{min}, T_{max}	0.826, 1.000
No. of measured, independent and observed [$I > 2\sigma(I)$] reflections	20506, 6359, 4513
R_{int}	0.024
(sin θ/λ)$_{max}$ (Å^{-1})	0.654

Refinement	
$R[F^2 > 2\sigma(F^2)]$, $wR(F^2)$, S	0.049, 0.139, 1.00
No. of reflections	6359
No. of parameters	335
H-atom treatment	H-atom parameters constrained
$\Delta\rho_{max}$, $\Delta\rho_{min}$ (e Å^{-3})	0.70, -0.30

Computer programs: *CrysAlis PRO* 1.171.39.29c (Rigaku OD, 2017), *SHELXS2018*/3 (Sheldrick, 2018), *SHELXL2018*/3 (Sheldrick, 2018), *SHELXTL* v6.10 (Sheldrick, 2008).
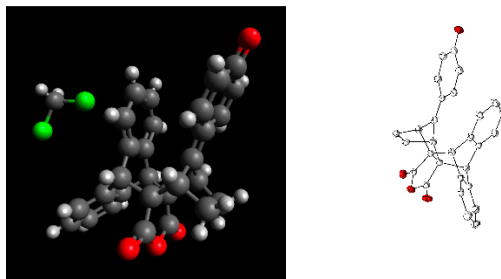
Crystal Structure of 5
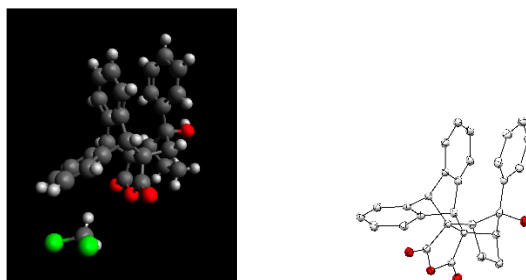
Figure 9.3. Crystal Structure (mercury image and ORTEP) of Compound 5 (Chapter 2)

All reflection intensities were measured at 110(2) K using a SuperNova diffractometer (equipped with Atlas detector) with Cu *K*α radiation (λ = 1.54178 Å) under the program CrysAlisPro (Version CrysAlisPro 1.171.39.29c, Rigaku OD, 2017). The same program was used to refine the cell dimensions and for data reduction. The structure was solved with the program SHELXS-2018/3 (Sheldrick, 2018) and was refined on F^2 with SHELXL-2018/3 (Sheldrick, 2018). Analytical numeric absorption correction using a multifaceted crystal model was applied using CrysAlisPro. The temperature of the data collection was controlled using the system Cryojet (manufactured by Oxford Instruments). The H atoms were placed at calculated

positions using the instructions AFIX 13, AFIX 23, AFIX 43 or AFIX 147 with isotropic displacement parameters having values 1.2 or 1.5 U_{eq} of the attached C or O atoms. The structure is mostly ordered. In the asymmetric unit, there is one disordered lattice DCM solvent molecule that is found at one site of inversion symmetry. Overall, its occupancy factor refines to 0.4433(13).

Crystallographic experimental details

	xs1967a
Crystal data	
Chemical formula	$C_{29}H_{22}O_4 \cdot 0.443(CH_2Cl_2)$
M_r	472.22
Crystal system, space group	Monoclinic, $P2_1/n$
Temperature (K)	110
a, b, c (Å)	8.37037 (17), 26.3667 (5), 10.3432 (2)
β (°)	108.918 (2)
V (Å^3)	2159.43 (8)
Z	4
Radiation type	Cu $K\alpha$
μ (mm^{-1})	1.75
Crystal size (mm)	0.28 × 0.06 × 0.03
Data collection	
Diffractometer	SuperNova, Dual, Cu at zero, Atlas

Absorption correction	Analytical *CrysAlis PRO* 1.171.39.29c (Rigaku Oxford Diffraction, 2017) Analytical numeric absorption correction using a multifaceted crystal model based on expressions derived by R.C. Clark & J.S. Reid. (Clark, R. C. & Reid, J. S. (1995). Acta Cryst. A51, 887-897) Empirical absorption correction using spherical harmonics, implemented in SCALE3 ABSPACK scaling algorithm.
T_{min}, T_{max}	0.769, 0.961
No. of measured, independent and observed [$I > 2\sigma(I)$] reflections	14500, 4251, 3489
R_{int}	0.037
$(\sin\theta/\lambda)_{max}$ (Å^{-1})	0.617
Refinement	
$R[F^2 > 2\sigma(F^2)]$, $wR(F^2)$, S	0.036, 0.093, 1.03
No. of reflections	4251
No. of parameters	327
No. of restraints	13
H-atom treatment	H-atom parameters constrained
$\Delta\rho_{max}$, $\Delta\rho_{min}$ (e Å^{-3})	0.26, -0.23

Computer programs: *CrysAlis PRO* 1.171.39.29c (Rigaku OD, 2017), *SHELXS2018*/3 (Sheldrick, 2018),

SHELXL2018/3 (Sheldrick, 2018), *SHELXTL* v6.10 (Sheldrick, 2008).
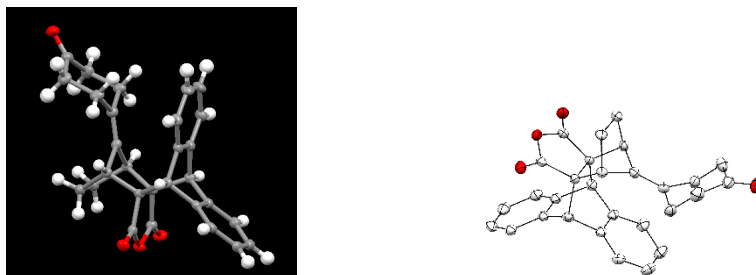
Crystal Structure of Compound 6
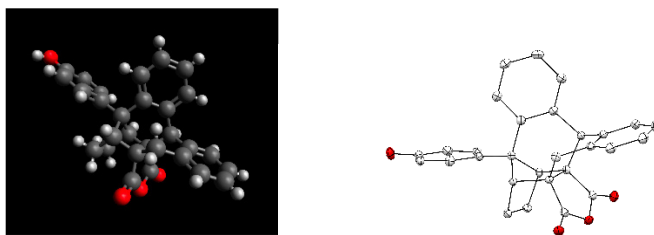
Figure 9.4. Crystal structure (mercury image and ORTEP) of Compound 6 (Chapter 2)

All reflection intensities were measured at 110 K using a SuperNova diffractometer (equipped with Atlas

detector) with Mo *K*α radiation (λ = 0.71073 Å) under the program CrysAlisPro (Version CrysAlisPro

1.171.39.29c, Rigaku OD, 2017). The same program was used to refine the cell dimensions and for data

reduction. The structure was solved with the program SHELXS-2018/3 (Sheldrick, 2018) and was refined on

F^2 with SHELXL-2018/3 (Sheldrick, 2018). Numerical absorption correction based on gaussian integration

over a multifaceted crystal model was performed using CrysAlisPro. The temperature of the data collection

was controlled using the system Cryojet (manufactured by Oxford Instruments). The H atoms were placed

at calculated positions (unless otherwise specified) using the instructions AFIX 13, AFIX 23 or AFIX 43 with

isotropic displacement parameters having values 1.2 U_{eq} of the attached C atoms. The H atom attached to

O4 was found from difference Fourier map, and its coordinates were refined pseudofreely using the DFIX

instruction in order to keep the O−H bond distance within an acceptable range. The structure is ordered.

Crystallographic experimental details

	xs1923a
Crystal data	
Chemical formula	$C_{29}H_{22}O_4$

M_r	434.46
Crystal system, space group	Triclinic, *P*-1
Temperature (K)	110
a, *b*, *c* (Å)	7.2809 (2), 11.2824 (3), 13.6279 (5)
α, β, γ (°)	74.115 (3), 75.617 (3), 73.108 (3)
V (Å^3)	1012.78 (6)
Z	2
Radiation type	Mo *K*α
μ (mm^{-1})	0.09
Crystal size (mm)	0.32 × 0.25 × 0.16
Data collection	
Diffractometer	SuperNova, Dual, Cu at zero, Atlas
Absorption correction	Gaussian *CrysAlis PRO* 1.171.39.29c (Rigaku Oxford Diffraction, 2017) Numerical absorption correction based on gaussian integration over a multifaceted crystal model Empirical absorption correction using spherical harmonics, implemented in SCALE3 ABSPACK scaling algorithm.
T_{min}, T_{max}	0.461, 1.000
No. of measured,	19204, 4660, 4240

independent and observed [$I > 2\sigma(I)$] reflections	
R_{int}	0.020
$(\sin\theta/\lambda)_{max}$ (Å^{-1})	0.650
Refinement	
$R[F^2 > 2\sigma(F^2)]$, $wR(F^2)$, S	0.038, 0.101, 1.04
No. of reflections	4660
No. of parameters	302
No. of restraints	1
H-atom treatment	H atoms treated by a mixture of independent and constrained refinement
$\Delta\rho_{max}$, $\Delta\rho_{min}$ (e Å^{-3})	0.37, -0.22

Computer programs: *CrysAlis PRO* 1.171.39.29c (Rigaku OD, 2017), *SHELXS2018*/3 (Sheldrick, 2018), *SHELXL2018*/3 (Sheldrick, 2018), *SHELXTL* v6.10 (Sheldrick, 2008).

**Synthesis and Characterization of Compounds**

9,10-dihydro-9,10-[4,7]methanoisobenzofuranoanthracene-12,14,15-trione (2):   Ketone **(2)** was synthesized by following the synthetic route found in the literature. Spectral and analytical data agreed with the previous reports.[2,3]

---

[2] Guan, L.; Holl, M. G.; Pitts, C. R. ; Struble, M. D.; Siegler, M. A.; Lectka, T. *J. Am. Chem. Soc.* **2017,** *139*, 14913 - 14916.

[3] Holl, M. G.; Struble, M. D.; Singal, P.; Siegler, M. A.; Lectka, T. *Angew. Chem.* **2016,** *128*, 8406-8409.

15-hydroxy-15-(4-methoxyphenyl)-9,10-dihydro-9,10-[4,7]methanoisobenzofuranoanthracene-12,14-dione (3): In a flame dried round bottomed flask, compound 2 (1.22 g, 3.43 mmol) was dissolved in 10 mL THF and 20 mL of 1M 4-Methoxyphenylmagnesium bromide solution in THF was added to the mixture. After refluxing the mixture for 10 hours under nitrogen atmosphere, the mixture was quenched with 1M HCl and extracted with ethyl acetate. Organic layer was then washed with brine, dried over $MgSO_4$ and concentrated under reduced pressure. The product **3** was purified by silica gel chromatography with a 20% ethyl acetate and hexanes solution as light yellow solid (1.1g, 2.37 mmol, 69% yield). ^{1}H NMR (CDCl$_3$) δ 7.27 (m, 4H), 7.12-7.14 (q, 2H), 7.05 – 7.07 (d, 2H, J = 8.7 Hz), 7.03 – 7.05 (q, 2H), 6.78 – 6.8 (d, 2H, J = 8.7 Hz), 4.82 (s, 2H), 3.74 (s, 3H), 2.96 (t, 2H), 1.68 (m, 2H), 1.4 (m, 2H), 0.46 – 0.47 (s, 1H); ^{13}C NMR (CDCl$_3$) δ 174, 158.6, 142.34, 142.1, 136.72, 127.4, 126.47, 126.44, 125.59, 124.66, 114.18, 90.28, 68.19, 55.3, 49.4, 47.86, 26.18; IR 3576, 2994, 2963, 2914, 1839, 1848, 1776, 1610, 1512 (cm^{-1}, CaF$_2$, CH$_2$Cl$_2$); HRMS (ESI-) calc for C$_{30}$H$_{24}$O$_5$Na$^+$: 487.1516, found 487.1508.

15-(4-oxocyclohexa-2,5-dien-1-ylidene)-9,10-dihydro-9,10-[4,7]methanoisobenzofuranoanthracene-12,14-dione (1): To a round bottomed flask containing compound **3** (730 mg, 1.57 mmol) was added 7 mL of SOCl$_2$ and few drops of Et$_3$N and the mixture was stirred at room temperature for 1 hour. The mixture was dissolved in 30 mL ethyl acetate and transferred to a separatory funnel. Deionized water (30 mL) was added to the funnel slowly (generates HCl gas vigorously if water is added quickly). Organic layer was then washed with brine (30 mL), dried over $MgSO_4$ and evaporated under reduced pressure. Product **1** was then isolated by silica gel chromatography with 30% ethyl acetate and hexanes solution as lemon yellow crystals (380 mg, 0.88 mmol, 56% yield). ^{1}H NMR (CDCl$_3$) δ 7.32 – 7.33 (q, 2H), 7.21 – 7.25 (m, 4H), 6.85 (q, 2H), 6.82 (d, 2H, J = 9.9Hz), 6.2 (d, 2H, J = 9.9Hz), 4.71 (s, 2H), 3.37 (m, 2H). 1.67 – 1.69 (m, 4H); ^{13}C NMR (CDCl$_3$) δ 186.14, 171.39, 164.74, 138.4, 137.93, 137.04, 129.34, 128.07, 127.99, 125.71, 125.38, 119.71, 64.98, 49.0, 44.4, 24.4; IR 2976, 2963, 2934, 2893, 1847, 1781, 1633,1578, 1466, 1460 (cm^{-1}, CaF$_2$, CH$_2$Cl$_2$); HRMS (ESI-) calc for C$_{29}$H$_{20}$O$_4$Na$^+$: 455.1254, found 455.1247.

15-(4-oxocyclohexylidene)-9,10-dihydro-9,10-[4,7]methanoisobenzofuranoanthracene-12,14-dione (4): Compound **1** (31 mg, 0.072 mmol) was dissolved in 25 mL THF in a round bottomed flask and a catalytic

amount of Pd/C was added to the mixture. H$_2$ gas was purged through the mixture and the reaction was observed with ^{1}H NMR for completion. After completion, mixture was filtered over celite and washed with 25 mL THF. The combined filtrate was evaporated under reduced pressure and the product was purified by silica gel chromatography with 20% ethyl acetate and hexanes solution as white solid (15.2 mg, 0.035 mmol, 49% yield). ^{1}H NMR (CDCl$_3$) δ 7.26 – 7.29 (m, 4H), 7.16 – 7.17 (q, 2H), 7.08 – 7.09 (q, 2H), 4.648 (s, 2H), 2.98 (m, 2H), 2.05 – 2.2 (m, 6H), 1.85 – 1.91 (m, 2H), 1.56 (m, 2H); ^{13}C NMR (CDCl$_3$) δ 211.2, 173.04, 140.05, 139.59, 139.06, 127.64, 127.44, 125.19, 124.98, 121.63, 64.96, 49.29, 43.14, 40.24, 27.7, 25.98; IR 3070, 3028, 2964, 2896, 1845, 1777, 1711 (cm^{-1}, CaF$_2$, CH$_2$Cl$_2$); HRMS (ESI-) calc for C$_{29}$H$_{24}$O$_4$Na$^+$: 459.1567, found 459.1568.

15-hydroxy-15-phenyl-9,10-dihydro-9,10-[4,7]methanoisobenzofuranoanthracene-12,14-dione (5): Compound **1** (178 mg, 0.412 mmol) was dissolved in 15 mL THF and set on ice-water bath. A solution of LAH (2 mL of 2 M solution in THF, 4 mmol) was added to the solution dropwise and the mixture was stirred at 0 ^{o}C for 1 hour. Reaction was quenched with 25 mL water and extracted with 25 mL ethyl acetate. Organic layer was washed with brine, dried over anhydrous MgSO$_4$ and evaporated under reduced pressure. Product was isolated by silica gel chromatography with 20% ethyl acetate and hexanes solution (60 mg, 0.138 mmol, 33.6%). ^{1}H NMR (CDCl$_3$) δ 7.12 (q, 2H), 7.01 (q, 2H), 6.97 (m, 2H), 6.9 (m, 1H), 6.85 (m, 2H), 6.78 (q, 2H), 6.43 (q, 2H), 4.64 (s, 2H), 3.23 (t, 2H), 2.43 (m, 2H), 1.63 (m, 2H), 0.67 (s, 1H); ^{13}C NMR (CDCl$_3$) δ 174, 143.78, 142.34, 140, 128.95, 128.07, 127.52, 127.11, 126.86, 126.31, 125.17, 92.11, 65.66, 49.07, 46.11, 28.21; IR 3591, 3026, 2996, 2959, 2917, 1850, 1779, 1771, 1461, 1356 (cm^{-1}, CaF$_2$, CH$_2$Cl$_2$); HRMS (ESI-) calc for C$_{29}$H$_{22}$O$_4$Na$^+$: 457.1410, found 457.1403.

5-(4-hydroxyphenyl)-5,6,10,14b-tetrahydro-7H,9H-5,9a,6-(epipropane[1,1,3]triyl)benzo[3,4]phenanthro[1,10a-c]furan-7,9-dione (6): Compound **1** (50 mg, 0.12 mmol) was dissolved in 5 mL CH$_3$CN and 2-mercaptoethanol (3 mL) was added to the solution. Then a few drops of triethylamine were added to the mixture before it was refluxed for 24 hours. The mixture was then dissolved in 50 mL ethyl acetate, transferred to a separatory funnel, washed with 2M KOH solution (50 mL * 5) and brine (50 mL). Organic layer was dried over MgSO$_4$ and evaporated under reduced pressure.

Product was isolated by silica gel chromatography with 10% ethyl acetate in hexanes solution as white solid (15 mg, 30% yield) (Product was subjected to chromatography twice in order to get cleaner NMR spectra). ^{1}H NMR (CD$_3$CN) δ 7.55 (d, 1H, J = 7.3Hz), 7.45 (dd, 1H, J = 8.36Hz, 2.4Hz), 7.36 (t, 1H), 7.27 (td, 1H), 6.91 – 7 (m, 6H), 6.87 (d, 1H, J = 7.5Hz), 6.8 (dd, 1H, J = 8.45Hz, 2.7Hz), 6.59 (dd, 1H, J= 7.9Hz, 1.3Hz), 4.94 (s, 1H), 3.25 (m, 2H), 3.09 (d, 1H, 15.1Hz), 2.21 (d, 1H, J = 15.1Hz), 1.8 (m, 1H), 1.64 (m, 1H), 1.4 (m, 1H), 1.9 – 1.94 (m, 1H); ^{13}C NMR δ 175.47, 173.32, 155.7, 141.8, 140.5, 134.63, 133.54, 133, 130.75, 129.33, 129.02, 128.53, 128.47, 128.26, 127.82, 126.98, 126.49, 116.09, 114.71, 64.56, 62.83, 59.2, 52.18, 49.72, 46.45, 35.78, 26.21, 23.35; IR 3579, 2961, 2931, 2906, 2854, 1844, 1779, 1738, 1514 (cm^{-1}, CaF$_2$, CH$_2$Cl$_2$); HRMS (ESI-) calc for C$_{29}$H$_{22}$O$_4$Na$^+$: 457.1410, found 457.1410.

9.3 Experimental Section for Chapter 3

Single Crystal X-Ray Crystallography

Crystal Structure of Cation 2:
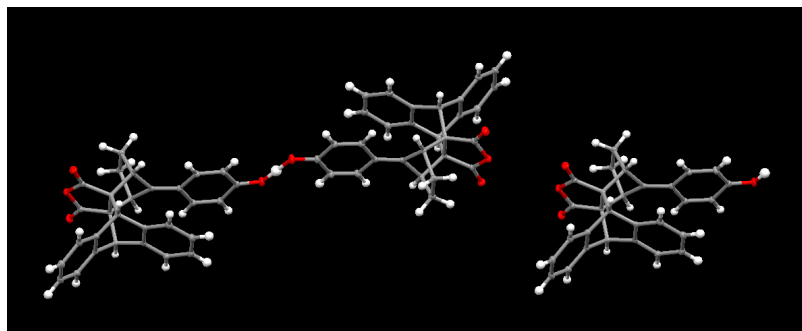
Figure 9.5. *Crystal Structure of Cation 2 (Chapter 3); TfO⁻ counter ions removed for clarity*

All reflection intensities were measured at 110(2) K using a SuperNova diffractometer (equipped with Atlas detector) with Mo $K\alpha$ radiation (λ = 0.71073 Å) under the program CrysAlisPro (Version CrysAlisPro 1.171.39.29c, Rigaku OD, 2017). The same program was used to refine the cell dimensions and for data reduction. The structure was solved with the program SHELXS-2018/3 (Sheldrick, 2018) and was refined on F^2 with SHELXL-2018/3 (Sheldrick, 2018). Numerical absorption correction based on gaussian integration over a multifaceted crystal model was applied using CrysAlisPro. The temperature of the data collection was controlled using the system Cryojet (manufactured by Oxford Instruments). The H atoms were placed at calculated positions (unless otherwise specified) using the instructions AFIX 13, AFIX 23 or AFIX 43 with isotropic displacement parameters having values 1.2 U_{eq} of the attached C atoms. The structure is partly disordered.

Figure 9.6. *Contoured Fourier map of the independent hydrogen bound proton (O4B represents the carbonyl oxygen of the QM attached to the proton whereas O4B* denotes the oxygen atom on QM generated by the Mercury program).*
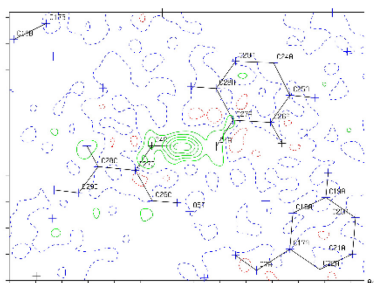
Figure 9.7. *Contoured Fourier map of the proton shared by the two p-QM molecules (O4A and O4C represent the carbonyl oxygen atoms of the QM moieties).*

The asymmetric unit contains three crystallographically independent molecules of the target compound and one and half triflate counterions. The molecules of the target compound are ordered, whereas the counterions are disordered. One triflate counterion is found at one site of no special positon (and is fully occupied), and is disordered over two orientations. The occupancy factor of the major component of the disorder refines to 0.5143(15). The other triflate counterion is found at one site of inversion symmetry and must be disordered as the triflate counterion does not have the inversion symmetry. Its occupancy factor must be constrained to 0.5. Overall, the negative charge carried by the triflate counterion in the asymmetric unit must be −1.5. This is consistent with the existence of 2 electron density peaks (2 H atoms) found near O4A, O4B and O4C, which overall carries a +1.5 charge. One of those peaks is found approximately equidistant from O4A and O4C, which suggests that one fully occupied H atom is shared with both O atoms; its occupancy factor must be 1. The other remaining peak is attached to O4B, which is donor to O4B* (O4B*

= O atom related to O4B by one inversion center), and its occupancy factor must be 0.5 as there would be

an impossible short O4B−H4B...H4B*−O4B* (* atoms generated by inversion symmetry) contact otherwise.

Contoured difference Fourier maps show unequivocally the existence of those two peaks.
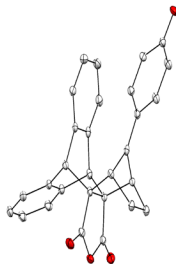
Figure 9.8. *Displacement ellipsoid plot (50% probability level) of one cationic part of the asymmetric unit of compound 2 (Chapter 3) at 110(2) K. H atoms and triflate counterions were removed for clarity.*

Sample Preparation

Compound 1 was dissolved in 3 mL of acetonitrile in a 3-dram screw cap vial. 2 equivalents of triflic acid

was added to the light-yellow solution which instantly turned dark amber. The solvent was evaporated very

slowly to grow the crystals.

Crystallographic experimental details

	xs1906a
Crystal data	
Chemical formula	$6(C_{29}H_{20.5}O_4)\cdot3(CF_3O_3S)$
M_r	3044.93
Crystal system, space group	Triclinic, P-1
Temperature (K)	110
a, b, c (Å)	9.2466 (2), 18.4489 (5), 20.5607 (5)

α, β, γ (°)	104.176 (2), 99.4171 (19), 94.7816 (19)
V (Å^3)	3326.75 (15)
Z	1
Radiation type	Mo $K\alpha$
μ (mm^{-1})	0.16
Crystal size (mm)	0.41 × 0.30 × 0.20
Data collection	
Diffractometer	SuperNova, Dual, Cu at zero, Atlas
Absorption correction	Gaussian *CrysAlis PRO* 1.171.39.29c (Rigaku Oxford Diffraction, 2017) Numerical absorption correction based on gaussian integration over a multifaceted crystal model Empirical absorption correction using spherical harmonics, implemented in SCALE3 ABSPACK scaling algorithm.
T_{min}, T_{max}	0.381, 1.000
No. of measured, independent and observed [$I > 2\sigma(I)$] reflections	61910, 15247, 12325
R_{int}	0.024
$(\sin \theta/\lambda)_{max}$ (Å^{-1})	0.650

Refinement	
$R[F^2 > 2\sigma(F^2)]$, $wR(F^2)$, S	0.042, 0.129, 1.02
No. of reflections	15247
No. of parameters	1061
No. of restraints	372
H-atom treatment	H atoms treated by a mixture of independent and constrained refinement
$\Delta\rho_{max}$, $\Delta\rho_{min}$ (e Å^{-3})	0.80, -0.50

Computer programs: *CrysAlis PRO* 1.171.39.29c (Rigaku OD, 2017), *SHELXS2018*/3 (Sheldrick, 2018), *SHELXL2018*/3 (Sheldrick, 2018), *SHELXTL* v6.10 (Sheldrick, 2008)

Generation of the protonated p-QM: Compound **1** (15 mg, 0.035 mmol) was dissolved in 1 mL CD$_3$CN in an NMR tube and 2 equivalents of trifluoromethanesulfonic acid (TfOH) were added to the tube. The light-yellow solution immediately turned dark amber. The sample was transferred to a vial and set aside for crystallization, which yielded yellow crystals over a matter of days. ^{1}H NMR (CD$_3$CN) δ 12.5 (s, broad) 7.83 (d, 2H, 9.3Hz), 7.43-7.44 (q, 2H), 7.38-7.39 (q, 2H), 7.32-7.33 (q, 2H), 7.135 (d, 2H, 9.3 Hz), 4.99-5.0 (s, 2H), 4.01 (m, 2H), 1.81 (m, 4H); ^{13}C{^{1}H} NMR δ 204.7, 181.0, 169.7, 149.5, 139.3, 137.2, 130.1, 128.4, 127.3, 125.6, 123.0, 121.0, 120.5, 66.3, 47.8, 47.4, 22.3.

9.4 Experimental Section for Chapter 4

Single Crystal X-Ray Crystallography

Crystal Structure of Compound 2
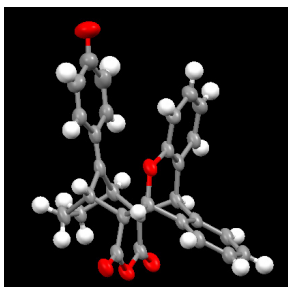
Figure 9.9. *Compound 2; product of photo-oxygenation of p-QM 1 (Chapter 4)*

All reflection intensities were measured at 110(2) K using a SuperNova diffractometer (equipped with Atlas detector) with Cu *K*α radiation (λ = 1.54178 Å) under the program CrysAlisPro (Version CrysAlisPro 1.171.39.29c, Rigaku OD, 2017). The same program was used to refine the cell dimensions and for data reduction. The structure was solved with the program SHELXS-2018/3 (Sheldrick, 2018) and was refined on F^2 with SHELXL-2018/3 (Sheldrick, 2018). Analytical numeric absorption correction using a multifaceted crystal model was applied using CrysAlisPro. The temperature of the data collection was controlled using the system Cryojet (manufactured by Oxford Instruments). The H atoms were placed at calculated positions using the instructions AFIX 13, AFIX 23 or AFIX 43 with isotropic displacement parameters having values 1.2 or 1.5 U_{eq} of the attached C atoms. The structure is mostly ordered. In the asymmetric unit, one void may potentially include a mixture of very disordered (and partially occupied) solvent molecules (possibly DCM/MeCN). In the final refinement, its contribution has been removed using the SQUEEZE procedure in Platon (Spek, 2009).

Crystallographic experimental details

	xs1924a
Crystal data	

Chemical formula	$C_{29}H_{20}O_5$
M_r	448.45
Crystal system, space group	Triclinic, P-1
Temperature (K)	110
a, b, c (Å)	8.0663 (5), 12.7882 (6), 13.3392 (11)
α, β, γ (°)	102.324 (5), 103.153 (6), 102.371 (4)
V (Å^3)	1258.07 (15)
Z	2
Radiation type	Cu $K\alpha$
μ (mm^{-1})	0.66
Crystal size (mm)	0.21 × 0.11 × 0.02
Data collection	
Diffractometer	SuperNova, Dual, Cu at zero, Atlas
Absorption correction	Analytical
CrysAlis PRO 1.171.39.29c (Rigaku Oxford Diffraction, 2017) Analytical numeric absorption correction using a multifaceted crystal model based on expressions derived by R.C. Clark & J.S. Reid. (Clark, R. C. & Reid, J. S. (1995). Acta Cryst. A51, 887-897) Empirical absorption correction using spherical harmonics, implemented in SCALE3 ABSPACK scaling algorithm.

T_{min}, T_{max}	0.919, 0.989
No. of measured, independent and observed [$I > 2\sigma(I)$] reflections	14928, 4504, 3584
R_{int}	0.036
$(\sin \theta/\lambda)_{max}$ (Å^{-1})	0.598
Refinement	
$R[F^2 > 2\sigma(F^2)]$, $wR(F^2)$, S	0.066, 0.183, 1.06
No. of reflections	4504
No. of parameters	310
H-atom treatment	H-atom parameters constrained
$\Delta\rho_{max}$, $\Delta\rho_{min}$ (e Å^{-3})	0.28, -0.22

Computer programs: *CrysAlis PRO* 1.171.39.29c (Rigaku OD, 2017), *SHELXS2018*/3 (Sheldrick, 2018), *SHELXL2018*/3 (Sheldrick, 2018), *SHELXTL* v6.10 (Sheldrick, 2008).

Photo-oxygenated product (Compound 2): p-QM **1** (74 mg, 0.17 mmol) was dissolved in 5 mL CH$_3$CN and exposed to 254 nm light in a rayonet reactor for 16 hours. The solution was exposed to air through a needle for complete conversion. Solvent was evaporated under reduced pressure and the product was isolated on a combi flash auto-column as yellow solid (27 mg, 0.06 mmol, 35% yield). ^{1}H NMR (CDCl$_3$) δ 7.31 – 7.38 (m, 4H), 7.22 (m, 1H), 7.048 (dd, 1H, J = 7.5Hz, 1.7Hz), 6.79 (td, 1H, J = 7.5Hz, 1.7Hz), 6.68 (td, 1H, J = 7.5Hz, 1.3Hz), 6.54 (dd, 1H, J = 9.9Hz, 2.5Hz), 6.37 (dd, 1H, J = 9.9Hz, 1.9Hz), 6.223 (dd, 1H, J = 8.2Hz, 1.13Hz), 5.97 (dd, 1H, J = 9.9Hz, 2Hz), 5.5 (s, 1H), 4.16 (s, 1H), 3.88 (d, 1H, J = 3.4Hz), 3.447 (d, 1H, J = 3Hz), 1.76 – 1.99 (m,

4H); ^{13}C NMR (CDCl$_3$) δ 186.46, 172.42, 170.31, 163.77, 153.94, 140.25,135.93, 135.54, 131.34, 130.92, 129.97, 129.53, 129.22, 129.06, 128.91, 128.56, 125.58, 123.33, 122.5, 122.19, 118.49, 63.75, 62.22, 49.42, 43.49, 43.3, 24.39, 24.13; IR 2979, 2930, 2895, 1850, 1780, 1636, 1582, 1487, 1453 (cm^{-1}, CaF$_2$, CH$_2$Cl$_2$); HRMS (ESI-) calc. for C$_{29}$H$_{20}$O$_5$Na$^+$: 471.120295, found 471.120208. (For ^{18}O$_2$ insertion, HRMS (ESI-) calc. for C$_{29}$H$_{20}$O$_4$^{18}O- : 449.128043, found 449.128116.)

Photoreduction Product (Compound 10): Compound **1** (50 mg, 0.12 mmol) was dissolved in a mixture of 7 mL CH$_3$CN and 1 mL CH$_3$OH. The reaction vessel was purged with N$_2$ for 5 minutes and then exposed to 254 nm light in a rayonet reactor for 12 hours. Solvent was removed under reduced pressure and the reaction mixture was subjected to gradient column chromatography in a combi-flash auto-column. Photoreduced product **10** was isolated as the major product (18 mg, 0.04 mmol, 36% yield). Its characterization data were consistent with those reported in the literature.

Photohydration product (Compound 11): Compound **1** (95 mg, 0.22 mmol) was dissolved in a mixture of 7 mL CH$_3$CN and 1 mL H$_2$O. The reaction flask was then purged with N$_2$ for 5 minutes and then exposed to 254 nm light in a rayonet reactor for 12 hours. Solvents were removed under reduced pressure and the product **11** was isolated on a combi flash auto-column as white solid (45 mg, 0.1 mmol, 46% yield). ^{1}H NMR (DMSO-d6) δ 9.41 (s, 1H), 7.61 (d, 1H, J = 7.5 Hz), 7.4 (m, 1H), 7.28 (td, 1H, J = 7.5Hz, 1.3 Hz), 7.16 (d, 1H, J = 7.5Hz), 6.96 (dd, 1H, J = 8.5Hz, 2Hz), 6.76 – 6.9 (m, 4H), 6.7 (dd, 1H, J = 8.5Hz, 2.5Hz), 6.36 (d, 1H, J = 7.5Hz), 4.86 – 4.93 (m, 2H), 4.81 (s, 1H), 3.67 (d, 1H, J = 2.5Hz), 3.18 (d, 1H, J = 3.5Hz), 1.84 (m, 1H), 1.72 (m, 1H), 1.56 (m, 1H), 1.23 (m, 1H); ^{1}H NMR (CD$_3$CN) δ 7.62 (dd, 1H, J = 7.5Hz, 1Hz), 7.44 – 7.51 (m, 2H), 7.35 (td, 1H, J = 7.5Hz, 1.4Hz), 7.25 (dd, 1H, J = 7.5Hz, 1Hz), 7.05 (s, 1H), 6.92 – 7.01 (m, 5H), 6.8 (dd, 1H, J = 8Hz, 2.7Hz), 6.57 (dt, 1H, J = 7.8Hz, 1Hz), 4.95 (d, 1H, J = 9Hz), 4.9 (s, 1H), 3.69 (dd, 1H, J = 3.7Hz, 1.25Hz), 3.21 (dd, 1H, J = 4.5Hz, 1.25Hz), 2 (m, 1H), 1.82 (m, 1H), 1.7 (m, 1H), 1.54 (d, 1H, J = 9Hz), 1.39 (m, 1H); ^{13}C NMR (DMSO-d6) δ 175.87, 173.71, 156.26, 141.83, 140.66, 137.57, 135.83, 132.82, 130.92, 130.88, 130.72, 129.68, 129.59, 129.51, 128.58, 128.16, 126.03, 125.97, 116.33, 115.18, 71.2, 65.08, 63.84, 63.49, 50.17, 49.34, 44.95, 26.56, 22.78; IR 3574.5, 2362.7, 1846.45, 1780.3, 1735.5, 1611.8, 1515.7 (cm^{-1}, CaF$_2$, CH$_2$Cl$_2$); HRMS (ESI+) calc for C$_{29}$H$_{23}$O$_5$$^+$: 451.15455, found 451.15326.

9.5 Experimental Section for Chapter 6

Single Crystal X-Ray Crystallography

Crystal Structure of Compound 3

  All reflection intensities were measured at 110(2) K using a SuperNova diffractometer (equipped with Atlas detector) with Mo $K\alpha$ radiation (λ = 0.71073 Å) under the program CrysAlisPro (Version CrysAlisPro 1.171.39.29c, Rigaku OD, 2017). The same program was used to refine the cell dimensions and for data reduction. The structure was solved with the program SHELXS-2018/3 (Sheldrick, 2018) and was refined on F^2 with SHELXL-2018/3 (Sheldrick, 2018).   Numerical absorption correction based on gaussian integration over a multifaceted crystal model was applied using CrysAlisPro. The temperature of the data collection was controlled using the system Cryojet (manufactured by Oxford Instruments). The H atoms were placed at calculated positions (unless otherwise specified) using the instruction AFIX 43 with isotropic displacement parameters having values 1.2 U_{eq} of the attached C atoms. The H atom attached to N2 was found from difference Fourier map, and its coordinates were refined freely. The structure is ordered.

Specified hydrogen bonds (with esds except fixed and riding H)

  D-H   H...A   D...A   <(DHA)

 0.876(17)   2.114(17)   2.9398(14)   156.9(14)   N2-H2N...O3_$2

 0.876(17)   2.218(15)   2.6501(13)   110.1(12)   N2-H2N...F1

Figure 9.10. *Displacement ellipsoid plot (50% probability level) of Compound 3 (Chapter 6)*

Sample Preparation

Compound **3** was dissolved in 3 mL dichloromethane in a 3-dram vial and the solvent was evaporated slowly

with the vial in slanted position. Crystals of compound **3** were formed when all the solvent had evaporated.

Experimental details

	xs2324a
Crystal data	
Chemical formula	$C_{17}H_{11}FN_2O_3$
M_r	310.28
Crystal system, space group	Monoclinic, $P2_1/c$
Temperature (K)	110
a, b, c (Å)	12.8867 (5), 4.97269 (15), 21.7966 (8)
β (°)	106.662 (4)
V (Å^3)	1338.11 (9)
Z	4
Radiation type	Mo $K\alpha$
μ (mm^{-1})	0.12
Crystal size (mm)	0.53 × 0.37 × 0.27
Data collection	
Diffractometer	SuperNova, Dual, Cu at zero, Atlas
Absorption correction	Gaussian *CrysAlis PRO* 1.171.39.29c (Rigaku Oxford Diffraction, 2017) Numerical

	absorption correction based on gaussian integration over a multifaceted crystal model Empirical absorption correction using spherical harmonics, implemented in SCALE3 ABSPACK scaling algorithm.
T_{min}, T_{max}	0.368, 1.000
No. of measured, independent and observed [$I > 2\sigma(I)$] reflections	19575, 3075, 2786
R_{int}	0.027
$(\sin \theta/\lambda)_{max}$ (Å^{-1})	0.650
Refinement	
$R[F^2 > 2\sigma(F^2)]$, $wR(F^2)$, S	0.036, 0.102, 1.07
No. of reflections	3075
No. of parameters	211
H-atom treatment	H atoms treated by a mixture of independent and constrained refinement
$\Delta\rho_{max}$, $\Delta\rho_{min}$ (e Å^{-3})	0.37, -0.25

Computer programs: *CrysAlis PRO* 1.171.39.29c (Rigaku OD, 2017), *SHELXS2018*/3 (Sheldrick, 2018), *SHELXL2018*/3 (Sheldrick, 2018), *SHELXTL* v6.10 (Sheldrick, 2008).

Crystal Structure of Compound 11

All reflection intensities were measured at 110(2) K using a SuperNova diffractometer (equipped with Atlas detector) with Mo *K*α radiation (λ = 0.71073 Å) under the program CrysAlisPro (Version CrysAlisPro 1.171.39.29c, Rigaku OD, 2017). The same program was used to refine the cell dimensions and for data reduction. The structure was solved with the program SHELXS-2018/3 (Sheldrick, 2018) and was refined on F^2 with SHELXL-2018/3 (Sheldrick, 2018). Numerical absorption correction based on gaussian integration over a multifaceted crystal model was applied using CrysAlisPro. The temperature of the data collection was controlled using the system Cryojet (manufactured by Oxford Instruments). The H atoms were placed at calculated positions (unless otherwise specified) using the instruction AFIX 43 with isotropic displacement parameters having values 1.2 U_{eq} of the attached C atoms. The H atom attached to N1 was found from difference Fourier map, and its coordinates were refined freely. The structure is mostly ordered.

The −CF$_3$ group is disordered over two orientations, and the occupancy factor of the major component of the disorder refines to 0.70(2).

Specified hydrogen bonds (with esds except fixed and riding H)

 D-H   H...A   D...A   <(DHA)

 0.856(19)   2.186(19)   2.9050(17)   141.5(16)   N1-H1N...O1_$2

 0.856(19)   2.117(18)   2.6556(16)   120.4(15)   N1-H1N...F4
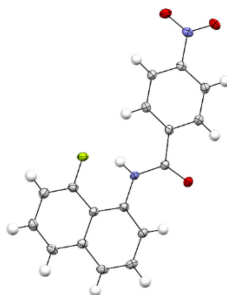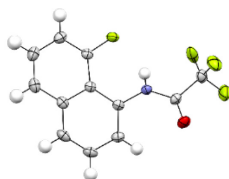

Figure 9.11. Displacement ellipsoid plot (50% probability level) of Compound 11 (Chapter 6)

Sample Preparation

Compound **11** was dissolved in 3 mL dichloromethane in a 3-dram vial and the solvent was evaporated slowly with the vial in slanted position. Crystals of compound **11** were formed when all the solvent had

evaporated.

Experimental details

	xs2322a
Crystal data	
Chemical formula	$C_{12}H_7F_4NO$
M_r	257.19
Crystal system, space group	Monoclinic, $P2_1/c$
Temperature (K)	110
a, b, c (Å)	4.8492 (2), 12.3436 (5), 17.6866 (8)
β (°)	92.080 (4)
V (Å³)	1057.96 (8)
Z	4
Radiation type	Mo $K\alpha$
μ (mm^{-1})	0.15
Crystal size (mm)	0.25 × 0.20 × 0.05
Data collection	
Diffractometer	SuperNova, Dual, Cu at zero, Atlas
Absorption correction	Gaussian
	CrysAlis PRO 1.171.39.29c (Rigaku Oxford Diffraction, 2017) Numerical

	absorption correction based on gaussian integration over a multifaceted crystal model Empirical absorption correction using spherical harmonics, implemented in SCALE3 ABSPACK scaling algorithm.
T_{min}, T_{max}	0.675, 1.000
No. of measured, independent and observed [$I > 2\sigma(I)$] reflections	9969, 2435, 1974
R_{int}	0.028
$(\sin \theta/\lambda)_{max}$ (Å^{-1})	0.650
Refinement	
$R[F^2 > 2\sigma(F^2)]$, $wR(F^2)$, S	0.039, 0.097, 1.10
No. of reflections	2435
No. of parameters	194
No. of restraints	114
H-atom treatment	H atoms treated by a mixture of independent and constrained refinement
$\Delta\rho_{max}$, $\Delta\rho_{min}$ (e Å^{-3})	0.24, -0.25

Computer programs: *CrysAlis PRO* 1.171.39.29c (Rigaku OD, 2017), *SHELXS2018*/3 (Sheldrick, 2018), *SHELXL2018*/3 (Sheldrick, 2018), *SHELXTL* v6.10 (Sheldrick, 2008).

General protocol for synthesis of the N-(8-fluoronaphthalen-1-yl)benzamide derivatives: To a solution of **10** in 10 mL CH$_2$Cl$_2$, 1 equiv. of the appropriate benzoyl chloride derivative was added at room temperature.

To the mixture, 0.1 mL Et$_3$N was added and the solution was stirred at room temperature for 2 h. The solvent was evaporated under reduced pressure and the desired product was purified with MPLC using hexanes and ethyl acetate as eluents.

N-(8-fluoronaphthalen-1-yl)-4-methoxybenzamide (compound 1). Compound **1** was synthesized following the general protocol for benzamide derivative synthesis and isolated as colorless crystalline solid (135 mg, 75% isolated yield). ^{1}H NMR (CDCl$_3$) δ 9.6 (d, J = 20.6 Hz, 1H), 8.76 (d, J = 7.7 Hz, 1H), 7.94 (d, J = 8.7 Hz, 1H), 7.5–7.66 (m, 3H), 7.3–7.4 (m, 1H), 7.1–7.2 (m, 1H), 7.01 (d, J = 8.7Hz, 1H), 3.88 (s, 3H); ^{13}C NMR {^{1}H} (CDCl$_3$) δ 165, 164.97, 165.5, 160.3, 157.9, 136.6, 136.5, 132.93, 132.89, 128.8, 127.4, 127.30, 127.29, 125.56, 125.46, 125.41, 125.38, 123.70, 123.67, 118.32, 118.30, 115.05, 114.97, 114.1, 111.3, 111.1, 55.5; ^{19}F NMR (CDCl$_3$) δ −117 (m, 1F); ^{19}F NMR {^{1}H} (CDCl$_3$) δ −117 (s, 1F); IR 3482, 1675, 1606, 1537, 1495, 1432, 1341 (cm^{-1}, CaF$_2$, CH$_2$Cl$_2$); FTMS (ESI) m/z: [M + H]+ Calcd for C$_{18}$H$_{15}$FNO$_2$+ 296.1081; Found 296.1076.

N-(8-fluoronaphthalen-1-yl)benzamide (compound 2). Compound **2** was synthesized following the general protocol for benzamide derivative synthesis and isolated as a light pink solid (145 mg, 80% isolated yield). ^{1}H NMR (CDCl$_3$) δ 9.69 (d, J = 20.8 Hz, 1H), 8.73 (d, J = 7.86 Hz, 1H), 8.38 (m, 2H), 8.13 (m, 2H), 7.7 (m, 2H), 7.5–7.6 (t, J = 8 Hz, 1H), 7.4–7.47 (m, 1H), 7.19–7.25 (m, 1H); ^{13}C NMR {^{1}H} (CDCl$_3$) δ 163.3, 160.1, 157.7, 149.8, 140.7, 136.51, 136.48, 131.95, 131.91, 128.1, 127.23, 127.21, 125.93, 125.82, 125.62, 125.59, 124.81, 124.79, 124.2, 118.91, 118.89, 150.07, 149.99, 111.7, 111.5; ^{19}F NMR (CDCl$_3$) δ −116.96 (m, 1F); ^{19}F NMR {^{1}H} (CDCl$_3$) δ −116.96 (s, 1F); IR 3477, 1681, 1541, 1487, 1432, 1342 (cm^{-1}, CaF$_2$, CH$_2$Cl$_2$); FTMS (ESI) m/z: [M + H]+ Calcd for C$_{17}$H$_{13}$FNO+ 266.0976; Found 266.0970.

N-(8-fluoronaphthalen-1-yl)-4-nitrobenzamide (compound 3). Compound **3** was synthesized following the general protocol for benzamide derivative synthesis and isolated as a yellow solid (162 mg, 85% isolated yield). ^{1}H NMR (CDCl$_3$) δ 9.7 (d, J = 21 Hz, 1H), 8.79 (m, 1H), 7.98 (m, 1H), 7.5–7.68 (m, 6H), 7.34–7.42 (m, 1H), 7.15–7.23 (m, 1H); ^{13}C NMR {^{1}H} (CDCl$_3$) δ 165.45, 165.43, 160.3, 157.8, 136.55, 136.51, 135.2, 132.72, 132.68, 131.9, 128.9, 127.30, 127.29, 126.9, 125.6, 125.5, 125.44, 125.40, 123.98, 123.95, 118.49, 118.47, 115.1, 115, 111.4, 112.2; ^{19}F NMR (CDCl$_3$) δ −117 (m, 1F); ^{19}F NMR {^{1}H} (CDCl$_3$) δ −117 (s, 1F); IR 3470, 1688,

1606, 1540, 1531, 1503, 1487, 1347 (cm^{-1}, CaF$_2$, CH$_2$Cl$_2$); FTMS (ESI) m/z: [M + H]+ Calcd for C$_{17}$H$_{12}$FN$_2$O$_3$+ 311.0826; Found 311.0819.

Synthesis of 4-(dimethylamino)-*N*-(8-fluoronaphthalen-1-yl)benzamide (compound 4): Compound **3** (100 mg, 0.32 mmol) was dissolved in 30 mL EtOH:THF (2:1) and Pd/C was added to the solution. The mixture was purged with H$_2$ gas until TLC indicated complete consumption of **3** and the mixture was purged with excess H$_2$ gas for another 30 min. Pd/C was then filtered through celite and the cake was washed with 15 mL THF. The solvent was evaporated under reduced pressure and the ^{1}H NMR of mixture indicated complete conversion of NO$_2$ to NH$_2$. The intermediate p-NH$_2$ derivative was utilized without further purification. It was dissolved in 20 mL EtOH, 200 mg (1.45 mmol) of K$_2$CO$_3$ and 0.1 mL (1.6 mmol) MeI were added to the mixture and the solution was refluxed overnight. The reaction mixture was filtered over Celite, washed with 10 mL EtOH and filtrate was evaporated under reduced pressure. The dimethylated product was isolated by MPLC using hexanes and ethyl acetate as eluent as a light pink solid (35 mg, 35% isolated yield). ^{1}H NMR (CDCl$_3$) δ 9.63 (d, J = 21.1 Hz, 1H), 8.82 (m, 1H), 7.88 (m, 2H), 7.5–7.67 (m, 3H), 7.3–7.41 (m, 1H), 7.12–7.22 (m, 1H), 6.76 (m, 2H), 3.06 (s, 6H); ^{13}C NMR {^{1}H} (CDCl$_3$) δ 165.49, 165.47, 160.5, 158.1, 152.7, 136.62, 136.58, 128.5, 127.42, 127.40, 125.42, 125.38, 125.35, 125.32, 123.17, 123.14, 121.8, 117.97, 117.95, 114.98, 114.90, 111.3, 111.2, 110.9, 40.1; ^{19}F NMR (CDCl$_3$) δ −116.29 (m, 1F); ^{19}F NMR {^{1}H} (CDCl$_3$) δ −116.29 (s, 1F); IR 3486, 1669, 1607, 1541, 1526, 1501 (cm^{-1}, CaF$_2$, CH$_2$Cl$_2$); FTMS (ESI) m/z: [M + H]+ Calcd for C$_{19}$H$_{18}$FN$_2$O+ 309.1398; Found 309.1392.

Synthesis of 2,2,2-trifluoro-*N*-(8-fluoronaphthalen-1-yl)acetamide (compound 11): To a solution of **10** (110 mg, 0.68 mmol) in 10 mL DCM was added 0.1 mL (0.7 mmol) of trifluoroacetic anhydride and 0.1 mL Et$_3$N. After stirring at room temperature for 2 h, the solvent was evaporated under reduced pressure and the product was purified on MPLC using hexanes and ethyl acetate as eluents as a white solid (150 mg, 86% isolated yield). ^{1}H NMR (CDCl$_3$) δ 9.7 (d, J = 19.9 Hz, 1H), 8.52 (m, 1H), 7.6–7.8 (m, 2H), 7.5–7.59 (m, 1H), 7.4–7.49 (m, 1H), 7.15–7.3 (m, 1H); ^{13}C NMR {^{1}H} (CDCl$_3$) δ 159.7, 157.3, 155, 154.6, 136.31, 136.28, 129.74, 129.70, 126.96, 126.94, 126.3, 126.2, 125.97, 125.94, 125.50, 125.46, 120.1, 119.36, 119.34, 117.3, 115.0, 114.9, 114.4, 112.1, 111.9; ^{19}F NMR (CDCl$_3$) δ −117.9 (m, 1F), −76.19 (s, 3F); IR 3443, 1737, 1638, 1555,

1507, 1443, 1382 (cm^{-1}, CaF$_2$, CH$_2$Cl$_2$); FTMS (ESI) m/z: [M + H]+ Calcd for C$_{12}$H$_8$F$_4$NO+ 258.0536; Found

258.0530.

9.6 Experimental Section for Chapter 7

Single Crystal X-Ray Crystallography

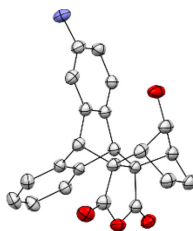**Crystal Structure of Compound 3**

Figure 9.12. Displacement ellipsoid plot (50% probability level) of Compound 5 (Chapter 7)

All reflection intensities were measured at 110(2) K using a SuperNova diffractometer (equipped with Atlas

detector) with Cu *K*α radiation (λ = 1.54178 Å) under the program CrysAlisPro (Version CrysAlisPro

1.171.39.29c, Rigaku OD, 2017). The same program was used to refine the cell dimensions and for data

reduction. The structure was solved with the program SHELXS-2018/3 (Sheldrick, 2018) and was refined on

F^2 with SHELXL-2018/3 (Sheldrick, 2018). Analytical numeric absorption correction using a multifaceted

crystal model was applied using CrysAlisPro. The temperature of the data collection was controlled using

the system Cryojet (manufactured by Oxford Instruments). The H atoms were placed at calculated positions

using the instruction AFIX 13, AFIX 23, AFIX 43, AFIX 93 or AFIX 147 with isotropic displacement parameters

having values 1.2 or 1.5 U_{eq} of the attached C, N or O atoms. The structure is partly disordered. The

asymmetric unit contains two crystallographically independent molecules, and for each molecule, the −NH$_2$

group is disordered over the positions C19X/C20X (X = A, B). For molecule A, the −NH$_2$ group is located

mostly on C20A, and the occupancy factor of the major component of the disorder refines to 0.927(4). For

molecule B, the −NH$_2$ group is located more often on C19B, and the occupancy factor of the major

component of the disorder refines to 0.605(5).

Specified hydrogen bonds (with esds except fixed and riding H)

D-H	H...A	D...A	<(DHA)	
0.88	2.25	3.036(3)	149.5	N1A^a-H1A1^a...O1B_$2
0.88	2.34	3.119(3)	147.5	N1A^a-H1A2^a...O4A_$2
0.88	1.65	2.52(3)	167.0	N1C^b-H1C1^b...O1B_$2
0.88	2.25	3.095(4)	159.6	N1B^a-H1B2^a...O2A_$3
0.88	2.03	2.828(4)	150.0	N1B^a-H1B1^a...O4B_$5
0.88	1.97	2.821(5)	163.9	N1D^b-H1D4^b...O4B_$5

Sample Preparation

Compound **5** was dissolved in 3 mL dichloromethane in a 3-dram vial and the solvent was evaporated slowly with the vial in slanted position. Crystals of compound **5** were formed when all the solvent had evaporated.

Experimental details

	xs2325a
Crystal data	
Chemical formula	$C_{23}H_{19}NO_4$
M_r	373.39
Crystal system, space group	Monoclinic, $P2_1/c$
Temperature (K)	110
a, b, c (Å)	15.9450 (3), 8.13292 (13), 27.6436 (5)
β (°)	95.2369 (19)
V (Å^3)	3569.84 (11)
Z	8
Radiation type	Cu $K\alpha$

μ (mm^{-1})	0.78
Crystal size (mm)	0.30 × 0.18 × 0.06
Data collection	
Diffractometer	SuperNova, Dual, Cu at zero, Atlas
Absorption correction	Analytical *CrysAlis PRO* 1.171.40.53 (Rigaku Oxford Diffraction, 2019) Analytical numeric absorption correction using a multifaceted crystal model based on expressions derived by R.C. Clark & J.S. Reid. (Clark, R. C. & Reid, J. S. (1995). Acta Cryst. A51, 887-897) Empirical absorption correction using spherical harmonics, implemented in SCALE3 ABSPACK scaling algorithm.
T_{min}, T_{max}	0.859, 0.965
No. of measured, independent and observed $[I > 2\sigma(I)]$ reflections	21669, 6977, 5430
R_{int}	0.037
$(\sin\theta/\lambda)_{max}$ (Å^{-1})	0.616
Refinement	
$R[F^2 > 2\sigma(F^2)]$, $wR(F^2)$, S	0.053, 0.142, 1.05
No. of reflections	6977

No. of parameters	521
No. of restraints	1
H-atom treatment	H-atom parameters constrained
$\Delta\rho_{max}$, $\Delta\rho_{min}$ (e Å^{-3})	0.47, -0.38

Computer programs: *CrysAlis PRO* 1.171.39.29c (Rigaku OD, 2017), *SHELXS2018*/3 (Sheldrick, 2018), *SHELXL2018*/3 (Sheldrick, 2018), *SHELXTL* v6.10 (Sheldrick, 2008).

Synthesis of Compound 4: Compound **1** (180 mg, 0.5 mmol)[21] was dissolved in 7 mL CH_3CN and 80 mg of NH_4NO_3 (1 mmol) in a 3:2 mixture of CH_3CN:TFAA (TFAA = trifluoroacetic anhydride) was added to the solution. The reaction mixture was stirred at room temperature for 1 h after which the solvent was evaporated under reduced pressure. The mixture was subjected to MPLC separation using hexanes/ethyl acetate as eluent. The product was isolated as a white solid (185 mg, 82% isolated yield). ^{1}H NMR (CDCl$_3$) δ 8.16 (d, *J* = 2 Hz, 1H), 8.1 (dd, *J* = 8.1 Hz; 2.1 Hz, 1H), 7.45 (d, *J* = 8.2 Hz, 1H), 7.27–7.32 (m, 2H), 7.18–7.22 (m, 2H), 4.83 (s, 2H), 4.72 (s, 1H), 2.88 (s, 2H), 1.95–2.1 (m, 2H), 1.55–1.65 (m, 2H); ^{13}C NMR {^{1}H} (CDCl$_3$) δ 171.6, 171.5, 147.6, 147.1, 141.8, 139.8, 139.2, 128.34, 128.32, 125.8, 125.6, 123.9, 120.1, 89.7, 67.6, 67.5, 48.7, 48.6, 43.72, 43.67, 24.98, 24.89; IR 1782, 1649, 1530, 1349 (cm^{-1}, CaF$_2$, CH$_2$Cl$_2$).

Synthesis of Compound 5: To a solution of **4** (150 mg, 0.34 mmol) in 20 mL of EtOH, was added 30 mg of Pd/C. The mixture was subjected to hydrogenation in a Parr reactor (3 atm) until ^{1}H NMR showed complete conversion of **4**. The reaction mixture was filtered through a plug of Celite and the cake was washed with an additional 15 mL of EtOH. The solvent was evaporated under reduced pressure and the desired product (white solid) was purified by silica gel chromatography using 50% EtOAc in hexanes as the eluent (54 mg, 43% isolated yield). ^{1}H NMR (CDCl$_3$) δ 7.19–7.25 (m, 3H), 7.1–7.15 (m, 2H), 6.8 (d, *J* = 2.3 Hz, 1H), 6.5 (dd, *J* = 8 Hz; 2.3 Hz, 1H), 4.64 (d, *J* = 11 Hz, 2H), 3.87 (d, *J* = 11.4 Hz, 1H), 3.7–3.85 (br, 2H), 2.53 (m, 2H), 1.82 (m, 2H), 1.36 (m, 2H), 0.37 (d, *J* = 11.7 Hz, 1H); ^{13}C NMR {^{1}H} (CDCl$_3$) δ 173.23, 173.17, 146.5, 142.3, 141.3, 140.3, 129.5, 127.7, 127.5, 126.9, 125.4, 125.1, 113.3, 113.2, 85.4, 69.0, 68.6, 48.9, 47.8, 46.19, 46.16, 25.33, 25.29; IR 3533, 3394, 2963, 2928, 2908, 1778, 1672 (cm^{-1}, CaF$_2$, CH$_2$Cl$_2$).

Vita

Kazim was born and raised in Quetta, the capital city of Pakistan's largest yet least populated province, Balochistan. He attended St. Mary's High School Quetta till 7th grade before moving to Balochistan Residential College (BRC) Loralai where he spent 4.5 years in a boarding school. After completing his matriculation (10th grade) from BRC in 2010, he moved back to his hometown and attended Tameer-i-Nau Public College for his intermediate (12th grade). He was then admitted into the Syed Babar Ali School of Science and Engineering at Lahore University of Management Sciences (LUMS), one of the most prestigious universities in Pakistan, through their financial aid program. He graduated from LUMS with BS Chemistry in 2016 with high distinction. During his time at LUMS, he conducted undergraduate research with Prof. Rahman S. Z. Saleem on the synthesis of heterocyclic compounds with the aim of targeting MDM2-p53 interaction in cancer cells. He was then admitted into the graduate program at the Department of Chemistry, Johns Hopkins University in Baltimore, USA. After waiting more than 7 months for his student visa, during which he worked as a research assistant at LUMS, he started his graduate studies in Spring 2017 and joined the Lectka laboratory later that semester. During his time in the Lectka laboratory, he designed and synthesized several caged molecules to investigate the physical and chemical ramifications of non-covalent interactions in synthetic organic chemistry. After graduating in May 2022, he plans to conduct postdoctoral research at the National Cancer Institute (NCI) of the National Institute of Health (NIH) in Dr. Euna Yoo's laboratory. During his postdoctoral time, he hopes to apply his synthetic skills to translational research at the interface of organic chemistry and biology and expand his knowledge and skills in the field of chemical biology.